UNIVERSITY of CALIFORNIA
Santa Barbara

Theoretical Study of Material and Device Properties of Group-III Nitrides

A dissertation submitted in partial satisfaction of the requirements for the degree of

Doctor of Philosophy

in

Materials

by

Qimin Yan

Committee in charge:

Professor Chris G. Van de Walle, Chair

Professor Matthias Scheffler

Professor James S. Speck

Professor Steven P. Denbaars

June 2012

The dissertation of Qimin Yan is approved:

Professor Matthias Scheffler

Professor James S. Speck

Professor Steven P. Denbaars

Professor Chris G. Van de Walle, Committee Chair

June 2012

Theoretical Study of Material and Device Properties

of Group-III Nitrides

Copyright © 2012

by

Qimin Yan

Acknowledgments

First of all, I would like to thank my advisors, Matthias Scheffler and Chris Van de Walle, for giving me the opportunity to study interesting problems, patient instructions, tremendous support, and continuous encouragement. They have different styles in doing science, and they both taught me so much in their own way. Chris' severe reasoning and never-ending feedbacks have shaped my style in thinking, writing, and speaking. Matthias' unique thinking and acute observation on physics problems made me think more deeply from different aspects. Benefiting from their expertise in different research areas ranging from electronic structure theory to semiconductor physics, I have grown up much quicker than I expected. All in all, during the last five years, Matthias and Chris have greatly affected my attitude toward both science and life, and they have completely reshaped me.

I am indebted to Patrick Rinke, for collaboration on the subjects on strain effects in nitrides and the great help he offered at the early stage of my graduate study. Also I am so grateful to the collaboration with Anderson Janotti. His insight and knowledge on the subjects of defects in nitride materials have greatly helped me. As a senior project scientist, he has devoted great efforts to the group and all of us benefit a lot from these efforts. I also would like to thank Manos Kioupakis for his extremely patient help through various projects including *GW* and *BSE* calculations. His patient instructions and also his guidance as a friend contributed a great deal to building my confidence. All these discussions

and collaborations have greatly enhanced my scientific career in different research areas.

I am also grateful to collaborations with experimentalists in SSLEC including Yuji Zhao, Chia-Yen Huang, and Chih-Chien (Eddie) Pan, visiting professor Yuhrenn Wu, and Prof. James Speck on the topic of device simulations. The many interesting discussions enabled me to establish a connection between material properties and realistic device performance, the results of the collaborations constitute most of the material in Chapter 4.

I have also greatly benefited from the interactions with other members of Chris' group. During the past five years the group has grown quickly, with many outstanding postdoctoral researchers and graduate students. The invaluable discussions and collaborations with Maosheng Miao, Poul Moses, Audrius Alkauskus, Khang Hoang, Daniel Steiauf, Hartwin Peelaers, Justin Weber, Joel Varley, Gareth Wilson-Short, John Lyons, Cyrus Dreyer, Luke Gordon, Lars Bjaalie, Patrick McBride, Christopher Roberts, and other members in the group are gratefully acknowledged. I am also grateful to fruitful discussions with Atsushi A. Yamaguchi, Prof. Horia Metiu, Gregory Mills, Dan Cohen, Alex Romanov, Anurag Tyagi, Hisashi Masui, and Matthias Bickermann.

Finally, I wish to thank my dear wife, Jie, for her love, continuous support, and encouragement throughout my graduate career.

Curriculum Vitae

Qimin Yan

Education

2012	Ph.D. in Materials, University of California, Santa Barbara
2006	M.S. in Physics, Tsinghua University, China
2003	B.S. in Applied Physics, Xi'an Jiaotong University, China

Awards

2011	Outstanding Graduate Student Research Achievement Award by the Solid State Lighting and Energy Center at UCSB
2006	Excellent Master Degree Thesis Prize of Tsinghua University
2005	"GuangHua" Scholarship

Publications

"Origins of optical absorption and emission lines in AlN", Qimin Yan, Anderson Janotti, Matthias Scheffler, and Chris G. Van de Walle, in preparation.

"Strain effects and band parameters in MgO, ZnO and CdO", Qimin Yan, Patrick Rinke, Matthias Scheffler, and Chris G. Van de Walle, submitted.

"Polarization-driven topological insulator transition in a GaN/InN/GaN quantum well", Mao-Sheng Miao, Qimin Yan , Chris G. Van de Walle, W. K. Lou, L. L. Li, and Kai Chang, submitted.

"Interplay of polarization fields and Auger recombination in the efficiency droop of nitride light-emitting diodes", Emmanouil Kioupakis, Qimin Yan, and Chris G. Van de Walle, submitted.

"Influence of Polarity on Carrier Transport in Semipolar Multiple-Quantum-Well (20-21) and (20-2-1) Light-Emitting Diodes", Yoshinobu Kawaguchi, Chia-Yen Huang, Yuh-Renn Wu, Qimin Yan, Chih-Chien Pan, Yuji Zhao, Shinichi Tanaka, Kenji Fujito, Daniel Feezell, Chris G. Van de Walle, Steven P. DenBaars, and Shuji Nakamura, Appl. Phys. Lett. 100, 231110 (2012).

"Indium incorporation and emission properties of nonpolar and semipolar InGaN quantum wells", Yuji Zhao, Qimin Yan, Chia-Yen Huang, Shih-Chieh Huang, Po Shan Hsu, Shinichi Tanaka, Chih-Chien Pan, Yoshinobu Kawaguchi, Kenji Fujito, Chris G. Van de Walle, James S. Speck, Steven P. DenBaars, Shuji Nakamura, and Daniel Feezell, Appl. Phys. Lett. 100, 201108 (2012).

"Confinement effects on valence-subband character and polarization anisotropy in (11-22) semipolar InGaN/GaN quantum wells", Christopher Roberts, Qimin Yan, Mao-Sheng Miao, and Chris G. Van de Walle, J. Appl. Phys. 111, 073113 (2012).

"Role of nitrogen vacancies in the luminescence of Mg-doped GaN", Qimin Yan, Anderson Janotti, Matthias Scheffler, and Chris G. Van de Walle, Appl. Phys. Lett. 100, 142110 (2012).

"Influence of Mg-doped barriers on semipolar (20-21) multiple-quantum-well green light-emitting diodes", Chia-Yen Huang, Qimin Yan, Yuji Zhao, Kenji Fujito, Daniel Feezell, Chris G. Van de Walle, James S. Speck, Steven P. DenBaars, and Shuji Nakamura, Appl. Phys. Lett. 99, 141114 (2011)

"High optical polarization ratio from semipolar (20-2-1) blue-green InGaN/GaN light-emitting diodes", Yuji Zhao, Shinichi Tanaka, Qimin Yan, Chia-Yen Huang, Roy B. Chung, Chih-Chien Pan, Kenji Fujito, Daniel Feezell, Chris G. Van de Walle, James S. Speck, Steven P. DenBaars, and Shuji Nakamura, Appl. Phys. Lett. 99, 051109 (2011).

'"Hybrid functional investigations of band gaps and band alignments for AlN, GaN, InN, and InGaN", Poul Georg Moses, Maosheng Miao, Qimin Yan, and Chris G. Van de Walle, J. Chem. Phys. 134, 084703 (2011).

"Band parameters and strain effects in ZnO and group-III nitrides", Qimin Yan, Patrick Rinke, M Winkelnkemper, A Qteish, D Bimberg, Matthias Scheffler, and Chris G Van de Walle, Semi. Sci. Tech. 26, 014037 (2011).

"Role of strain in polarization switching in semipolar InGaN/GaN quantum wells", Qimin Yan, Patrick Rinke, Matthias Scheffler, and Chris G. Van de Walle, Appl. Phys. Lett. 97, 181102 (2010)

"Strain effects in group-III nitrides: Deformation potentials for AlN, GaN, and InN", Qimin Yan, Patrick Rinke, Matthias Scheffler, and Chris G. Van de Walle. Appl. Phys. Lett. 95, 121111 (2009).

Contributed Talks

2012 American Physical Society March Meeting, Boston, USA

- Role of native defects and related complexes in absorption and luminescence of AlN.

2011 9th International Conference on Nitride Semiconductors, Glasgow, Scotland

- Role of nitrogen vacancies and related complexes in luminescence of Mg-doped GaN.

2011 Materials Research Society Spring Meeting, San Francisco, CA, USA

- Role of nitrogen vacancies and related complexes in compensation and luminescence of Mg-doped GaN.

2011 American Physical Society March Meeting, Dallas, TX, USA

- Role of nitrogen vacancies and related complexes in compensation and luminescence of Mg-doped GaN.

2010 American Physical Society March Meeting, Portland, OR, USA

• First-Principles determination of deformation potentials and band parameters in group-II oxide semiconductors.

2009 American Physical Society March Meeting, Pittsburgh, PA, USA

• First-Principles determination of deformation potentials in nitride semiconductors.

Abstract

Theoretical Study of Material and Device Properties

of Group-III Nitrides

by

Qimin Yan

Group-III nitride semiconductors, including AlN, GaN, InN, and their alloys, are ideal materials for solid state lighting applications. Current research focuses on improving the efficiency by improvements in materials quality and novel device designs, for instance based on nonpolar and semipolar growth. The motivation for our work is to assist and guide the experimental development of high-performance solid state optoelectronic devices by performing computational studies. Our investigations range from basic structural and electronic properties of nitrides to the effects of device design on efficiency of light emission.

In the area of fundamental properties, we performed a systematic study of strain effects on the electronic band structures of the group-III-nitrides (AlN, GaN and InN) using density-functional theory with an advanced hybrid functional as well as using the quasiparticle GW method. We present a complete set of deformation potentials that allows us to predict the band positions of group-III nitrides and their alloys (InGaN and AlGaN) under realistic strain conditions. We

then employed the resulting first-principles deformation potentials to predict the effects of strain on transition energies and valence-band structures of c-plane, non-polar, and semipolar InGaN alloy layers grown on GaN substrates, with particular attention to the role of strain in the polarized light emission.

We also investigated the role of native defects in the optical properties of GaN and AlN, again using hybrid density-functional calculations. We established that complexes between Mg and nitrogen vacancies lead to the broad red luminescence that has often been observed in GaN. We find that isolated nitrogen vacancies can give rise to broad emission peaked at 2.18 eV. We show that isolated aluminum vacancies lead to an absorption peak at 3.43 eV and an emission peak at 2.73 eV. We also find that V_{Al}-$\mathrm{O_N}$ complexes can give rise to absorption peaked at 3.97 eV and emission peaked at 3.24 eV. These results indicate that Al vacancies and their complexes with oxygen lead to distinct UV absorption lines that have hampered development of UV-transparent AlN substrates. We also investigate the optical excitation of the bulk AlN and the nitrogen vacancies in AlN using *ab initio* many-body perturbation theory. Our calculations show that many-body effect strongly affects the absorption spectrum of AlN and a localized exciton is formed around the vacancy.

Finally, we have carried out device simulations based on k.p theory and Schrödinger-Poisson solvers to investigate the role of strain, polarization and doping in performance of nitride-based LED devices. We elucidate the mechanisms by which

modification of GaN barriers by Mg doping benefits hole transport, and we demonstrate how the strain-induced polarization field affects wavefunction overlap in the quantum wells of the *c*-plane and nonpolar plane LEDs and is related to the droop problem. We show that the emission wavelength shift under current injection is also related with quantum well potential profile and the polarization field inside quantum wells. These simulations shed light on the improvement of nitride-based LED efficiency by device design.

Contents

1 Introduction **1**
1.1 Lighting, past, present and future 1
1.1.1 History 1
1.1.2 Solid state lighting 3
1.2 Group-III nitrides, material and device properties 6
1.2.1 Droop problem 6
1.2.2 Spontaneous and piezoelectric polarization in nitrides 10
1.3 Defects and impurities in nitride materials and devices 14
1.3.1 Defect formation energy 15
1.3.2 Transition levels, configuration-coordinate diagram, and optical processes 17
1.4 Computational methods 22
1.4.1 Density-functional theory and ground-state properties 23
1.4.2 Screened exchange: hybrid functionals 27
1.4.3 Electronic excitations: *GW* method 28
1.4.4 Electronic excitations: Bethe-Salpeter equation 31
1.4.5 Band structures and $\mathbf{k}\cdot\mathbf{p}$ method 35
1.4.6 Schrödinger-Poisson and drift-diffusion model 40

2 Strain effects in group-III nitrides and alloys **46**
2.1 Introduction 46
2.2 Model and computational details 52
2.3 Computational results 59
2.3.1 Lattice parameters, band gaps, and band structures 59
2.3.2 Transition energies under strain 61
2.3.3 Deformation potentials of group-III nitrides 64
2.4 Strain effects in InGaN alloys 67
2.4.1 Band gap and bowing parameter of *c*-plane InGaN alloys . . 69
2.4.2 Strain effects on the polarization character of nonpolar *m*-plane InGaN 72

2.4.3 The role of strain in the polarization switching of $(11\bar{2}2)$ InGaN alloys . . . 75
2.5 Conclusion . . . 82

3 The role of defects in absorption and luminescence in GaN and AlN 84
3.1 The role of the nitrogen vacancy in luminescence in Mg-doped GaN 85
3.1.1 Nitrogen vacancies and complexes in GaN . . . 85
3.1.2 Computational details . . . 86
3.1.3 Formation of nitrogen vacancies and complexes in GaN . . . 87
3.1.4 Luminescence of nitrogen vacancies and complexes in GaN . 94
3.1.5 Summary . . . 97
3.2 Optical absorption and emission due to native defects and complexes in AlN . . . 97
3.2.1 Motivation . . . 97
3.2.2 Computationals details . . . 100
3.2.3 Formation of native defects and complexes in AlN . . . 101
3.2.4 Optical signatures of native defects and complexes in AlN . . 105
3.2.5 Summary . . . 109
3.3 Excitonic effect on optical absorption from nitrogen vacancies in AlN 109
3.3.1 Motivation and computational details . . . 109
3.3.2 Results for the excitonic effects in optical absorption . . . 111
3.3.3 Summary . . . 118

4 Device simulation of nitride-based LEDs 119
4.1 Droop problem and polarization field . . . 120
4.1.1 Motivation . . . 120
4.1.2 Wavefunction overlap in polar and nonpolar quantum wells . 121
4.1.3 Summary . . . 126
4.2 Carrier transport and the effect of the barrier modification . . . 127
4.2.1 Hole transport in multiple-quantum-well structures . . . 127
4.2.2 Experimental spectra of double-quantum-well LEDs . . . 128
4.2.3 Effects of Mg doping on the hole distribution in DQW LEDs 129
4.2.4 Summary . . . 132
4.3 Optical spectrum of $(20\bar{2}1)$ and $(20\overline{21})$ semipolar LEDs . . . 132
4.3.1 Experimental observations: dependence of emission wavelengths on the inclination angle . . . 132
4.3.2 Simulations: polarization fields and emission wavelengths . . 134
4.3.3 Summary . . . 137

5 Summary and outlook 139

Bibliography 142

Chapter 1

Introduction

1.1 Lighting, past, present and future

1.1.1 History

Lighting was one of the earliest applications of electric power. Today it utilizes approximately 20% of the world's grid-based electricity production. The main reason for this large share is the inefficiency of current light sources, which unfortunately waste most of the power. The worldwide demand for lighting is increasing rapidly, and there is a strong motivation for improving the efficiency of light sources and mitigating their effect on worldwide energy consumption and global climate change.

Traditional electric light bulbs were developed more than 100 years ago. The technology is still in use today and has been noticeably improved, e. g., Halogen

bulbs. The operation of these incandescent light bulbs is quite simple while not efficient: by heating a tungsten wire in a vacuum bulb to a high temperature (3500 K), the wire glows white-hot and emits a broad black-body radiation spectrum that covers the entire visible range. The efficiency of such energy conversion is extremely low, around 5%, which means as much as 95% of the energy consumed by these electric light bulbs is wasted and converted into useless heat. Furthermore, the large amount of heat generated makes the lifespan of such light bulbs short (around 1000 to 2000 hours). Governments around the world are implementing legislation to phase out incandescent light bulbs for general lighting in the near future.

Compared with incandescent light bulbs, fluorescent light bulbs are a more efficient and a longer lasting alternative, in spite of some limitations. The mechanism of such light bulbs is different from incandescent sources: as the electric current passes through a mixture of the inert gas and mercury in a fluorescent tube, the mercury atoms are excited and then emit ultraviolet radiation. The tube's fluorescent coating then converts the ultraviolet light to visible light. Fluorescent light bulbs perform better than traditional electric light bulbs, with efficiencies on the order of 20% and typical lifetimes of 10,000 hours, but they also have their limitations. First of all, although fluorescent light bulbs have much higher efficiencies than incandescent bulbs, the conversion of ultraviolet light to visible light still limits the efficiency of the devices. In addition, fluorescent light bulbs

contain mercury which is a severe health hazard and needs to be safely recycled or disposed.

In the past two decades, solid state lighting based on light-emitting diodes (LEDs) has become the focus. So far, the energy-conversion efficiencies of the best LED devices can exceed 50%, which significantly reduces the energy cost of lighting. Besides the high efficiencies, these LEDs also enjoy an unusually long lifespan. For example, while most incandescent bulbs typically last between 1,000 and 2,000 hours and fluorescent bulbs typically last anywhere between 10,000 and 15,000 hours, LEDs can last 35,000 to 50,000 hours. It makes them an ideal choice for hard-to-reach lighting by eliminating the need to frequently replace the bulb which also reduces maintenance costs. Furthermore, different from fluorescent light bulbs, LEDs do not contain toxic elements. All in all, these semiconductor-based LEDs have the potential to reshape the lighting industry[1].

1.1.2 Solid state lighting

Solid state lighting is enabled by semiconductor light-emitting diodes (LEDs). The history of LEDs can be traced back to the early 1900s. The phenomenon of electroluminescence, which is the underlying physics behind the operation of LEDs, was first discovered by the British scientist H. J. Round, who published a 24-line note reporting light emission from a silicon carbide diode in February, 1907[2]. However, there was no follow-up publication on this topic from Round. A

Russian scientist Oleg Losev independently discovered the phenomena the same year. In the mid 1920s, Losev observed light emission from zinc oxide and silicon carbide crystal rectifier diodes. His first paper on the emission of silicon carbide diodes was published in 1927 by the journal *Wireless Telegraphy and Telephony* in Russia and other important publications followed[3].

However, LED devices were not used in practical applications for decades after their discovery. After almost fifty years, the developments in III-V compound semiconductor research in the 1960s and 1970s led to the successful fabrication of efficient LEDs in the long-wavelength part of the visible spectrum. These LEDs have been applied as indicator lights, e.g., in watches, calculators, and other electronic devices. However, white-light emission for lighting applications, which requires LEDs emitting in the blue or violet part of the spectrum, were still missing. In the 1980s and 1990s, research efforts on solid state lighting focused on ZnSe, but unfortunately defects in this material deteriorated the device performance and limited their lifetimes. The breakthrough happened in the early 1990s when Shuji Nakamura developed the first viable blue LEDs based on the group-III nitrides[4]. Since then, group-III nitrides have become the dominant short-wavelength LED materials.

One of the most important applications of these nitride LED devices is indoor lighting with white-light emission. Several approaches are available to achieve white-light emission with nitride LEDs[1]. The first approach is to use a phosphor.

By combining a blue LED with a yellow phosphor coating, the high-energy blue photons are converted into photons with longer visible wavelengths. This approach has been widely used in most commercial white-light LED devices on the market thanks to its simplicity and low cost. However, this simple method is not perfect: The efficiency of these LEDs is limited by the photon energy conversion process in phosphors, and the color quality achieved with this approach is not always satisfactory. A solution to get better color quality is combining an ultraviolet LED with a mix of phosphors, which produces white light more suitable for indoor use. Unfortunately, the efficiency is then even lower. Another approach is to combine three or more LEDs of different colors, which is the best option for efficiency and color quality but comes at a higher cost.

As the output power of these light-emitting devices becomes higher, LEDs have found applications as display backlights in portable computers, cell phones, and televisions. More powerful LEDs are even commercialized for use in vehicle headlights. In recent years, the total cost of ownership of LED light bulbs is going down and is now comparable with that of fluorescent ones. As a result, their market share for general lighting applications is increasing rapidly. Over the next decade, the value of the LED market is predicted to exceed 15 billion dollars per year.

1.2 Group-III nitrides, material and device properties

Group-III nitride semiconductors, including AlN, GaN, InN, and their alloys, are currently the materials of choice for solid state lighting applications in the short-wavelength range. Their electronic band gaps range from 6.2 eV for AlN to 3.48 eV for GaN and 0.7 eV for InN. Therefore, alloying GaN with InN yields InGaN material with a direct band gap that is tunable over the entire visible light spectrum. The study of nitride materials for light emission is a highly active research area with strong growth prospects. Current research focuses on improving the efficiency by device design and reducing the cost of LEDs in order to deliver affordable devices that can replace the existing solutions for general lighting. Semipolar and nonpolar device growth offer additional control over the device properties and are a promising area for new developments. In the following I describe several key topics of current research on nitride material and device properties.

1.2.1 Droop problem

Although nitride-based LEDs have shown many advantages over conventional light sources and have the potential to reshape the lighting industry, they still exhibit serious shortcomings. It is commonly observed in all nitride-based LEDs

that the internal quantum efficiency (IQE) decreases dramatically when they are operating at the high power that general lighting requires (Fig. 1.1a), which is the so-called efficiency droop problem. Unfortunately, droop becomes worse for devices operating at longer wavelengths, and the lighting efficiency in the green range is quite low, an effect known as the green-gap problem. In order to increase the performance of nitride LED devices at long wavelengths, it is highly desirable to understand the origin of droop and find solutions to mitigate its impact.

Several loss mechanisms have been proposed as the origin of the droop, including electron leakage from the quantum wells[6], defects[7], or Auger recombination[8]. Based on intensive research efforts in recent years[8,9], Auger recombination has been proposed as one of the most plausible mechanisms to cause the droop. Auger recombination is a nonradiative process; namely, the process doesn't generate any photons. During this process, as shown in Fig. 1.1b, an electron and a hole recombine while the energy released by the recombination is transferred to a third carrier via electron-electron scattering. The third carrier involved in the transition can be either an electron or a hole.

Several electron-hole recombination processes, either radiative or nonradiative, are happening during the operation of nitride LEDs and the dependence of recombination rates on carrier density is different. In Auger recombination, three carriers are involved, and the overall recombination rate scales with the third power of the free-carrier density. On the other hand, the radiative recombination

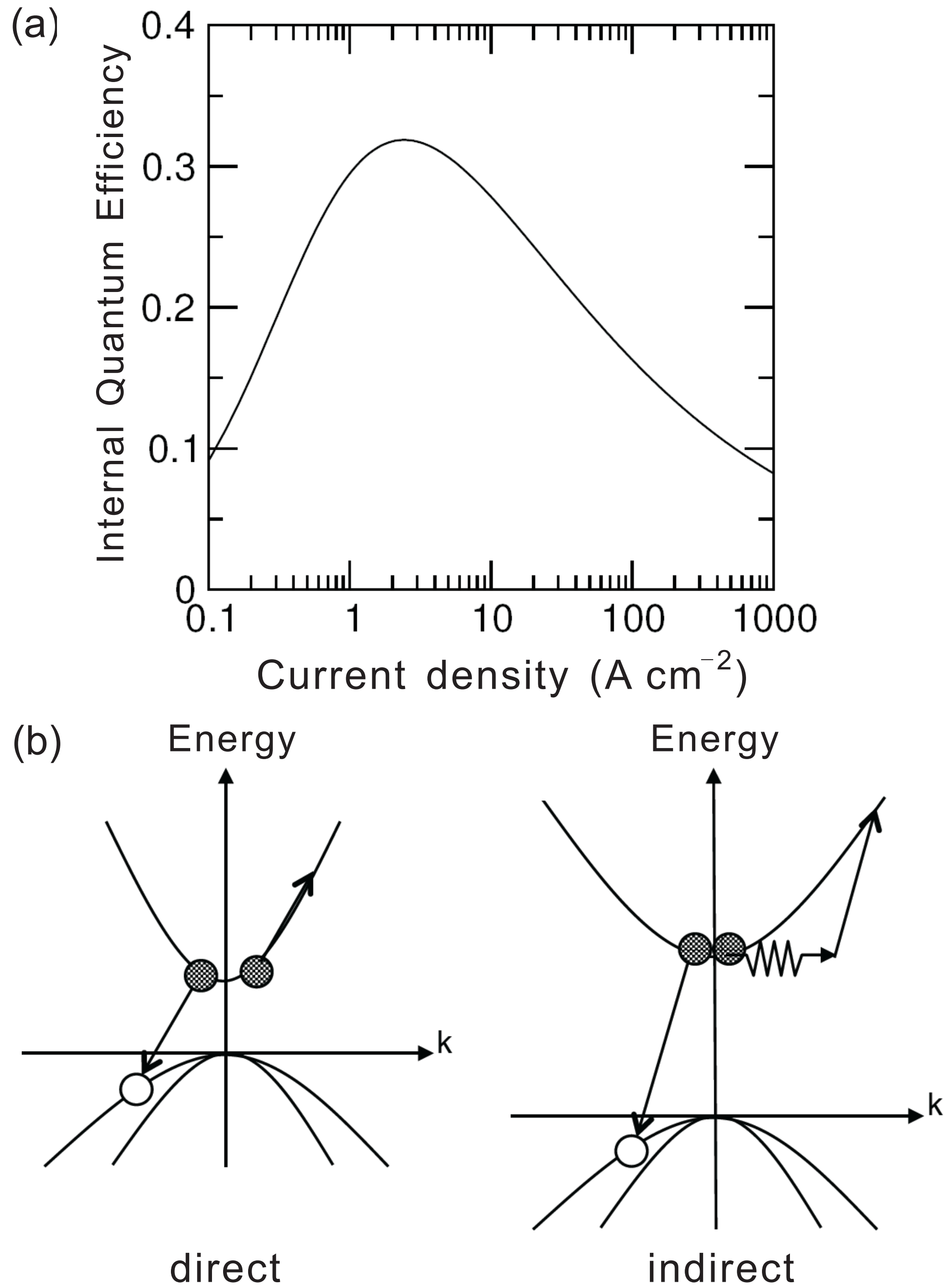

Figure 1.1: (a) Internal quantum efficiency versus injected current density for a nitride-based LED device generated from representative experimental data[5]. A dramatic drop in IQE is observed at high current density. (b) Schematic of direct and indirect Auger recombination processes.

involves electron-hole pairs and its rate increases with the square of the free-carrier density, while Shockley-Read-Hall (SRH) nonradiative recombination at defects depends linearly on the carrier concentration[10]. The internal quantum efficiency, defined as the ratio of emitted photons over total recombined electron-hole pairs, can be described by a so-called ABC model:

$$\eta_{IQE} = \frac{R_{rad}}{R_{SRH} + R_{rad} + R_{Auger}} = \frac{Bn^2}{An + Bn^2 + Cn^3}. \tag{1.1}$$

Due to the existence of the Auger process, which becomes dominant at high injected current densities, the IQE decreases at high injected carrier densities. Experimentally measured values for the Auger coefficient of InGaN are on the order of 10^{-31}-10^{-30} cm^{6}s^{-1}, which is large enough to explain the observed efficiency droop in LEDs[11]. On the theoretical side, earlier investigations for the direct Auger recombination process obtained an Auger coefficient of the order of 10^{-34} cm^{6}s^{-1}[12], which is 3 to 4 orders of magnitude smaller than the experimental results. However, indirect Auger recombination, which requires the assistance of electron-phonon scattering to provide additional momentum to facilitate the recombination, has been found to be the dominant Auger recombination mechanism in nitride materials. Such indirect Auger recombination is strong enough to agree with experimental data and explain the efficiency droop[13].

Currently, lots of research efforts focus on solving the efficiency droop problem of nitride-based LED devices through novel device design. These efforts include improving the carrier distribution over multiple quantum wells via barrier modifi-

cation and increasing the carrier overlap in the quantum well by fabricating devices on semipolar and nonpolar planes. In Sec. 4.2, we show that the modification of GaN barriers by Mg doping benefits hole transport in semipolar LEDs.

1.2.2 Spontaneous and piezoelectric polarization in nitrides

An important physical property of nitride semiconductors with the wurtzite crystal structure is their spontaneous and strain-induced piezoelectric polarization[14,15]. Polarization-induced electric fields are detrimental to the performance of nitride-based optoelectronic devices[16,17]. Hence a good understanding of the polarization effects at nitride material interfaces is essential for device simulations.

All three nitride materials crystallize in the wurtzite structure with four atoms in the primitive unit cell. The space group of this crystal structure is C_{6v}^4 or $P6_3mc$, which is homomorphic to the point group C_{6v} with a screw axis along the c axis. This group contains several rotation operations about the c axis followed by a translation with the vector (0, 0, c/2), while it lacks inversion symmetry. Due to the partially ionic nature of the Ga-N bonds and lack of inversion symmetry, group-III nitrides show spontaneous polarization P_{SP} along the c axis in the equilibrium wurtzite crystal structure. Note that the spontaneous polarization difference at the InGaN/GaN interface is usually small and thus contributes little to the polarization charge at the interface.

Besides spontaneous polarization due to the symmetry of crystals, mechanical

stress also results in a piezoelectric polarization $P_{\rm PZ}$. In nitride semiconductor heterostructures, the lattice mismatch between substrates and active regions induces elastic strain and mechanical stress. When the layer thickness is below a critical thickness for misfit dislocation formation[18], the nitride layers can be pseudomorphically grown on thick substrates, and the lattice mismatch is accommodated by the elastic strain in the layer.

The relation between strain and stress can be described by:[19]

$$\sigma_i = C_{ij}\varepsilon_j, \tag{1.2}$$

where σ_i and ε_i are the six unique stresses and strains and C_{ij} is the 6×6 matrix with the elastic stiffness coefficients with the following notation for the components of the symmetric second-rank stress and strain tensors:

$$\sigma_1 = \sigma_{xx}, \sigma_2 = \sigma_{yy}, \sigma_3 = \sigma_{zz}, \sigma_4 = \sigma_{yz}, \sigma_5 = \sigma_{xz}, \sigma_6 = \sigma_{xy}; \tag{1.3}$$

$$\varepsilon_1 = \varepsilon_{xx}, \varepsilon_2 = \varepsilon_{yy}, \varepsilon_3 = \varepsilon_{zz}, \varepsilon_4 = \varepsilon_{yz}, \varepsilon_5 = \varepsilon_{xz}, \varepsilon_6 = \varepsilon_{xy}. \tag{1.4}$$

By taking into account the symmetry of the space group $P6_3mc$, the piezo-

electric polarization of wurtzite materials is related to strain components as:

$$\mathbf{P}^{pz} = \begin{pmatrix} 0 & 0 & 0 & 0 & e_{15} & 0 \\ 0 & 0 & 0 & e_{15} & 0 & 0 \\ e_{31} & e_{31} & e_{33} & 0 & 0 & 0 \end{pmatrix} \begin{pmatrix} \varepsilon_{xx} \\ \varepsilon_{yy} \\ \varepsilon_{zz} \\ \varepsilon_{yz} \\ \varepsilon_{xz} \\ \varepsilon_{xy} \end{pmatrix} \tag{1.5}$$

with the elements e_{ij} of the piezoelectric tensor in Voigt notation[15,19]. The total polarization is simply the sum of the spontaneous polarization (P_{SP}) and the piezoelectric polarization (P_{PZ}): $P = P_{\mathrm{PZ}} + P_{\mathrm{SP}}$.

Nitride LEDs are traditionally grown along the [0001] crystallographic direction, which is known as the c-axis orientation. The nitride materials are strongly polar along this axis: for Ga-faced polar crystals, the total polarization is directed towards the substrate, while for N-faced crystals it is directed towards the surface. In traditional c-plane nitride-based LED devices, the existence of polarization fields shifts electrons and holes to opposite sides of the well, decreasing the overlap integral, which in turn reduces the recombination efficiency of the system and induces the so called quantum confined Stark effect (QCSE).

Strain-induced polarization effects in nitride layers grown on semipolar and nonpolar templates have been theoretically calculated[20]. Figure 1.2 shows the total polarization as a function of inclination angle away from the c axis calculated

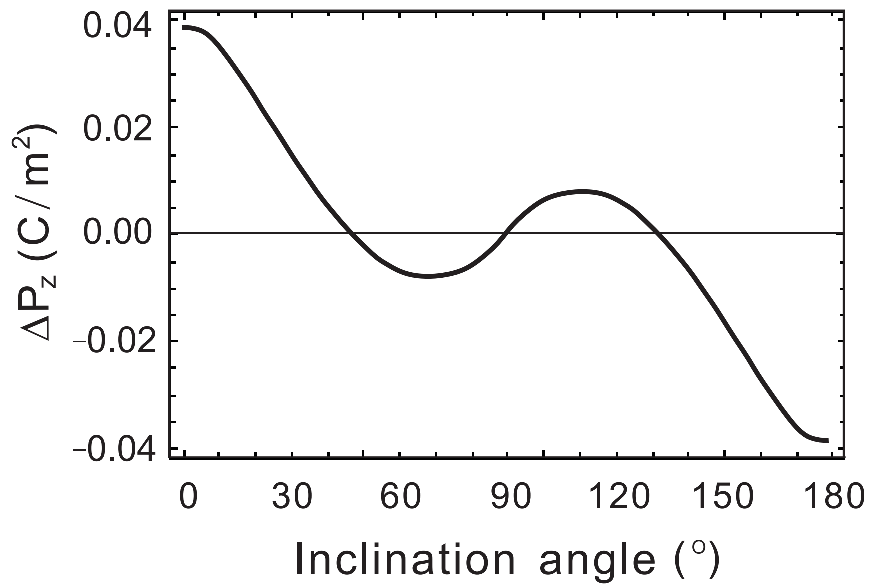

Figure 1.2: Piezoelectric polarization in $In_{0.2}Ga_{0.8}N$ alloys grown on GaN substrates and its dependence on the inclination angle between the growth orientation and the *c* axis. The data are calculated with the approach described by Romanov *et al.* in Ref. 20.

with the approach described by Romanov *et al.* in Ref. 20. It indicates that by growing nitride devices along different crystallographic orientations one can produce quantum-well structures with reduced or even zero internal polarization fields. Recently, high-quality growth of nitride LEDs along nonpolar or semipolar crystallographic directions has been developed and is a subject of active research. In the Sec. 4.1 and 4.3, we will demonstrate how the strain-induced polarization field affects the wavefunction overlap in the quantum wells of the c-plane and nonpolar plane LEDs and is related to the droop problem.

1.3 Defects and impurities in nitride materials and devices

Point defects and impurities are unavoidably formed in nitride crystals during the growth and annealing processes and strongly affect the properties of nitride materials and the performance of nitride-based optoelectronic devices. First, intentional doping of Si and Mg impurities in GaN yields n- and p-type materials respectively, which is the prerequisite for the realization of nitride-based optoelectronic diodes, including LEDs and laser diodes. Second, native defects and/or unintentionally incorporated impurities can induce unintentional free carriers in nitride materials. For example, due to unintentional incorporation of impurities, GaN typically exhibits unintentional n-type doping with carrier concentration on

the order of 10^{16} to 10^{17} cm^{-3}. In addition, these defects introduce several states in the band gaps of nitride materials and can therefore give rise to recombination events during optical absorption or emission. For example, defects in AlN cause strong absorption in the UV region and it is crucial to reduce the concentration of these defects in order to fabricate UV-transparent AlN substrates for UV optoelectronic devices. Finally, defects can behave as charge traps and assist non-radiative recombination in the active region of nitride LEDs. Such recombination lowers the internal quantum efficiency of LEDs in the low current region and can cause serious device degradation in laser devices. These examples highlight the need to study defects in nitride materials and understand their effects on device performance.

1.3.1 Defect formation energy

The concentration of defects in materials is determined by their formation energies. Within the dilute limit, the concentration of a given defect is related to its formation energy (E^f) by the following expression[21]:

$$c = N_0 \, e^{-E^f/k_B T} \quad , \tag{1.6}$$

where k_B is the Boltzmann constant, T is the temperature, and N_0 is the number of sites on which the defect can be incorporated (including the number of possible configurations per site). Normally N_0 is on the order of 10^{22-23} sites·cm^{-3}. In principle, the formation energy in Eq. 1.6 should be the free energy which includes

additional contributions to the formation energy that arise from changes in the volume and the vibrational energy and entropy associated with the defect. It has been shown both experimentally and theoretically that the vibrational entropy of point defects typically ranges between 0 to several k_{B}, which is only important at high temperatures. In our calculation, we use the zero-temperature formation energy and the vibrational entropy term is not included.

As an example, the formation energy of a nitrogen vacancy in charge state q (V_{N}^q) is given by the following expression:

$$E^f[V_{\mathrm{N}}^q] = E_{\mathrm{t}}[V_{\mathrm{N}}^q] - E_{\mathrm{t}}[\mathrm{GaN}] + \mu_{\mathrm{N}} + q\varepsilon_F + \Delta_q. \tag{1.7}$$

The $E_{\mathrm{t}}[V_{\mathrm{N}}^q]$ term is the total energy of the GaN crystal with the V_{N}^q defect, and $E_{\mathrm{t}}[\mathrm{GaN}]$ is the energy of the bulk.

The energy E^f depends on the chemical potentials relevant to the defect. These chemical potentials reflect the conditions of the chemical environment, i.e., the reservoirs with which atoms are exchanged. The N atom removed from the crystal is placed in a reservoir of energy μ_{N}. The chemical potentials are variables for non-elemental materials; in this case, the chemical potentials can vary over a range set by the stability conditions of the solid. For example, the μ_{N} can span a set of values set by the formation enthalpy of GaN, $\Delta H_f(\mathrm{GaN})$, reflecting growth conditions that can vary from N-rich to Ga-rich. In principle, the chemical potentials can be related to partial pressures of the chemical species via standard thermodynamic relationships.

As defects exhibit different charge states, the E^f depends on the energy of the electron reservoir in the material, which is known as the Fermi level (ε_F). The Fermi level in the formation energy expression (Eq. 1.7) is a variable which is referenced to the bulk valence-band maximum (VBM).

In our calculations, we adopt periodic boundary conditions to simulate defects in the crystal. When constructing a supercell it is important to make it large enough so as to reduce spurious defect-defect interactions. For a charged defect system, even if the unit cell is large enough to obtain the correct defect geometry, the long-range coulomb interaction between charge images is still present. The last term in Eq. 1.7, Δ^q, is the correction due to the finite size of the supercell. Due to the applied periodic boundary condition, there exists artificial electrostatic interaction between the image charges and the neutralizing background. This artificial contribution to the total energy needs to be removed when calculating formation energies. For a more detailed discussion of the formalism we refer to the work by Freysoldt[22].

1.3.2 Transition levels, configuration-coordinate diagram, and optical processes

Defects exist in nitride materials in different charge states. The transitions between different charge states of the defect are related to the occupancy of defect levels in the gap. As opposed to the Kohn-Sham defect levels in calculated

band structures, these charge transition levels can be measured experimentally, e.g., by deep-level transient spectroscopy(DLTS). The transition level between charge states q_1 and q_2 is defined as the Fermi-level position for which these two charge states have equal formation energy. We can determine these transition levels from one charge state to another from the calculated formation energies. These transition levels are also called thermodynamic transition levels since they represent the physical situation in which one defect charge state can fully relax to its equilibrium configuration after a charge-state transition.

In the case of shallow centers, these transition levels correspond to the thermal ionization energy of the hydrogenic effective-mass levels. For defects with localized states in the band gap, known as deep centers, these transition levels are those which are experimentally observed in experiments such as DLTS. Therefore, the charge-state transition levels are important to determine the effect of a defect on the electrical behavior of the host material.

Another type of transition between defect levels of different charge states is the optical transition level. This level is defined similarly to the thermodynamic transition level, except the energy of the final state is calculated using the same atomic configuration as the initial state.

The optical level is observed in optical processes such as optical absorption and photoluminescence experiments. Here we choose the optical absorption involving a defect state and the conduction band as an example. During optical absorption,

the electron is excited from the defect state to the conduction band by absorbing a photon. The charge state of the defect is changed upon this electronic transition. The time scale for this electronic transition is much shorter than the time needed for the local geometry of the defect to change. In this way, an electronic transition is most likely to occur without changes in the positions of the nuclei. This approximation is called the Frank-Condon principle. The energy difference from the optical transition level to the conduction-band minimum (CBM) thus correspond to this vertical optical transition energy, assuming that this transition is symmetry allowed.

As mentioned above, the local geometry of a defect depends on its charge state. It is convenient to define a configuration coordinate q to describe the atomic configuration of a defect. For example, q can be defined as the weighted average of the change of atom positions between different defect structures. By plotting the energy as a function of the configuration coordinate, we can construct a configuration-coordinate diagram that describes the dependence of energy of a defect on its atomic configuration. Configuration-coordinate diagrams are very useful tools in studying the optical excitations of defects. The absorption and emission energies calculated from these diagrams can be associated with peaks in experimental absorption and luminescence spectra. Configuration-coordinate diagrams are therefore extremely helpful in identifying specific defects and charge states responsible for the luminescence or absorption bands.

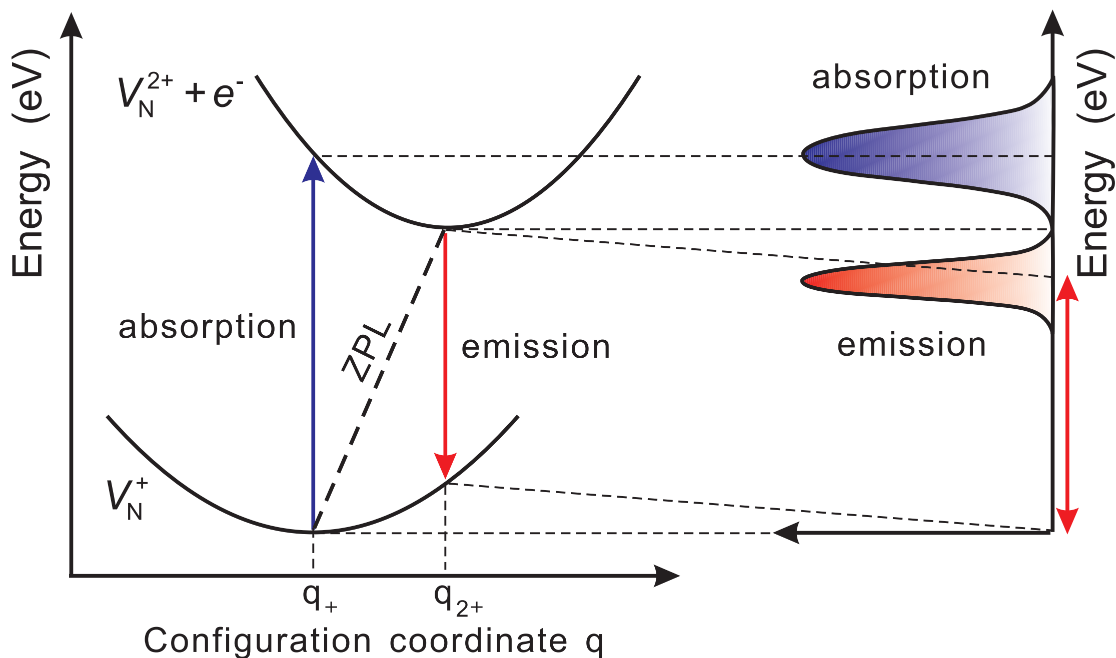

Figure 1.3: Configuration-coordinate diagram describing the process $V_N^+ + \hbar\omega \rightarrow V_N^{2+} + e^-$ in GaN. The upward-pointing solid arrow represents the photoexcitation of an electron from the V_N^+ to the conduction band, while the downward-pointing dotted arrow represents the emission process from the conduction band to the V_N^{2+}. The solid arrows indicate the absorption and emission peaks, while the diagonal dashed arrow represents the zero-phonon line (ZPL).

The excitation of an electron localized in a defect state of the nitrogen vacancy in the positive charge state (V_{N}^{+}) to the conduction band is described by the process $V_{\mathrm{N}}^{+} + \hbar\omega \rightarrow V_{\mathrm{N}}^{2+} + e^{-}$, as depicted in Fig. 1.3. The energy difference between the two equilibrium configurations involved in the transition corresponds to the difference in energy from the $+/2+$ charge-state transition level to the CBM. This energy difference corresponds to the optical transition energy when no phonon is involved and hence is called the zero phonon line (ZPL). The absorption energy of the vertical transition in the configuration-coordinate diagram consists of the energy difference between V_{N}^{+} and V_{N}^{2+} calculated in the atomic configuration of the V_{N}^{+} (configuration coordinate q_{+}) plus an electron at the CBM. This energy corresponds to a peak in the absorption spectrum. On the other hand, the emission energy consists of the energy difference between V_{N}^{2+} plus an electron at the CBM, and V_{N}^{+} calculated in the atomic configuration of V_{O}^{+} (configuration coordinate q_{2+}). The difference in energy of V_{N}^{+} between the configurations at q_{2+} and at q_{+} is the relaxation energy. The relaxation energy can be quite large for localized defects, which leads to broad absorption and emission bands as well as a large energy difference between the absorption and emission peaks, which is called the Stokes shift.

1.4 Computational methods

First-principles computational approaches based on density-functional and many-body perturbation theories are a powerful set of tools that have complemented and guided experimental research efforts on nitride materials for LEDs. With the most advanced first-principles approaches, highly accurate equilibrium crystal structures of materials can be predicted within 1% error compared with experiments. Accurate electronic properties, including band gaps, band structures, and effective masses can also be obtained using these methods. In addition, these first-principles methods can be employed to understand and predict the properties of defects that are crucial for optoelectronic performance.

The limitation of first-principles calculations is that they can only be performed on systems up to a few hundred atoms in size, which is insufficient to model device structures. Fortunately, on the length scale of device structures there is no need for a fully atomistic description and the performance of nitride-based LED devices can be studied by semi-empirical simulations such as the $\mathbf{k} \cdot \mathbf{p}$ model. The use of input parameters obtained from first-principles calculations in the $\mathbf{k} \cdot \mathbf{p}$ scheme combined with a Schrödinger-Poisson solver and drift-diffusion model enables the study of band diagrams, subband structures, strain and polarization effects, and carrier transport in nitride optoelectronic devices.

Numerous computational studies in last two decades have shown the predictive power of computational techniques for the study of technologically important

nitride materials and the performance of nitride-based optoelectronic devices. In the following, we present an overview of the computational methodology.

1.4.1 Density-functional theory and ground-state properties

Density-functional theory (DFT) is the most widely used computational method for electronic structure studies of material properties[23]. The theory says that the total energy of the system is a functional of the electron density and reaches its minimum at the exact ground-state density. The first approximation made in this theory is the Born-Oppenheimer approximation, which decouples electron and atomic wavefunctions. With an additional Kohn-Sham approximation, the functional for the electronic energy can be expressed in the following form:

$$E_{tot}\left[n\right] = T_s\left[n\right] + E_{ext}\left[n\right] + E_H\left[n\right] + E_{xc}\left[n\right], \tag{1.8}$$

where $T_s[n]$ is the non-interacting kinetic energy, $E_{ext}[n]$ the potential energy due to interaction with the ions, $E_H[n]$ the classical electrostatic interaction (Hartree) term, and $E_{xc}[n]$ the exchange-correlation energy. So far, the exact form of the exchange-correlation functional, which contains all the complexity of the quantum many-body interactions, is unknown. Fortunately, several suitable approximations have been found which allow practical calculations. The most common approximations are the local-density approximation (LDA) and generalized gradient approximation (GGA). LDA is based on the assumption that the exchange and

correlation depends solely on the electron density at each point in space. GGA includes gradient corrections to LDA[24]. The correlation energy of the electron gas has been calculated with Quantum Monte Carlo[25]. For the low (n→0) and high (n→∞) density limit, exact forms of electron correlation are known[26,27].

Practical DFT calculations typically proceed in the context of Kohn-Sham theory. This theory invokes a fictitious system of non-interacting particles with the same ground-state electron density and total energy as the real system of interacting particles. By using this system of non-interacting particles, feasible DFT calculations become possible. The motion of these non-interacting particles in the effective Kohn-Sham potential is described by the Kohn-Sham equation:

$$\left[-\frac{\hbar^2\nabla^2}{2m}+\nu_{KS}\left[n\left(\mathbf{r}\right)\right]\right]\varphi_i\left(\mathbf{r}\right)=\varepsilon_i\varphi_i\left(\mathbf{r}\right), \tag{1.9}$$

where ε_i and $\varphi_i(\mathbf{r})$ are the energy eigenvalues and wavefunctions of the Kohn-Sham orbitals. The Kohn-Sham potential is a local potential that depends on the density and is given by

$$\nu_{KS}\left[n\left(\mathbf{r}\right)\right]=\nu_{ext}\left[n\left(\mathbf{r}\right)\right]+\nu_{H}\left[n\left(\mathbf{r}\right)\right]+\nu_{xc}\left[n\left(\mathbf{r}\right)\right], \tag{1.10}$$

where $\nu_{ext}[n(\mathbf{r})]$ is the external potential (e.g., the potential of the ions), $\nu_H[n(\mathbf{r})]$ is the Hartree term, and $\nu_{xc}[n(\mathbf{r})]$ is the exchange-correlation potential. The electron density of the Kohn-Sham system,

$$n\left(\mathbf{r}\right)=\sum_{i}^{ooc}\left|\varphi_i\left(\mathbf{r}\right)\right|^2, \tag{1.11}$$

obtained from the solution of Eq. 1.9 is then inserted in Eq. 1.8 to yield the total energy of the electron system.

The energy in Eq. 1.8 depends on the positions of the nuclei. By minimizing the total energy, the unit cell volume and atomic positions are optimized to yield equilibrium lattice parameters and atomic geometries. DFT within the LDA or GGA for the exchange-correlation functional provides accurate structural properties for group-III nitride materials[28]. The lattice parameters of the wurtzite crystal structure for AlN, GaN, and InN are listed in Table 1.1. The calculated results are in good agreement with experiment and the deviations are on the order of 1% error that is typical of these functionals.

Although DFT with present-day exchange-correlation functionals performs exceptionally well in predicting the ground-state properties of materials, it was not intended to describe properties that involve electronic excitations. One of the most serious drawbacks of traditional DFT functionals, in particular LDA and GGA, is that the band gaps of Kohn-Sham band structures are severely underestimated (typically by 50%). Several schemes have been developed to address this problem, including the incorporation of exact exchange in these functionals and applying many-body perturbation theory on top of traditional DFT calculations. It has been shown that the electronic properties of nitride semiconductors can be well reproduced by these more advanced methods.

Table 1.1: Equilibrium lattice parameters (a and c) and band gaps (E_g) obtained with LDA, GGA, and HSE (with a mixing parameter $\alpha = 25\%$). Experimental lattice parameters at $T = 300$ K and band gaps (without phonon effects) are taken from Refs. 29 and 30.

	Method	a (Å)	c (Å)	u	E_g (eV)
AlN	LDA	3.092	4.950	0.3818	4.40
	GGA	3.127	5.021	0.3812	4.10
	HSE	3.102	4.971	0.3819	5.64
	Exp.	3.112	4.982	-	6.25
GaN	LDA	3.155	5.145	0.3764	2.12
	GGA	3.215	5.240	0.3766	1.74
	HSE	3.182	5.173	0.3772	3.24
	Exp.	3.190	5.189	-	3.51
InN	LDA	3.504	5.670	0.3784	< 0
	GGA	3.573	5.762	0.3792	< 0
	HSE	3.548	5.751	0.3796	0.68
	Exp.	3.540	5.706	-	0.78

1.4.2 Screened exchange: hybrid functionals

To address the band-gap problem, recent developments in exchange-correlation functionals include the incorporation of exact exchange in the so-called hybrid functionals. The hybrid approach to constructing density functional approximations was introduced by Axel Becke. This approach originated in quantum chemistry, and in particular the B3LYP functional, which combines Becke's exchange functional (B3) with Lee, Yang, and Parr (LYP) correlation, has been quite successful in describing structural properties and energetics of molecules[31].

Following Becke's idea, Heyd, Scuseria, and Ernzehof (HSE)[32] proposed an alternative form, in which also a certain amount of exact Hartree-Fock exchange is mixed with the GGA functional. By introducing a screening length with an error function, this range-separated hybrid functional treats the exchange energy differently in short and long range. In practice, the separation of short-range (SR) and long-range (LR) parts is realized by

$$\frac{1}{r} = \underbrace{\frac{erfc\,(\mu r)}{r}}_{SR} + \underbrace{\frac{erf\,(\mu r)}{r}}_{LR}. \tag{1.12}$$

Here, μ is the actual controlling parameter for the range-separation. In short range, the GGA exchange function is mixed with Hartree-Fock exchange in a 3:1 ratio, while the long-range exchange and correlation are solely described by the GGA functional:

$$E_{XC}^{HSE} = \alpha E_X^{HF,SR}(\mu) + (1-\alpha)\, E_X^{PBE,SR}(\mu) + E_X^{PBE,LR}(\mu) + E_C^{PBE}. \tag{1.13}$$

Here, α defines the percentage of Fock exchange included. The structural parameters for the group-III nitrides obtained with the HSE hybrid functional, as shown in Table 1.1[33], are in even better agreement with experiment than LDA or GGA. Most importantly, the HSE functional significantly reduces the band-gap error of local and semilocal DFT functionals. As shown in Table 1.1, the band gaps calculated with HSE are in much better agreement with experiment than LDA or GGA. However, all these advantages come at a price. Due to the expensive calculations of four-center integrals for the Hartree-Fock potential, typical HSE calculations require at least an order of magnitude more computational resources than standard DFT calculations. Overall, the hybrid-functional approach is a powerful technique that can yield reliable structural and electronic properties of nitride semiconductors.

1.4.3 Electronic excitations: GW method

Many-body perturbation theory within the GW approximation has been the method of choice for calculating quasiparticle band structures while taking into account the electronic excitations in solids[34,35,36,37]. Band structure studies within the GW method usually start with a DFT calculation for the ground-state configuration $|N, 0\rangle$ of the electronic system of N electrons without excitations. Based on the ground-state configuration $|N, 0\rangle$, the one-body Green's function is described

by the following equation:

$$G_1(1,2) = -i\left\langle N,0\left|T\left(\psi(1)\,\psi^+(2)\right)\right|N,0\right\rangle. \tag{1.14}$$

It describes particle-like excitation processes in which an electron is removed from the system ($N \to N-1$) or added to it ($N \to N+1$). The band structure of a material is given by the solution of the one-particle Green's function G_1, which may be obtained from a Dyson-type equation of motion,

$$\left[H_0 + \sum(E)\right] G_1(E) = EG_1(E). \tag{1.15}$$

In this equation, $H_0 = T_0 + V_{ext} + V_{Coul}$ is the Hamiltonian in the Hartree approximation. The exchange and correlation effects among the electrons are described by the electron self-energy operator $\sum(E)$. The self-energy contains all the complexity of exchange and correlation of the many-electron system and can be expanded in terms of Feynman diagrams with respect to the screened Coulomb interaction. The GW approximation keeps only the first-order term of the self-energy:

$$\sum = G_1 W, \tag{1.16}$$

where G_1 is the one-particle Green's function and W the screened Coulomb interaction. The Green's function and the screened Coulomb interaction are calculated from the Kohn-Sham wavefunctions $\left|\psi_m^{DFT}\right\rangle$ and eigenvalues E_m^{DFT}. The dielectric function needed to describe the screened interaction between charge carriers

is then expressed within the random-phase approximation (for details, see Refs. 35,38,39). The calculation of the dielectric function makes the GW approach computationally very demanding, and several computational techniques and approximations have been developed to make these calculations tractable[40].

In practical calculations, the general form of the equation for the one-particle Green's function is transformed into the corresponding Dyson equation for the quasiparticles of the system with quasiparticle electron and hole states:

$$\left[H_0 + \sum \left(E_m^{QP}\right)\right] \left|\psi_m^{QP}\right\rangle = E_m^{QP} \left|\psi_m^{QP}\right\rangle . \tag{1.17}$$

In practice, an assumption is frequently made that the DFT and QP wavefunctions are the same. With this approximation, Eq. 1.17 is evaluated in the basis given by the DFT states $\left|\psi_m^{DFT}\right\rangle$ and the quasiparticle energy of a state m is thus given by

$$E_m^{QP} = E_m^{DFT} + \left\langle \psi_m \left| \sum \left(E_m^{QP}\right) - V_{xc} \right| \psi_m \right\rangle , \tag{1.18}$$

where $V_{xc}(\mathbf{r})$ is the DFT exchange-correlation potential. In principle, the quasiparticle energies and wavefunctions can be used to update the Green's function and the screening to do self-consistent calculations. Detailed discussion of quasiparticle wavefunctions and the advantages and disadvantages of self-consistency is available the literature[37,41]. In practice, GW calculations for bulk materials are usually performed as a one-shot correction, a procedure denoted as G_0W_0.

Although DFT with LDA or GGA are most commonly used as the starting

point for G_0W_0 in solids, this is sometimes a bad starting point. For the nitrides this becomes most apparent for the band gap of InN, for which LDA and GGA result in an overlap between the conduction and the valence bands and thus an effectively metallic state, as shown in Table 1.1. In this case, orbital-dependent functionals provide a better description for certain materials. As one of the orbital-dependent methods, the optimized effective potential approach applied to exact-exchange (OEPx) produces the best local potential to the non-local Fock operator[42]. In OEPx(cLDA) LDA correlation is added to OEPx. Unlike in LDA and GGA the self-interaction error in OEPx(cLDA) is greatly reduced, and the approach correctly predicts InN to be semiconducting with the right band ordering in the wurtzite phase. It hence provides a better starting point for GW calculations.

1.4.4 Electronic excitations: Bethe-Salpeter equation

In this section, we will discuss theoretical methods to investigate the electron-hole interaction in optical excitation. The problem we are interested in is electron-hole excitations $|N, 0\rangle \rightarrow |N, S\rangle$ that do not change the total number of electrons in the system. This excitation process is relevant to optical absorption processes and can be investigated theoretically by writing down the two-particle Green's function for an electron-hole pair. The equation of motion of the two-particle Green's function is known as the Bethe-Salpeter equation (BSE). For a more

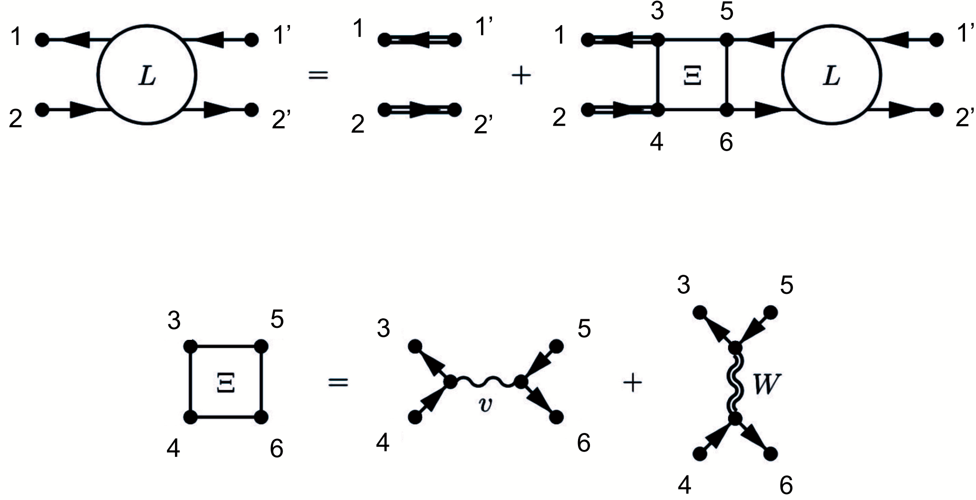

Figure 1.4: Schematic diagram of many-body interactions in the Bethe-Salpeter equation.

detailed discussion of the formalism we refer to the work by Strinati (see Ref. 43, 44). Here we only give a brief introduction of the BSE method.

From Ref. 43 and 44, the Bethe-Salpeter equation is expressed in the following form:

$$L\left(12;1'2'\right) = L_0\left(12;1'2'\right) + \int d\left(3456\right) L_0\left(12;1'2'\right) \times K\left(35;46\right) L62\left(12;52'\right). \tag{1.19}$$

Here $L_0\left(12;1'2'\right) = G_1\left(1,2'\right)G_1\left(2,1'\right)$ corresponds to free electron-hole pairs

without interaction. $L(12;1'2')$ is the electron-hole correlation function and $K(35;46)$ is the electron-hole interaction kernel. The schematic diagram of many-body interactions in the BSE is shown in Fig. 1.4. In practice, we transform all quantities from the continuous position variables into the basis given by the single-particle wavefunctions of the electron and hole. In this way, the equation of motion becomes a generalized eigenvalue problem[43,44]:

$$(E_c - E_v)\, A_{vc}^S + \sum_{v'c'} K_{vc,v'c'}^{AA}\,(\Omega_S) A_{v'c'}^S = \Omega_S A_{vc}^S. \tag{1.20}$$

In this expression, S denotes the correlated electron-hole excitations of the system with the excitation energies Ω_S. The matrix elements of the electron-hole interaction kernel K are given by

$$K_{vc,v'c'}^{AA}\,(\Omega_S) = i \int d\,(3456)\, \psi_v\,(\mathbf{x}_4) \psi_c^*\,(\mathbf{x}_3)\, K\,(35,46;\Omega_S)\, \psi_{v'}^*\,(\mathbf{x}_5)\, \psi_{c'}\,(\mathbf{x}_6)\,. \tag{1.21}$$

This is equivalent to expanding the excited states in electron-hole pair configurations as:

$$|N,S\rangle = \sum_v^{\text{hole}} \sum_c^{\text{elec}} A_{vc}^S \hat{a}_v^\dagger \hat{b}_c^\dagger\, |N,0\rangle =: \sum_v^{\text{hole}} \sum_c^{\text{elec}} A_{vc}^S\, |vc\rangle\,, \tag{1.22}$$

where $\hat{a}_v^\dagger$ and $\hat{b}_c^\dagger$ create a hole or an electron, respectively, starting from the many-body ground state $|N,0\rangle$. The electron-hole interaction kernel K is given by

$$K\,(35;46) = \frac{\delta\,[V_{Coul}\,(3)\,\delta\,(3,4) + \Sigma\,(3,4)]}{\delta G_1\,(6,5)}. \tag{1.23}$$

In order to be consistent with the quasiparticle band-structure calculation, we again employ the GW approximation for the self-energy operator Σ. Under

the additional assumption that the derivative of the screened interaction W with respect to G_1 can be neglected[43,44] one obtains

$$K(35;46) = -i\delta(3,4)\,\delta\left(5^-,6\right)v(3,6) + i\delta(3,4)\,\delta(4,5)\,v\left(3^+,4\right) \quad (1.24)$$

$$= K^x(35;46) + K^d(35;46)\,. \quad (1.25)$$

The term K^x, which results from the Coulomb potential, is usually called the exchange term; while the term K^d, which results from the screened-exchange self-energy, has the form of a direct interaction term. Note that $K^d(35;46)$ involves the screened Coulomb interaction W while $K^x(35;46)$ contains the bare Coulomb interaction v. The direct interaction term $K^d(35;46)$ is responsible for the attractive nature of the electron-hole interaction and the formation of bound electron-hole states (i.e., excitons). The exchange interaction term $K^x(35;46)$, on the other hand, controls details of the excitation spectrum.

The interaction of an external light field with excitations in the system is described by the macroscopic transverse dielectric function $\epsilon(\omega)$[45]. Its imaginary part $\epsilon_2(\omega)$ is

$$\epsilon_2(\omega) = \frac{16\pi e^2}{\omega^2}\sum_S \left|\vec{\lambda}\cdot\langle 0\,|\vec{v}|\,S\rangle\right|^2 \delta(\omega-\Omega_S)\,, \quad (1.26)$$

where $\vec{\lambda} = \vec{A}/|\vec{A}|$ is the polarization vector of the light and $\vec{v} = i/\hbar[H,\vec{r}]$ is the single-particle velocity operator.

Without the electron-hole interaction, the excitations are given by the well-

known expression[46]

$$\epsilon_2^{(0)}(\omega) = \frac{16\pi e^2}{\omega^2} \sum_{v,c} \left| \vec{\lambda} \cdot \langle v \left| \vec{v} \right| c \rangle \right|^2 \delta \left(\omega - (E_c - E_v) \right), \tag{1.27}$$

where $v(c)$ denotes valence (conduction) states. With the electron-hole interaction, different electron-hole configurations $|vc\rangle$ are coupled in the excitations $|S\rangle$:

$$\langle 0 \left| \vec{v} \right| S \rangle = \sum_{v}^{\text{hole}} \sum_{c}^{\text{elec}} A_{vc}^{S} \langle v \left| \vec{v} \right| c \rangle . \tag{1.28}$$

The above formula indicates that the optical transition matrix elements are given by a coherent sum of the transition matrix elements of the contributing electron-hole pair configurations and the weight of these configurations is decided by the coupling coefficients A_{vc}^{S}. Former calculations for bulk semiconductors indicate that the excitonic effect is crucial to obtain a reliable absorption spectrum in good agreement with experimental data. In the Sec. 3.3 we will show how the excitonic effect changes the absorption spectrum of defects in nitride semiconductors.

1.4.5 Band structures and k·p method

The k.p method represents an approach to study the band structures of nitride materials in a computationally feasible manner. The basic concept of this method is to describe the band structure with a basis of band states and consider the perturbation through symmetry analysis. This method has been first applied

by Seitz[47] and was later extended to study the band structure of semiconductors[48,49,50]. The original idea is that only the neighborhoods of the band extrema are important and the qualitative physics should be governed by the shape of the energy surfaces near the extrema. Thus $\mathbf{k}\cdot\mathbf{p}$ theory is commonly viewed and used as a perturbative approach as demonstrated by Kane[49]. Later on it was demonstrated by Cardona and Pollak[50] that $\mathbf{k}\cdot\mathbf{p}$ band structure can go beyond the neighborhood of band extrema, and realistic band structures for Si and Ge were obtained using a full-zone $\mathbf{k}\cdot\mathbf{p}$ theory.

The concept of the $\mathbf{k}\cdot\mathbf{p}$ method can be simply derived from the one-electron Schrödinger equation:

$$H\phi_n(\mathbf{r}) = \left(\frac{p^2}{2m} + V(\mathbf{r})\right)\phi_n(r) = E_n\phi_n(\mathbf{r}). \tag{1.29}$$

Here H denotes the one-electron Hamiltonian and $V(\mathbf{r})$ the local periodic lattice potential. The wavefunction of an electron in an eigenstate labeled n and its energy are denoted by $\phi_n(\mathbf{r})$ and E_n, respectively.

In a periodic potential Bloch theorem applies, and the wavefunction can be expressed as

$$\phi_{n\mathbf{k}}(\mathbf{r}) = e^{i\mathbf{k}\cdot\mathbf{r}}u_{n\mathbf{k}}(\mathbf{r}), \tag{1.30}$$

where n is the band index and $\mathbf{k}$ is the wave vector. The Bloch wavefunction $u_{n\mathbf{k}}(\mathbf{r})$ has the periodicity of the lattice. By substituting $\phi_{n\mathbf{k}}(\mathbf{r})$ into the Schrödinger

equation, an equation for $u_{n\mathbf{k}}(\mathbf{r})$ is obtained

$$\left(\frac{p^2}{2m} + V(\mathbf{r}) + \frac{\hbar\mathbf{k}\cdot\mathbf{p}}{m}\right) u_{n\mathbf{k}}(\mathbf{r}) = \left(E_n - \frac{\hbar^2 k^2}{2m}\right) \phi_n(\mathbf{r}). \tag{1.31}$$

Considering any fixed wavevector $\mathbf{k} = \mathbf{k_0}$, the above equation yields a complete set of eigenfunctions $u_{n\mathbf{k_0}}$. Hence, the wavefunction $\phi_{n\mathbf{k}}(\mathbf{r})$ at $\mathbf{k}$ can be expanded in terms of $u_{n\mathbf{k_0}}$

$$\phi_{n\mathbf{k}}(\mathbf{r}) = \sum C_{n,n}(\mathbf{k}, \mathbf{k_0}) e^{i\mathbf{k}\cdot\mathbf{r}} u_{n\mathbf{k_0}}. \tag{1.32}$$

At $\mathbf{k} = \mathbf{k_0} + \mathbf{\Delta k}$, we can treat the term $\hbar\Delta\mathbf{k}\cdot\mathbf{p}/\mathbf{m}$ in Eq. 1.31 as a perturbation. Once $E_{n\mathbf{k_0}}$ and $u_{n\mathbf{k_0}}$ are known, the wavefunctions $\phi_{n\mathbf{k}}(\mathbf{r})$ and the eigenenergies $E_{n\mathbf{k}}$ at any $\mathbf{k}$ vector in the vicinity of $\mathbf{k_0}$ can be obtained. This method for calculating the band structure is known as the $\mathbf{k}\cdot\mathbf{p}$ method.

$\mathbf{k}\cdot\mathbf{p}$ theory works quite well when calculating the band structure in the vicinity of any given point $\mathbf{k_0}$ if the matrix elements of $\mathbf{p}$ between the wavefunctions and the eigenenergies at $\mathbf{k_0}$ are known. Actually, when using a sufficiently large number of $u_{n\mathbf{k_0}}$ to approximate a complete set of basis functions, the band structure over the entire first Brillouin zone can also be calculated by diagonalizing the $\mathbf{k}\cdot\mathbf{p}$ Hamiltonian numerically[50].

Using the $\mathbf{k}\cdot\mathbf{p}$ method for semiconductor systems, one can construct the $\mathbf{k}\cdot\mathbf{p}$ Hamiltonian by considering symmetry invariants to obtain analytical expressions for the band dispersion and the effective masses. The $\mathbf{k}\cdot\mathbf{p}$ method can also be used to model the impact of an external perturbation such as strain on the band

structures as described in detail by Bir and Pikus in their landmark book[51]. For nitride materials with the wurtzite structure, by employing the $\mathbf{k}\cdot\mathbf{p}$ perturbation Hamiltonian given by Bir and Pikus[51], we can obtain the band structure in the vicinity of the band extrema at the Γ point. As the band gap is quite large in nitride materials compared with the separation between the topmost three valence bands, it is straightforward to construct the Hamiltonian with a basis consisting of the topmost three valence bands (including the spin degree of freedom). The Hamiltonian for valence bands of the wurtzite crystal is given by the following 6×6 matrix:

$$H = \begin{bmatrix} F & 0 & -H^* & 0 & K^* & 0 \\ 0 & G & \Delta & -H^* & 0 & K^* \\ -H & \Delta & \lambda & 0 & I^* & 0 \\ 0 & -H & 0 & \lambda & \Delta & I^* \\ K & 0 & I & \Delta & G & 0 \\ 0 & K & 0 & I & 0 & F \end{bmatrix}, \tag{1.33}$$

where

$$F = \Delta_1 + \Delta_2 + \lambda + \theta,$$

$$G = \Delta_1 - \Delta_2 + \lambda + \theta,$$

$$H = i(A_6 k_z k_+ + A_7 k_+),$$

$$I = i(A_6 k_z k_+ - A_7 k_+),$$

$$K = A_5 k_+^2,$$

$$\Delta = \sqrt{2}\Delta_2,$$

$$\lambda = A_1 k_z^2 + A_2 k_\perp^2,$$

$$\theta = A_3 k_z^2 + A_4 k_\perp^2,$$

$$k_+ = k_x + i k_y, k_\perp^2 = k_x^2 + k_y^2.$$

Here Δ_1 is the crystal-field interaction and Δ_2 is the spin-orbit interaction. A_1 to A_7 are Luttinger parameters which describe the band dispersion along different k directions. For unstrained wurtzite systems, the top three valence bands correspond to the heavy hole (HH), light hole (LH), and crystal-field split-off band (CH). The spin-orbit interaction is denoted by Δ_2 which is typically small (a few meV) in nitride materials. If we neglect spin-orbit interaction, the HH and LH band become doubly degenerate (Γ_6) and the CH band (Γ_1) is split off by crystal-field splitting. For the strained case, additional terms are included in the Hamiltonian and deformation potentials D_1 to D_6 are used to describe the effects of strain perturbation on band structures. By fitting the first-principles band structures with analytical solutions from $\mathbf{k}\cdot\mathbf{p}$ theory, band parameters and deformation potential parameters can be extracted[29]. These parameters are essential

inputs for device simulations of nitride-based light emitting devices.

1.4.6 Schrödinger-Poisson and drift-diffusion model

A schematic illustration of a typical multiple-quantum-well (MQW) nitride light-emitting diode is shown in Fig. 1.5. The active region, consisting of InGaN quantum wells and GaN barriers, is sandwiched between the n- and p-type GaN layers. The device is usually grown on top of a foreign substrate, typically sapphire or SiC. The n-type GaN layer doped with Si is deposited first, followed by the growth of InGaN quantum wells and GaN barriers, and finally the p-type Mg:GaN layer. Not shown in the figure are the transparent-oxide top contact and the AlGaN electron-blocking layer that is commonly employed to enhance electron capture in the quantum wells. Connecting the device to a power source injects electrons and holes into the quantum wells, where they recombine and produce light at the wavelength corresponding to the band gap of the alloy material.

In order to model the operation of light-emitting diode (LED) heterostructures based on wurtzite semiconductors group-III nitrides, a one-dimensional Schrödinger-Poisson solver is applied which accounts for specific features of the wurtzite materials including piezoelectric and spontaneous polarization.

Electrons and holes obey the Fermi-Dirac statistics. The respective carrier concentrations n and p are related to the electric potential φ , electron and hole

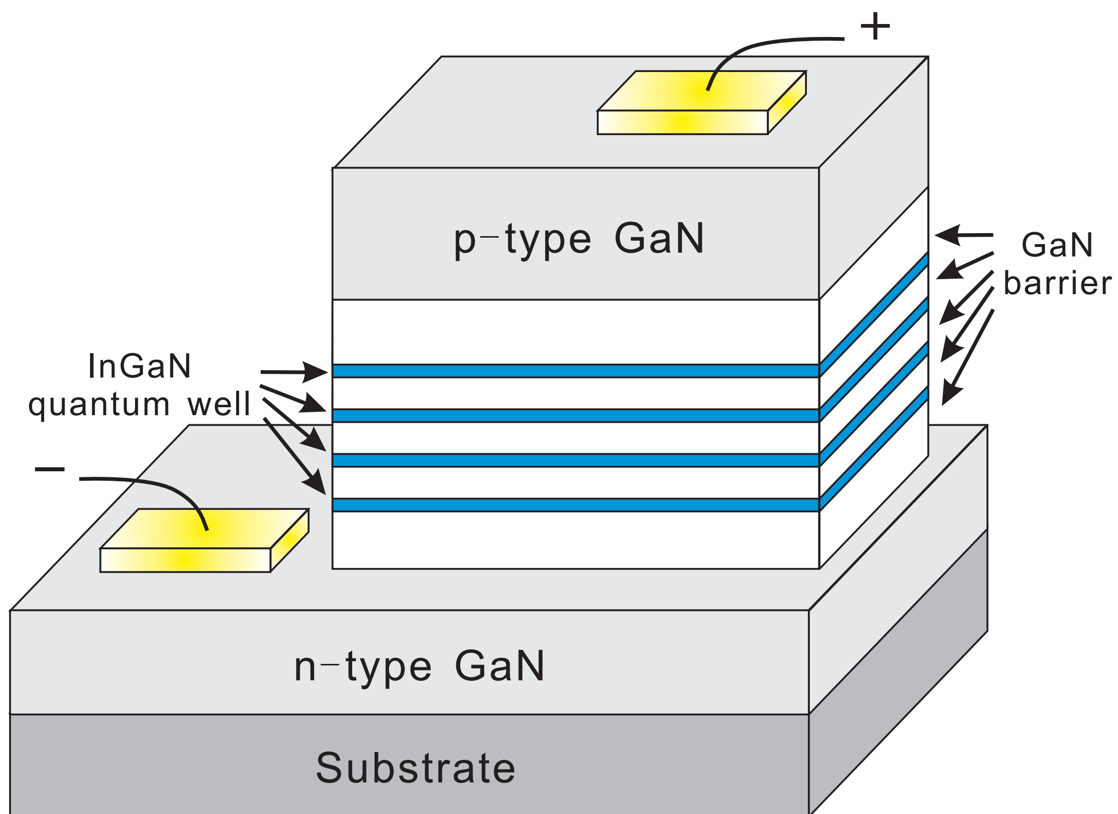

Figure 1.5: Schematic of a typical multiple-quantum-well InGaN/GaN light-emitting diode.

quasi-Fermi levels F_n and F_p , the CBM E_C , and the VBM E_V by the equations

$$\begin{aligned} n &= N_C \cdot F_{1/2}\left(\tfrac{F_n - E_C + q\varphi}{kT}\right), \\ p &= N_V \cdot F_{1/2}\left(\tfrac{E_V - F_p + q\varphi}{kT}\right), \end{aligned} \tag{1.34}$$

where $F_n(\xi) = \frac{1}{\Gamma(\nu+1)} \int\limits_0^\infty \frac{x^\nu dx}{1+\exp(x-\xi)}$ is the Fermi integral, q is the electron charge, k is the Boltzmann constant, T is temperature, and N_C and N_V are the effective density of states in the conduction and valence bands, respectively,

$$\begin{aligned} N_C &= 2\left(\tfrac{m_n^{av} kT}{2\pi\hbar^2}\right)^{3/2}, \\ N_V &= 2\left(\tfrac{m_p^{av} kT}{2\pi\hbar^2}\right)^{3/2}. \end{aligned} \tag{1.35}$$

Here, m_n^{av} and m_p^{av} are the averaged electron and hole effective masses. Taking into account the conduction-band anisotropy, the averaged electron effective mass is $m_n^{av} = (m_n^{av}\sqrt{m_n^c})^{2/3}$, where m_n^{av} and m_p^{av} are the effective masses along the a and c axes, respectively. For holes, one has to consider the complex valence-band structure and splitting of the valence bands at the center of the Brillouin zone. If the splitting can be neglected, the hole density of states can be expressed as

$$\begin{aligned} N_V &= N_{hh} + N_{lh} + N_{so}\ , \quad N_{so} = 2\ m_{so}^a\,(m_{so}^c)^{1/2}\left(\tfrac{kT}{2\pi\hbar^2}\right)^{3/2} \\ N_{lh} &= 2m_{lh}^a\,(m_{lh}^c)^{1/2}\left(\tfrac{kT}{2\pi\hbar^2}\right)^{3/2}\ , \quad N_{so} = 2m_{so}^a\,(m_{so}^c)^{1/2}\left(\tfrac{kT}{2\pi\hbar^2}\right)^{3/2}, \end{aligned} \tag{1.36}$$

where m_{hh} , m_{lh} , and m_{so} are the effective masses of heavy, light, and split-off holes, respectively.

The concentrations of ionized donors N_D^+ and acceptors N_A^- are related to the total impurity concentrations N_D and N_A as

$$N_D^+ = \frac{N_D}{1 + g_D \exp(\frac{F_n - E_C + E_D + q\varphi}{kT})}, N_A^- = \frac{N_A}{1 + g_A \exp(\frac{E_V + E_A - F_p - q\varphi}{kT})}. \tag{1.37}$$

Here, $g_D = 2$ and $g_A = 4$ are the degeneracy factors, and E_D and E_A are the activation energies of electrons and holes, respectively. The Poisson equation is employed for computation of the distribution of the electric potential in an LED structure:

$$\frac{d}{dz}\left(P_z^0 - \varepsilon_0\varepsilon_{33}\frac{d\varphi}{dz}\right) = q\left[N_D^+ - N_A^+ + p - n\right], \tag{1.38}$$

where ε_0 is the dielectric permittivity of vacuum, and ε_{33} is the relevant component of the static dielectric constant tensor of a wurtzite semiconductor. The vector of electrostatic induction has then only the z-component $D_z = P_z^0 - \varepsilon_0\varepsilon_{33}\frac{d\varphi}{dz}$.

At the internal abrupt heterointerfaces $z = z_i$

$$\varphi\left(z_i - 0\right) = \varphi\left(z_i + 0\right) \quad and \quad D_z\left(z_i - 0\right) = D_z\left(z_i + 0\right). \tag{1.39}$$

On the left edge of the LED structure

$$\varphi\left(L\right) = 0. \tag{1.40}$$

On the right edge of the LED structure

$$\varphi\left(R\right) = U_c + U_b, \tag{1.41}$$

where U_b is the bias and U_c is the contact potential determined from the equality of the quasi-Fermi levels on the both edges of the structure at zero bias. For a p-n homojunction, where the left edge of the structure is p-doped and the right edge is n-doped, the contact potential is nearly equal to the energy gap, i.e., $U_c \approx E_G$.

Under steady-state conditions, the electron and hole fluxes, $\mathbf{J}_n$ and $\mathbf{J}_p$, are governed by the continuity equations

$$\begin{aligned} \nabla \cdot \mathrm{J_n} + R = 0, \\ \nabla \cdot \mathrm{J_p} + R = 0, \end{aligned} \tag{1.42}$$

where R is the recombination rate of non-equilibrium carriers. The electron and hole current densities are related to the fluxes as $\mathbf{j}_\mathrm{n} = -q\mathbf{J}_\mathrm{n}$ and $\mathbf{j}_\mathrm{p} = +q\mathbf{J}_\mathrm{p}$. In turn, the carrier fluxes depend on the gradients of the quasi-Fermi levels as

$$\begin{aligned} \mathbf{J}_\mathrm{n} = -\tfrac{\mu_n n}{q} \nabla F_\mathrm{n}, \\ \mathbf{J}_\mathrm{p} = -\tfrac{\mu_p n}{q} \nabla F_\mathrm{p}. \end{aligned} \tag{1.43}$$

Here, μ_n and μ_p are the electron and hole mobilities, respectively. This form of transport equations written for the variables $\mathbf{J}_\mathrm{p}$, F_n and F_p allows consideration of conventional LED structures with abrupt interfaces as well as with graded composition. In our case, $\nabla \equiv d/dz$ and $\mathbf{J}_\mathrm{n} = \mathbf{e}_\mathrm{z} J_\mathrm{n}$, $\mathrm{J_p} = \mathbf{e}_\mathrm{z} J_\mathrm{p}$. For practical use of this method, proper boundary conditions at the contacts are applied.

Using the Schrödinger-Poisson solver, we carry out device simulations and obtain LED band diagrams as a function of bias, the electron and hole distribution inside a heterostructure, the electric field distribution in the structure, and the wavefunction overlap that affects the electron-hole recombination. In Sec. 4.1, we demonstrate how the strain-induced polarization field affects wavefunction overlap in the quantum wells of the c-plane and nonpolar plane LEDs and is related to the droop problem. In Sec. 4.2, we elucidate the mechanisms by which modification

of GaN barriers by Mg doping benefits hole transport, In Sec. 4.3, we show that the emission wavelength shift under current injection is also related with quantum well potential profile and the polarization field inside quantum wells.

The drift-diffusion model allows us to calculate the current density through the diode at a certain bias. In practice, although the carrier transport is treated semi-empirically, this model has been widely used for nitride device simulations to explain experimental observations in nitride-based heterostructures. However, in the drift-diffusion model, the quantum effect of the carrier tunneling between quantum wells is not taken into account. The lack of such quantum effects in this model is the probable cause of the discrepancy between theoretical predictions and experimental observations, particularly the difference in turn-on voltage and current.

Chapter 2

Strain effects in group-III nitrides and alloys

2.1 Introduction

The group-III nitride semiconductors AlN, GaN, InN, and their alloys are already extensively used as lighting emitting diodes (LEDs)[52] and laser diodes (LDs)[53] from the visible spectrum to the deep ultra-violet(UV)[54,55]. Applications of the nitride semiconductors in solid state lighting, however, are currently limited by several inherent factors. For example, the electron and hole wavefunctions in traditional *c*-plane (polar plane) quantum wells (QWs) are separated by the spontaneous and piezoelectric polarization which lowers the radiative recombination rate (quantum confined Stark effect[56]). As a result, the external quantum

efficiency of the *c*-plane InGaN QWs decreases rapidly as the In composition increases. Recently, semipolar and nonpolar InGaN/GaN quantum wells(QWs) have been proposed as promising candidates for high-efficiency light emitters. It has been theoretically predicted that, by changing the growth orientation normal to nonpolar and semipolar planes, the strain-induced piezoelectric polarization can be greatly reduced or even eliminated[20].

One effect of the interface between dissimilar nitride materials is the development of strain. The active regions in nitride-based light emitting devices are made of heterostructures such as the InGaN/GaN or AlGaN/GaN MQW structures. Vegard's law predicts that the equilibrium lattice constant of the alloy will be at a linearly interpolated value between the two extreme phases. Due to the large lattice mismatch (3.5% between AlN and GaN and 11% between InN and GaN), strain is present in the nitride alloy layers pseudomorphically grown on GaN substrates. Strain affects the group-III nitride device properties in several ways: (a) The strain changes the absolute positions of VBM and CBM, and hence modifies the quantum-well depth and the confinement of electrons and holes in the active region. (b) Strain induces piezoelectric polarization in InGaN or AlGaN QWs[20,57,58] which greatly lowers the electron-hole overlap and hence the radiative recombination rate. (c) In *c*-plane InGaN/GaN devices, the biaxial in-*c*-plane stress modifies the valence-band structures of nitride alloys, and changes the transition energies and effective masses of carriers. For example, experimental

observations reveal that the band gaps of the *c*-plane InGaN alloys show strong dependence on In composition and stain effects plays a role[59,60,61]. (d) In non-polar and semipolar QWs, the biaxial stress coming from the substrate induces anisotropic strain, which drastically modifies the subband structures and wave-function character[62,63,64,65] and induces the polarized light emission[58,66].

The effects of strain on band structures of group-III nitrides and their alloys can be described by deformation potential theory. In this theory, the effect of the strain perturbation on band structure is characterized by the deformation potential, which is defined as the linear coefficient of the change of band energies under strain. It has been demonstrated that the effects of residual strain in the epilayers can explain the observed values of optical transition energies in GaN through deformation potential theory[67,68,69]. In order to quantify the strain effects on band structures of InGaN or AlGaN alloys, accurate deformation potential parameters for all three nitrides are needed.

So far, most of experimental data on deformation potentials of GaN[69,70,71,72] and InN[72] have been obtained by a combination of x-ray and optical measurements from the change of optical transition energies under the biaxial stress induced by the *c*-plane substrate. However, the accurate determination of deformation potentials by this experimental approach is difficult. One of the main problems is that the uniaxial and biaxial components cannot be applied separately and the measurement only gives a combination of several deformation potentials. The

quasicubic approximation[51] is further needed to extract the deformation potentials from those combined data. Another issue is that the determination of the out-of-plane strain component is dependent on the numerical values of the elastic stiffness constants. As shown in Table 2.1, the experimental deformation potential data of GaN scatter over a very large range. Another possible experimental approach is to carry out optical measurements of nitride systems under uniaxial stress. The advantage of this approach is that various strained environments can be introduced in the system of interest, and therefore deformation potentials are obtained without the quasicubic approximation. Such techniques have recently been used to obtain the deformation potentials of GaN[73]. For AlN, until now no experimental deformation potential data is available.

Theoretical data of deformation potentials are available for GaN and AlN systems, but the data also exhibit a large uncertainty, as shown in Table 2.1. The large deviations in the band-gap related deformation potentials ($a_{cz} - D_1$, $a_{ct} - D_2$) are attributed to the band-gap problem of DFT in LDA or GGA. Earlier theoretical work has shown that the relaxation of the internal displacement parameter u is critical in determining the crystal-field splitting and the related deformation potentials (D_3 and D_4). Because of the lack of the relaxation, some of the earlier calculations may not have been completely converged[75]. Due to pronounced non-linear dependence of the transition energies on lattice parameters, the equilibrium lattice parameters around which the linear expansion is constructed also affect the

Table 2.1: Literature results for deformation potentials (eV) of wurtzite GaN.

Method	$a_{cz} - D_1$	$a_{ct} - D_2$	D_3	D_4	D_5	D_6
Calc.[74]	-	-	2.99	-1.50	-2.04	-
Calc.[75]	-4.78	-6.18	1.40	-0.70	-	-
Calc.[76]	-3.10	-11.2	8.20	-4.10	-4.70	-
Calc.[77]	-	-	5.80	-3.25	-2.85	-
Calc.[78]	-6.11	-9.62	5.76	-3.04	-	-
Calc.[79]	-9.47	-7.17	6.26	-3.29	-	-
Calc.[80]	-6.02	-8.98	5.45	-2.97	-2.87	-3.95
Exp.[71]	-	-	8.82	-4.41	-	-
Exp.[70]	-6.50	-11.80	5.30	-2.70	-	-
Exp.[81]	-	-	6.80	-3.40	-3.30	-
Exp.[69]	-5.32	-10.23	4.91	-2.45	-	-
Exp.[82]	-	-	-	-	-3.60	-
Exp.[83]	-9.60	-8.20	1.90	-1.00	-	-
Exp.[73]	-6.50	-11.20	4.90	-5.00	-2.80	-3.10

deformation potentials greatly, as we will demonstrate later. For wurtzite InN, the theoretical calculations with LDA and GGA give a negative band gap and hence incorrect interaction between bands, which inhibit the theoretical determination of deformation potentials of InN.

In the present work, all of these shortcoming in previous theoretical approaches have been addressed. We study the strain effects on the band structure of wurtzite AlN, GaN, and InN using band-gap corrected first-principles approaches including hybrid functional[84] and quasiparticle G_0W_0 methods[85]. We show that the modification of band structures of nitrides due to strain perturbations is nonlinear. By applying different strains to wurtzite nitride systems, we obtain a complete set of deformation potentials from the linear regime around the experimental lattice parameters.

We then go on and use the semi-empirical $\mathbf{k}\cdot\mathbf{p}$ method. We explore the strain effects in InGaN alloys by applying our consistent set of deformation potentials and predict the band-structure modifications due to strain effects in polar c-plane, nonpolar m-plane and semipolar InGaN/GaN systems: (1) the effect of biaxial stress on band gaps of InGaN alloys grown on c-plane GaN substrates; (2) the relation between anisotropic in-c-plane biaxial strain on valence-band structures and the optical anisotropy of the light emitted from m-plane InGaN/GaN devices[86]; (3) the role of shear strain in the polarization ratio of emitted light and the polarization switching phenomenon in semipolar InGaN quantum wells[66,87].

2.2 Model and computational details

In this Section, we employ the **k·p** perturbation approach given by Bir and Pikus[51] as mentioned in Sec. 1.4 to obtain the analytical solutions of strain-induced band structure modifications in the vicinity of the Γ point. These solutions are then used to fit the first-principles band structures to extract deformation potential parameters. The strained Hamiltonian of the topmost three valence bands is given by the following 6×6 matrix:

$$H = \begin{bmatrix} F & 0 & -H^* & 0 & K^* & 0 \\ 0 & G & \Delta & -H^* & 0 & K^* \\ -H & \Delta & \lambda & 0 & I^* & 0 \\ 0 & -H & 0 & \lambda & \Delta & I^* \\ K & 0 & I & \Delta & G & 0 \\ 0 & K & 0 & I & 0 & F \end{bmatrix}, \tag{2.1}$$

where

$$F = \Delta_1 + \Delta_2 + \lambda + \theta,$$

$$G = \Delta_1 - \Delta_2 + \lambda + \theta,$$

$$H = i(A_6 k_z k_+ + A_7 k_+ + D_6 \varepsilon_{z+}),$$

$$I = i(A_6 k_z k_+ - A_7 k_+ + D_6 \varepsilon_{z+}),$$

$$K = A_5 k_+^2 + D_5 \varepsilon_+,$$

$$\Delta = \sqrt{2}\Delta_2,$$

$$\lambda = A_1 k_z^2 + A_2 k_\perp^2 + D_1 \varepsilon_{zz} + D_2(\varepsilon_{xx} + \varepsilon_{yy}),$$

$$\theta = A_3 k_z^2 + A_4 k_\perp^2 + D_3 \varepsilon_{zz} + D_4(\varepsilon_{xx} + \varepsilon_{yy}),$$

$$\varepsilon_+ = \varepsilon_{xx} - \varepsilon_{yy} + 2i\varepsilon_{xy}, \varepsilon_{z+} = \varepsilon_{xz} + i\varepsilon_{yz},$$

$$k_+ = k_x + ik_y, k_\perp^2 = k_x^2 + k_y^2.$$

Here Δ_1 is the crystal-field interaction and Δ_2 is the spin-orbit interaction. Note that the element H in this Hamiltonian is different in sign and by a i factor from that in Ref. 75. However, these differences do not produce any measurable physical effect. Previous work has shown that the same band structure is obtained from both theories[88]. We have also checked that such a difference in the Hamiltonian does not affect the dependence of band energies at the Γ point on the strain components, which is used to fit the band structures to extract the deformation potentials. Therefore, Chuang's theory and the Bir-Pikus theory are equivalent to each other. For an unstrained wurtzite system, the top three valence bands correspond to the heavy hole (HH), light hole (LH), and crystal-field split-off band (CH). The transition energies from the CBM to these three bands are denoted as

E_A, E_B, and E_C, respectively. Here we do not consider the spin-orbit interaction ($\Delta_2 = 0$) so that for the unstrained system the HH and LH band become doubly degenerate (Γ_6) and the CH band (Γ_1) is split off by the crystal-field splitting.

We first focus on those strain components that do not break the wurtzite symmetry, including the biaxial strain in the c plane ($\varepsilon_{xx} = \varepsilon_{yy}$) and uniaxial strain along the c axis (ε_{zz}). Such strain perturbations to the 6×6 $\mathbf{k}\cdot\mathbf{p}$ Hamiltonian do not split HH and LH bands, although they induce the energy shift of the conduction band and three valence bands at the Γ point:

$$\begin{aligned}
\Delta E_{CB} &= a_{cz}\varepsilon_{zz} + a_{ct}\varepsilon_{\perp}, \\
\Delta E_{HH/LH} &= (D_1 + D_3)\varepsilon_{zz} + (D_2 + D_4)\varepsilon_{\perp}, \\
\Delta E_{CH} &= D_1\varepsilon_{zz} + D_2\varepsilon_{\perp},
\end{aligned} \tag{2.2}$$

yielding the following transition energies:

$$\begin{aligned}
E_{A/B} &= E_{A/B}(0) + (a_{cz} - D_1)\varepsilon_{zz} + (a_{ct} - D_2)\varepsilon_{\perp} \\
&\quad -(D_3\varepsilon_{zz} + D_4\varepsilon_{\perp}), \\
E_C &= E_C(0) + (a_{cz} - D_1)\varepsilon_{zz} + (a_{ct} - D_2)\varepsilon_{\perp}.
\end{aligned} \tag{2.3}$$

Here $\varepsilon_{\perp}$ (equal to $\varepsilon_{xx} + \varepsilon_{yy}$) and ε_{zz} are the strain components in and out of the c plane. From the slopes of the transition energies under biaxial strain in the c plane ($\varepsilon_{xx} = \varepsilon_{yy} \neq 0, \varepsilon_{zz} = 0$) we obtain the deformation potentials $a_{ct} - D_2$ and D_4, while $a_{cz} - D_1$ and D_3 can be obtained from the slope of transition energies under uniaxial strain along the c-axis ($\varepsilon_{xx} = \varepsilon_{yy} = 0, \varepsilon_{zz} \neq 0$).

The strain components mentioned above preserve the symmetry of the wurtzite crystal. The hexagonal symmetry can be broken by anisotropic strain in the c

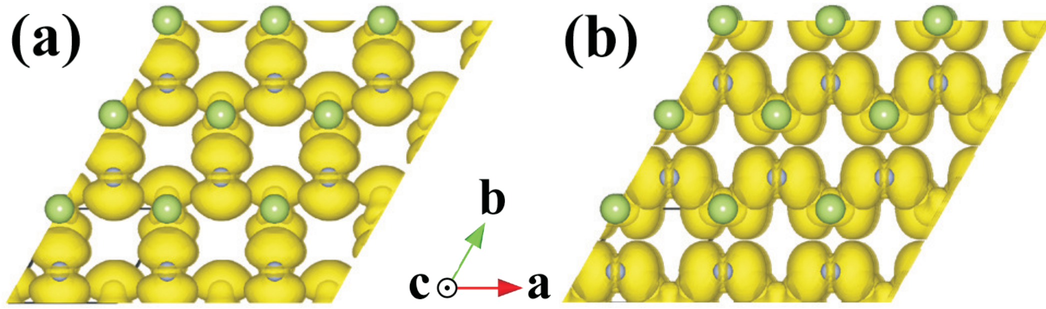

Figure 2.1: Partial charge density of (a) the highest and (b) the second highest valence band of wurtzite GaN under compressive uniaxial strain in the c plane.

plane, which is present in nonpolar and semipolar nitride alloys. For example, the uniaxial strain in the c plane ($\varepsilon_{yy} = \varepsilon_{zz} = 0$, $\varepsilon_{xx} \neq 0$) changes the crystal symmetry from C_{6v} to C_{2v}. Without spin-orbit splitting, the original 6×6 Hamiltonian reduces to a 3×3 matrix. The anisotropic strain in the c plane lifts the degeneracy of the Γ_6 states and yields the three eigenenergies:

$$\begin{aligned} E_1 &= E_{A/B}(0) + (D_2 + D_4)\varepsilon_{xx} + D_5\varepsilon_{xx}, \\ E_2 &= E_{A/B}(0) + (D_2 + D_4)\varepsilon_{xx} - D_5\varepsilon_{xx}, \\ E_3 &= E_C(0) + D_2\varepsilon_{xx}. \end{aligned} \tag{2.4}$$

Correspondingly the three eigenstates are:

$$\begin{pmatrix} 1 \\ 1 \\ 0 \end{pmatrix}, \begin{pmatrix} -1 \\ 1 \\ 0 \end{pmatrix}, \begin{pmatrix} 0 \\ 0 \\ 1 \end{pmatrix}. \tag{2.5}$$

The basis of the eigenvectors is:

$$
\begin{aligned}
|1\rangle &= |X + iY\rangle\,, \\
|2\rangle &= |X - iY\rangle\,, \\
|3\rangle &= |Z\rangle\,,
\end{aligned}
\tag{2.6}
$$

where the characters X/Y/Z means that the corresponding wavefunction has $p_x/p_y/p_z$ character. Obviously, the first eigenvector in Eq. 2.5 has p_x character while the second eigenvector has p_y character. We obtain the magnitude of the deformation potential D_5 from the slope of the energy splitting between the top two valence bands under anisotropic strain:

$$
\Delta E = |E_X - E_Y| = 2\,|D_5 \varepsilon_{xx}|\,. \tag{2.7}
$$

In order to decide the sign of D_5, we need to explore the symmetry character of the valence bands. Figure 2.1 shows the partial charge density of the topmost two valence bands of wurtzite GaN under uniaxial compressive strain along the x direction. The highest valence state exhibits p_x character, while the second highest state exhibits p_y character. This implies that D_5 is negative in GaN, in agreement with experimental observations[81]. Based on the calculated partial charge densities of AlN and InN (not shown here), we find that the D_5 values in AlN and InN are also negative.

Another strain component that may be present in semipolar nitride materials is shear strain (ε_{xz} and ε_{yz}). The corresponding deformation potential is D_6. By applying only the shear strain ε_{xz} in the wurtzite system, neglecting the spin-orbit

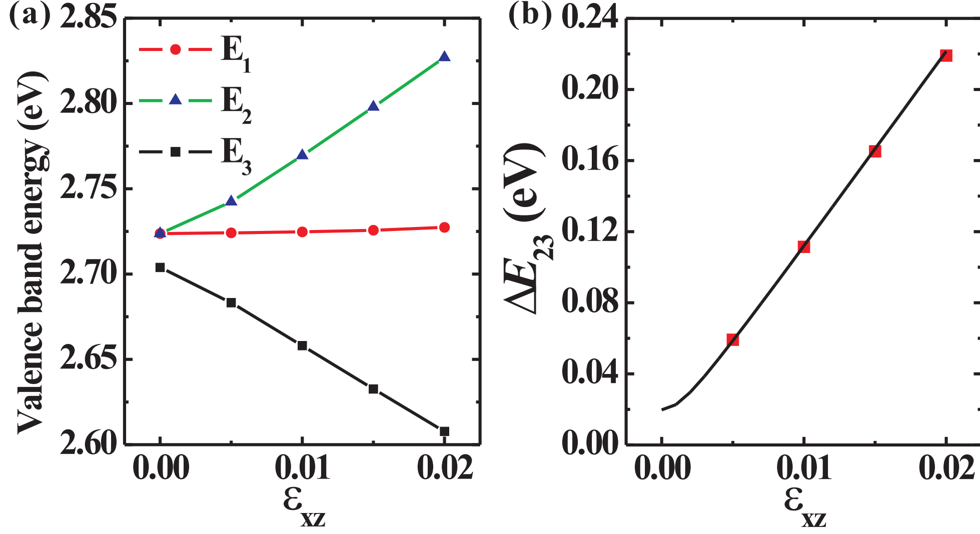

Figure 2.2: (a) Band energies of the topmost three valence bands of GaN under shear strain ε_{xz}. (b) Energy separation ΔE_{23} between valence band E_2 and E_3.

interaction, the topmost three valence-band eigenenergies at the Γ point are:

$$\begin{aligned} E_1 &= \Delta_{cr}, \\ E_2 &= \tfrac{\Delta_{cr}}{2} + \tfrac{\sqrt{\Delta_{cr}^2 + 8D_6^2\varepsilon_{xz}^2}}{2}, \\ E_3 &= \tfrac{\Delta_{cr}}{2} - \tfrac{\sqrt{\Delta_{cr}^2 + 8D_6^2\varepsilon_{xz}^2}}{2}. \end{aligned} \tag{2.8}$$

As shown in Fig. 2.2a, we obtain the valence-band structures of the shear strained wurzite GaN system from first-principles calculations. The energy separation between E_2 and E_3 is defined as $\Delta E_{23} = \sqrt{\Delta_{cr}^2 + 8D_6^2\varepsilon_{xz}^2}$. The energy of one of the doubly degenerate valence-bands (E_1, with p_y character) stays constant while the other one (E_2, with p_x character) goes up. Correspondingly, the crystal-field split-off band (E_3, with p_z character) goes down with the same magnitude. The changes of these band energies agree well with those predicted by the $\mathbf{k}\cdot\mathbf{p}$ perturbation approach. The crystal-field splitting Δ_{cr} is obtained from the

energy splitting between HH/LH and CH bands in the unstrained nitride system. Then we fit the energy separation (ΔE_{23}) to the expression above to obtain the deformation potential D_6, as shown in Fig. 2.2b.

Above we have obtained the definitions of all deformation potentials that are needed to describe the modification of band structure with strain at the Γ point. In order to determine these deformation potentials from first-principles calculations, we apply different strain components in the wurtzite nitride systems and then fully relax the structure including the internal structural parameter u (which sensitively affects the magnitude of crystal-field splitting). By fitting the analytical expressions for the $\mathbf{k}\cdot\mathbf{p}$ eigenenergies at the Γ point to the calculated band structures with different strain components, the deformation potentials are obtained.

The first-principles calculations are carried out using the plane-wave projector augmented-wave (PAW)[89] and hybrid functional method as implemented in the VASP code[90]. We use the Heyd-Scuseria-Ernzerhof (HSE)[32,84] DFT hybrid functional to carry out the structure optimization, which gives band gaps and equilibrium lattice parameters in better agreement with experiment for nitrides than LDA and GGA, as shown in Table 1.1. The screening parameter μ in HSE is fixed at a value of 0.2 and the mixing parameter α is fixed at a value of 25% (HSE06). We also performed LDA, GGA-PBE[24], and quasiparticle G_0W_0 calculations based on exact exchange (OEPx)[85] to crosscheck the strain effects on the

band structures. We treat the semi-core d-electrons of Ga and In as valence electrons in our calculations. We use a plane-wave energy cutoff of 600 eV, which is necessary for the accurate determination of the internal displacement parameter u, and a $6\times6\times4$ Γ-point centered k-point mesh.

2.3 Computational results

2.3.1 Lattice parameters, band gaps, and band structures

Table 1.1 demonstrates that LDA underestimates the equilibrium lattice parameters of AlN, GaN, and InN, while GGA overestimates these parameters compared with experimental data. HSE gives the best agreement with the experimental values. As shown in Table 1.1, band gaps are underestimated severely in LDA and GGA, which for InN even results in a negative gap (metallic state). HSE gives a considerable improvement and produces gaps that are close to those obtained from G_0W_0@OEPx[29] and only slightly underestimate the experimental values. These results confirm the reliability of the HSE method to study strain effects in wurtzite nitride systems.

The HSE data shown in Table 1.1 are obtained with the mixing parameters α = 25%. By modifying this mixing parameter, we can reproduce the experimental band gaps. The mixing parameters needed to reproduce the experimental band gaps of group-III nitrides are: 32% for AlN, 28% for GaN, and 24% for

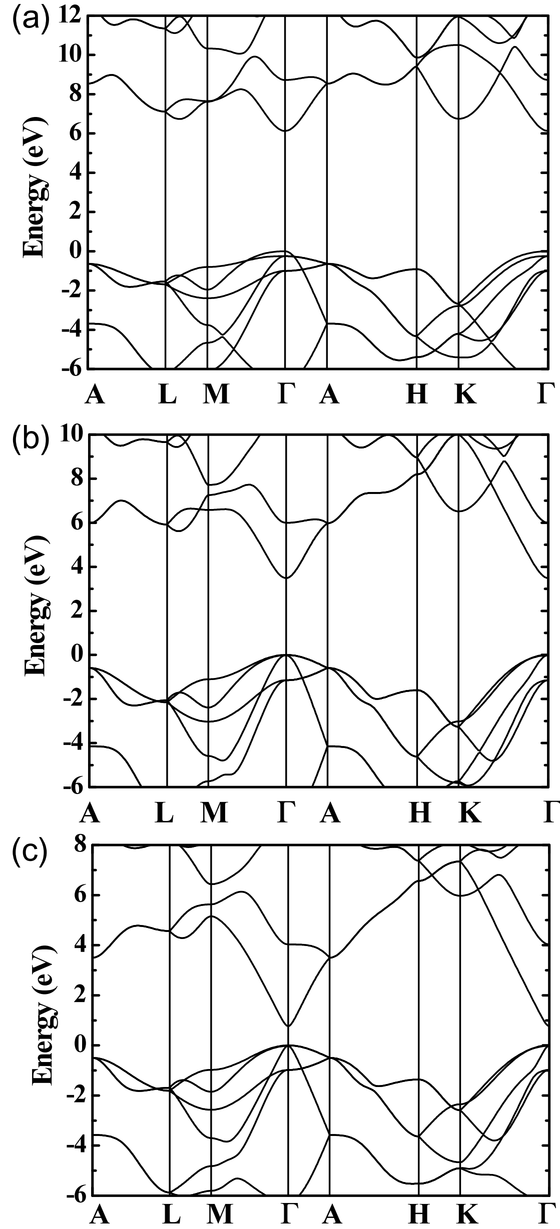

Figure 2.3: Band structures of (a) AlN, (b) GaN, and (c) InN obtained from density functional calculations using the HSE hybrid functional, with mixing parameters α adjusted to reproduce the experimental band gap (see text).

InN. The band structures of group-III nitride semiconductors AlN, GaN, and InN obtained with the hybrid functional approach with modified mixing parameters are shown in Fig. 2.3. These band structures show very good agreement with results obtained with the G_0W_0@OEPx method[29]. We thus validate the use of HSE as a reliable and accurate band-structure method. Clearly, only the transitions from the first conduction band to the topmost three valence bands are relevant for optical emission processes in nitride-based LED devices. In the following we will focus our discussions on transition energies and detailed valence-band structures of these four bands.

2.3.2 Transition energies under strain

In this Section, we calculate the dependence of the transition energies of the c-plane GaN on strain by computing the band structures of GaN systems for two types of realistic strain conditions: biaxial stress and hydrostatic pressure. Wurtzite c-plane GaN thin films grown on sapphire or SiC always experience biaxial stress induced by the substrate. Under such stress, when the wurtzite system experiences a compressive biaxial strain in the c plane, it is always accompanied by a tensile out-of-plane uniaxial strain:

$$\varepsilon_{zz} = -\frac{C_{13}}{C_{33}}\varepsilon_{xx}, \quad \varepsilon_{xx} = \varepsilon_{yy} \neq 0. \tag{2.9}$$

Here we use the elastic constants obtained by former theoretical calculations[91]

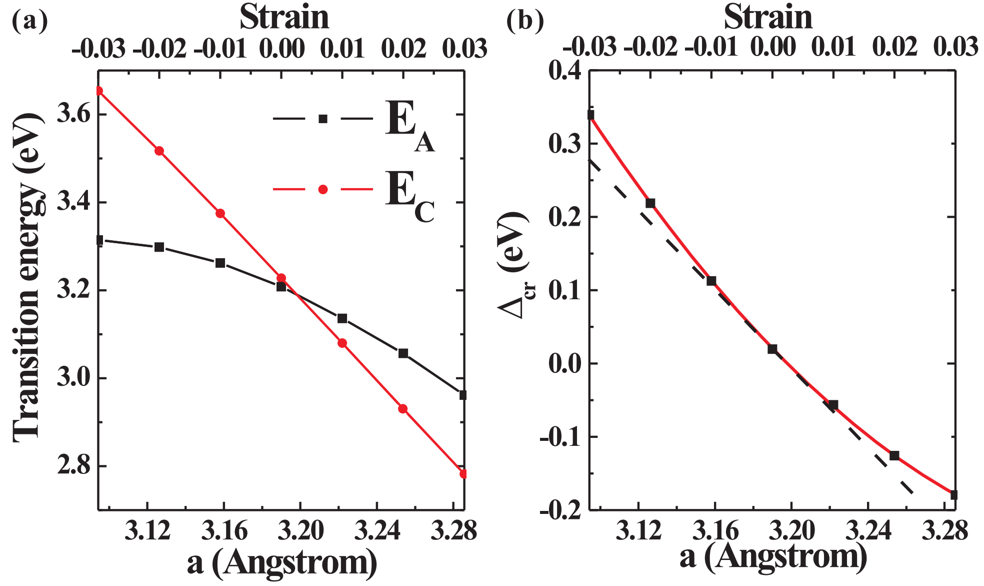

Figure 2.4: (a) Transition energies E_A and E_C of GaN under biaxial stress. (b) Crystal-field splitting of GaN under biaxial stress. Data points correspond to calculated values, solid lines represent second-order polynomial fits. The dashed line is a linear fit around the equilibrium lattice parameter.

to determine the lattice constant c. Figure 2.4a shows the transition energy between the first conduction band and the topmost three valence bands (HH, LH and CH) of GaN under biaxial stress in the c plane for the strain range $\pm3\%$. Interestingly the transition energy between CB and HH/LH shows a strong nonlinear behavior. Such nonlinearity is also evident in the crystal-field splitting (Δ_{cr}) in Fig. 2.4b, which can be described by a quadratic dependence as demonstrated by the fitted curve. This implies that the slope (which defines the deformation potentials) differs for different lattice parameters. Similar nonlinearities are observed for AlN and InN under biaxial stress (not shown here). For systems with large biaxial strain components, such as InGaN alloys with high In composition grown

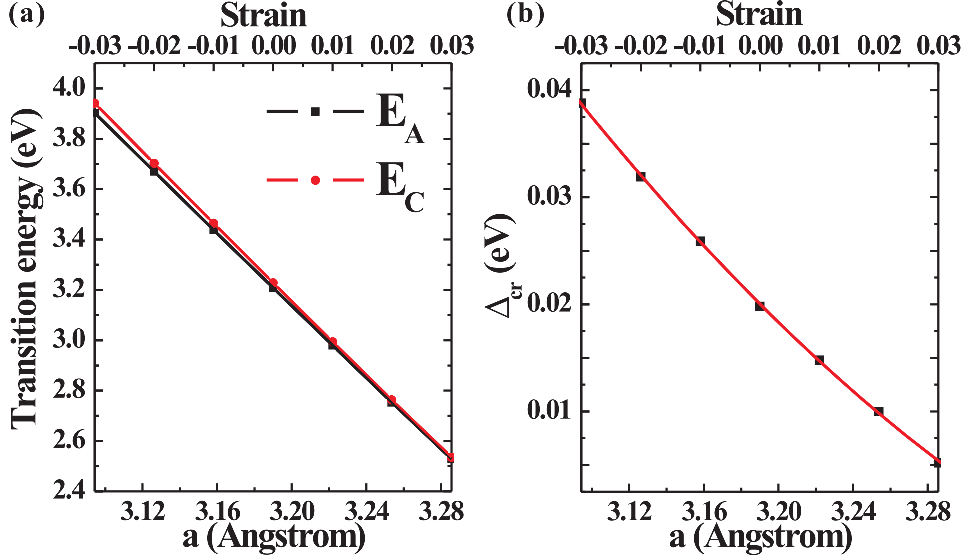

Figure 2.5: (a) Transition energies E_A and E_C of GaN under hydrostatic pressure. (b) Crystal-field splitting of GaN under hydrostatic pressure. Data points correspond to calculated values, solid lines represent second-order polynomial fits. The dashed line is a linear fit around the equilibrium lattice parameter.

on GaN substrates, these nonlinearities may have to be taken into account.

Another realistic strain condition is induced by hydrostatic pressure, where the stress components along three directions now have the same, $\sigma_{xx} = \sigma_{yy} = \sigma_{zz}$. The in-plane strain and out-of-plane strain now have the same sign but the strain components are not isotropic:

$$\begin{aligned} \varepsilon_{zz} &= \frac{C_{11} + C_{12} - 2C_{13}}{C_{33} - C_{13}} \varepsilon_{xx}, \\ \varepsilon_{xx} = \varepsilon_{yy} &= \frac{C_{33} - C_{13}}{C_{33}(C_{11} + C_{12}) - 2C_{13}^2} \sigma_{zz}. \end{aligned} \tag{2.10}$$

Under hydrostatic pressure condition, as shown in Fig. 2.5a, the transition energies change almost linearly in the strain range ±3% as does the crystal-field splitting as shown in Fig. 2.5b. As a result, as shown in Fig. 2.6a, under biaxial

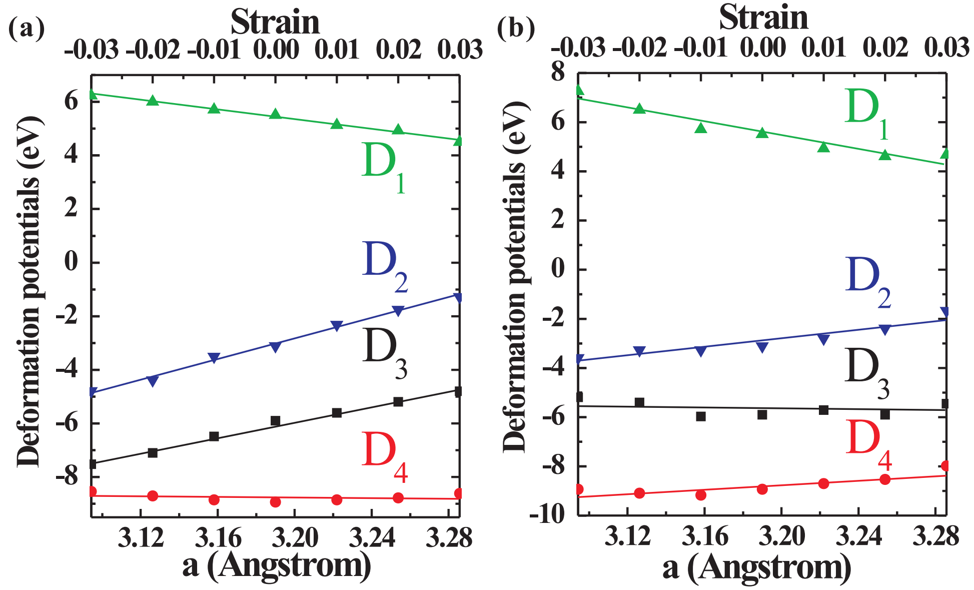

Figure 2.6: (a) Deformation potentials of GaN under biaxial stress. (b) Deformation potentials of GaN under hydrostatic pressure.

stress D_3 and D_4 vary by more than 50% in the biaxial strain range ±3%. Such large changes of deformation potentials also occur for the case of hydrostatic pressure as shown in Fig. 2.6b, although the transition energies that result from energy differences between different bands are close to linear in strain. This can be explained by the fact that the decrease of D_3 and the increase of D_4 largely cancel, thus greatly reducing the nonlinearity.

2.3.3 Deformation potentials of group-III nitrides

We have seen that the dependence of band energies on strain in general is nonlinear. However, over a small range of strains around a given lattice parameter, the variation can be regarded as linear. It is therefore still possible to define a

single set of deformation potentials, choosing the experimental lattice parameters as the point of reference. Our results are listed in Table 2.1, and compared with previous results both from experiment and from theory. In our experience a lack of relaxation of the internal parameter u (due to a lack of convergence) leads to an underestimate of the change in the crystal-field splitting under strain and hence an underestimate of the magnitude of corresponding deformation potentials D_3 and D_4. We suspect that this was the case in Ref. 74. As shown in Table 2.1, the experimental data for deformation potentials of GaN is also scattered over a very large range.

By constraining the strain range to realistic strain conditions in the linear regime around the experimental lattice parameters, we derive a consistent and complete set of deformation potentials for all three nitrides from HSE calculations with the mixing parameter $\alpha = 25\%$. The resulting values are listed in Table 2.2. For the purpose of comparison between different exchange-correlation functionals we also list our LDA and GGA-PBE results in Table 2.2 for AlN and GaN systems; we note that LDA and GGA results for InN are not available due to negative band-gap problem. With the exception of $a_{cz} - D_1$ the deformation potentials decrease in absolute value from AlN to GaN and InN.

Table 2.2 shows that the deformation potential data are sensitive to the exchange correlation functional. LDA and GGA-PBE data agree very well with each other, while both of them show appreciable deviations from HSE results.

The band-gap-related deformation potentials $a_{cz} - D_1$ and $a_{ct} - D_2$ obtained by HSE calculations are considerably larger in magnitude than those from LDA and GGA-PBE results. We expect that the HSE calculations, which yield better band structures, also provide a better description of the change of band gaps under strain. The valence-band-related deformation potentials D_3, D_4, D_5, and D_6 are clearly less sensitive to the choice of exchange-correlation functional.

We checked the validity of the HSE hybrid functional results by performing quasi-particle G_0W_0 calculations based on exact-exchange (OEPx), as described in Sec. 1.4. The comparison (included in Table 2.2) shows that the deformation potentials of GaN obtained from HSE calculations are in good agreement with those obtained from G_0W_0 calculations. Among these deformation potentials, $a_{cz} - D_1$ and $a_{ct} - D_2$ are more sensitive to the gap and hence the most important test. The good agreement with G_0W_0 data for these two deformation potentials validates the reliability of HSE method in determining deformation potentials of nitride systems. Although both HSE and G_0W_0 calculations properly address the band-gap problem, here we recommend HSE data for further use. Indeed, as demonstrated above, the HSE calculations provide highly accurate results for structural properties, which are required to subsequently obtain the band structures from which deformation potentials are extracted. Table 2.2 also lists the range of experimental data for deformation potentials of GaN (see Table 2.1); we note that our HSE results all fall within this (very wide) range. As shown in

Table 2.1, our HSE results agree well with recent experimental data measured by stress experiments[73].

In Table 2.2 we also list the deformation potentials suggested by Vurgaftman and Meyer[30]. For GaN our HSE values give systematically smaller absolute values than the Vurgaftman and Meyer numbers, with the exception of $a_{cz} - D_1$. For AlN HSE gives larger $|a_{cz} - D_1|$ value. For InN, Vurgaftman and Meyer recommended to use the same deformation potentials as for GaN due to the lack of data. Our HSE values show that the deformation potentials of InN are much smaller than those of GaN, with differences in magnitude as large as several eV; use of the GaN values therefore lead to significant errors.

2.4 Strain effects in InGaN alloys

With the complete set of deformation potentials for AlN, GaN, and InN, we can now study the strain effects on the band structure of an $In_xGa_{1-x}N$ alloy. $In_xGa_{1-x}N$ layers grown on a c-plane GaN substrate may exhibit strong spontaneous fields that induce electron-hole separation. In recent years, growth in nonpolar and semipolar orientations has been proposed to improve the device efficiency. Due to the lattice mismatch between nitride alloys and substrates, strain is present and plays a crucial role in band structure and device performance. Strain affects the band gap in all cases; in addition, for c-plane-grown devices strain causes piezoelectric polarization, while in nonpolar and semipolar $In_xGa_{1-x}N$ de-

Table 2.2: Deformation potentials (eV) of wurtzite AlN, GaN and InN obtained from LDA, GGA, HSE, and G_0W_0 methods. For GaN the range of experimentally determined deformation potentials and the values recommended by Vurgaftman and Meyer (VM) (Ref. 30) are also shown.

	Method	$a_{cz} - D_1$	$a_{ct} - D_2$	D_3	D_4	D_5	D_6
AlN	LDA	-3.44	-11.39	8.97	-3.95	-3.36	-
	GGA	-3.39	-11.38	9.12	-4.01	-3.37	-
	HSE	-4.21	-12.07	9.22	-3.74	-3.30	-4.49
GaN	LDA	-4.56	-8.03	5.61	-3.03	-2.94	-
	GGA	-4.46	-8.08	5.83	-2.98	-3.13	-
	HSE	-6.02	-8.98	5.45	-2.97	-2.87	-3.95
	G_0W_0@OEPx	-5.49	-8.84	5.80	-3.10	-	-
	VM	-4.90	-11.30	8.20	-4.10	-4.60	-
	Exp. range	-9.6 ... -3.1	-11.8 ... -8.1	1.4 ... 8.2	-4.1 ... -0.7	-4.7 ... -2.4	-
InN	HSE	-3.64	-4.58	2.68	-1.78	-2.07	-3.02

vices strain plays a crucial role in the polarization character of emitted light. In this Section we will explore the strain effects in these three types of $In_xGa_{1-x}N$ alloy in detail.

2.4.1 Band gap and bowing parameter of *c*-plane InGaN alloys

The $In_xGa_{1-x}N$ alloy is an ideal system for optoelectronic applications as LDs and LEDs in the visible range of spectrum. The incorporation of In lowers the band gaps of the $In_xGa_{1-x}N$ alloys and the emission wavelength in $In_xGa_{1-x}N$ devices is determined by the amount of indium, and can cover a wide spectral range from red to blue. $In_xGa_{1-x}N$ epilayers grown on GaN substrate are pseudomorphically strained and values of band gap are deduced from the experimental data for strained films. Besides the strain effect, the band-gap variation of an InGaN alloy grown on a *c*-plane GaN substrate is also affected by the bowing effect. The band gap of a free-standing $In_xGa_{1-x}N$ alloy shows a deviation (bowing effect) from linear interpolation of the fundamental gaps of GaN and InN, with a wide range of bowing parameters in the literature[59,60,61,92,93,94]. Interestingly, the bowing parameter is found to be In composition dependent[92,93,95]. Here we aim to obtain a more accurate value for the bowing parameter by using our calculated deformation potentials to determined the effects of strain on the gap, which need to be subtracted from experimental band-gap data before the effect of bowing can

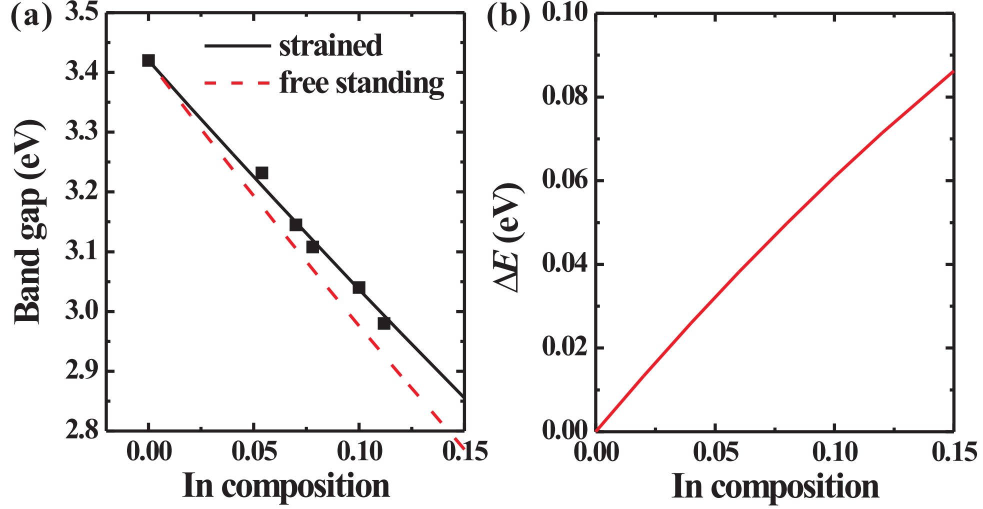

Figure 2.7: (a) Calculated band gap of a *c*-plane $In_xGa_{1-x}N$ with (solid line) and without (dashed line) strain effect. The bowing parameter is set to 2.0 eV and experimental data are shown as black dots. (b) Band-gap change due to strain effects in an $In_xGa_{1-x}N$ alloy.

be identified.

The equilibrium lattice constants of the $In_xGa_{1-x}N$ alloy are obtained by linear interpolation between GaN and InN: $a_{InGaN} = a_{InN} \times x + a_{GaN} \times (1-x)$ (Ref. 95). Similarly, the elastic constants and deformation potentials of alloy systems can be determined from pure nitrides by linear interpolation which are dependent on In composition as well: $C_{InGaN} = C_{InN} \times x + C_{GaN} \times (1-x)$ and $D_{InGaN} = D_{InN} \times x + D_{GaN} \times (1-x)$. The band gap of a free-standing alloy is calculated using the equation: $E_g = E_{InN} \times x + E_{GaN} \times (1-x) + b \times x(1-x)$ with bowing parameter b.

Assuming that the $In_xGa_{1-x}N$ epilayer is pseudomorphically strained by the GaN substrate, the in-*c*-plane biaxial strain components are determined by the

lattice mismatch between alloy and substrate $\varepsilon_{xx} = \varepsilon_{yy} = (a_{GaN} - a_{InGaN})/a_{InGaN}$. The corresponding out-of-plane strain component is related to the in-plane strain by a combination of elastic constants of the alloy $\varepsilon_{zz} = -\frac{2C_{13}}{2C_{33}}\varepsilon_{xx}$. In the following strain calculations we use the elastic constants by Wright *et al.*[91]. From Eq. 2.2, we calculate the strain effects on the band gap of calculated InGaN alloy as a function of In compositon. In previous work[59,92,93] the strain effect on band gap was assumed to be a linear function of In fraction x. However, as shown in Fig. 2.7, such a linear relation does not hold true, mainly because the deformation potentials of the InGaN alloy also exhibit a dependence on In composition. Since the difference in deformation potentials between GaN and InN is quite large, the changes in band positions which are a product of deformation potentials and strain may exhibit distinct nonlinearities.

Considering both the strain effect and the bowing effect, we now derive the bowing parameter of unstrained $In_xGa_{1-x}N$ alloys by fitting the experimental data of band gaps measured by McCluskey *et al.*[59,92]. From our calculations, the three transition energies of the c-plane InGaN system decrease with increasing In composition. The energy separation between HH/LH bands (with transition energies E_A and E_B) and the CH band (with transition energies E_C) increases with increasing In composition. The band gap of a $In_xGa_{1-x}N$ alloy as a function of In composition is shown in Fig. 2.7a. The band gap of a free-standing (unstrained) $In_xGa_{1-x}N$ alloy is also shown in Fig. 2.7a for comparison. The band-gap change

induced by strain is shown in Fig. 2.7b. Obviously, the strain effect is not linear with In composition as assumed before[59,92]. By fitting our calculated band gap (solid curve) to the experimental data (solid dots in Fig. 2.7a), a bowing parameter of 2.0 eV is derived for $In_xGa_{1-x}N$ alloy within the composition range $0 < x < 0.1$. This value is smaller than the result derived by McCluskey *et al.* (2.6 eV), though it agrees very well with the result obtained by recent first-principles hybrid functional calculations[95].

2.4.2 Strain effects on the polarization character of non-polar m-plane InGaN

In recent years, nonpolar InGaN/GaN quantum wells(QWs) have been proposed and fabricated as promising candidates for high-efficiency light emitters[96,97,98] because the polarization in these devices is expected to be greatly reduced or even negligible. Interestingly, the light emitted from nonpolar InGaN/GaN QWs has been found to be polarized[58,99,100,101,102]. The emitted light has preferential polarization along the $[11\overline{2}0]$ (x) direction, while the weaker transition has polarization along the [0001] (z) direction. Defining the polarization ratio as $\rho = (I_x - I_z)/(I_x + I_z)$, Masui *et al.* further found that the polarization ratio increases with increasing In composition, and correspondingly the energy separation between the valence bands with x character and z character increases[58]. Here we explore how strain affects the band ordering and polarization characteristics

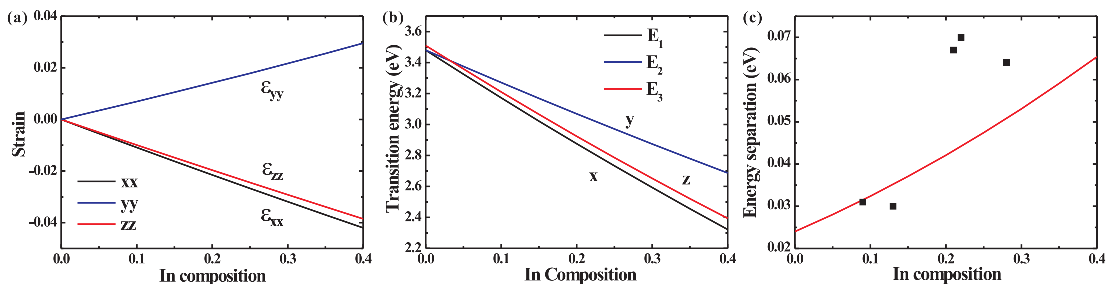

Figure 2.8: (a) Strain components in m-plane $In_xGa_{1-x}N$ alloys. (b) Transition energies of m-plane $In_xGa_{1-x}N$ alloys. (c) Energy separation between the topmost two valence bands, experimental data are shown as black dots.

of the optical transition for m-plane $In_xGa_{1-x}N$ alloys.

For $In_xGa_{1-x}N$ alloys grown on m-plane GaN substrates, the two principal directions in the m plane are $[11\bar{2}0]$ (x) and $[0001]$ (z), while the direction normal to the m plane is $[1\bar{1}00]$ (y). The in-m-plane strain components are determined by the lattice mismatch between the InGaN alloy and the GaN substrate, while the out-of-plane strain component (along the y direction) is determined by the relation: $\epsilon_{yy} = -C_{11}/C_{33}\epsilon_{xx} - C_{12}/C_{33}\epsilon_{zz}$. Assuming that the InGaN film is perfectly strained by the GaN substrate without strain relaxation, the strain components in the alloy are calculated from the lattice mismatch and elastic constants, as shown in Fig. 2.8a. The strain component along the x direction ϵ_{xx} is compressive while that along the y direction ϵ_{yy} is tensile. It means that ϵ_{xx} differs from ϵ_{yy} in the nonpolar $In_xGa_{1-x}N$ system. We will show that this difference is crucial for the modification of band structures of m-plane $In_xGa_{1-x}N$ alloys by splitting HH and LH bands.

With our deformation potentials and the expressions for band energies in Eq. 2.4, we calculate the transition energies of an $In_xGa_{1-x}N$ alloy as a function of In composition, as shown in Fig. 2.8b. The difference between ϵ_{xx} and ϵ_{yy} lowers the symmetry of the wurtzite system from C_{6v} to C_{2v} and splits the HH and CH bands (denoted now as E_1 and E_2 bands respectively, since the strain perturbation breaks the original two $|X \pm iY\rangle$ states into p_x-like and p_y-like states). By solving the strained $\mathbf{k}\cdot\mathbf{p}$ Hamiltonian, we find that the eigenstate of the E_1 band has p_x character and that of the E_2 band has p_z character. Furthermore, at a very low In composition (x=0.04) the valence band E_2 crosses the CH band which is p_z-like and denoted as the E_3 band. This means that in m-plane $In_xGa_{1-x}N$ alloys the band ordering near the valence-band edge is E_1, E_3, and E_2 in order of decreasing electron energy. The dominant optical transition is therefore from the CBM to the E_1 band and the emitted light from this transition has polarization mainly along the x direction. The next possible but much weaker transition is from the CBM to the E_3 band which has polarization along the z direction. The prediction of such band ordering and polarization character of emitted light is consistent with recent experimental observations[58,101,102].

As shown in Fig. 2.8c (red line), the energy separation between valence bands E_1 and E_3 increases constantly with increasing In composition. This implies that the hole concentration of the lower band decreases relative to the higher one and the polarization ratio decreases. This prediction agrees very well with

experimental observations[58]. The data points in Fig. 2.8c are from experimental measurement by Masui *et al.* Our prediction agrees well with the experimental data at low In composition, but a sudden jump in experimental data occurs at an In composition around 0.2, which cannot be explained assuming the alloy is perfect and fully strained by the substrate. The discrepancies are possibly due to In segregation or to strain relaxation in the nonpolar $In_xGa_{1-x}N$ alloy with high In fraction.

2.4.3 The role of strain in the polarization switching of $(11\bar{2}2)$ InGaN alloys

Semipolar or nonpolar quantum-well orientations have been proposed to increase the efficiency of light emitters. In these orientations the effect of spontaneous and piezoelectric polarization fields is reduced and thereby the carrier overlap is increased[96,97,98]. Optical anisotropy becomes relevant when device structures are fabricated on nonpolar and semipolar oriented substrates, which raises the problem how to control the light polarization emitted from group-III nitrides and their alloys. Growth of InGaN on GaN along semipolar or nonpolar directions leads to strain conditions different from those in conventional growth along the c direction. This affects the splitting of the uppermost valence bands and hence the polarization of the emitted light. Such effects in the case of nonpolar growth were discussed in Sec. 2.4.2. Optical anisotropy has also been observed

for semipolar[66,86,87,103,104,105] devices. This raises the question of how to *control* the polarization of the emitted light, which is not only of scientific interest but also of technical importance for the performance of light-emitting diodes and laser diodes.

Polarization switching has been reported for semipolar InGaN grown on a $(11\bar{2}2)$ GaN substrate[66,87]. The dominant polarization direction was found to switch from $[1\bar{1}00]$ (perpendicular to the c-axis) to $[\bar{1}\bar{1}23]$ when the In concentration was increased above 30%, but the mechanism responsible for the change in polarization can not be identified. Other experimental studies have found no evidence of polarization switching, however. Under high excitation power density the sign of the polarization ratio was found to remain unchanged even at high In content[104,105]. Why the polarization ratio is affected by the excitation power density also remains unclear.

Three factors critically influence the band structure of InGaN quantum wells (QW) and therefore the polarization of the emitted light: indium concentration, strain, and quantum confinement. Based on $\mathbf{k}\cdot\mathbf{p}$ modeling Yamaguchi predicted that the QW thickness strongly affects the polarization[63]. This seems qualitatively consistent with the results of Masui *et al.*, who observed an enhancement in optical polarization for thinner quantum wells[87]. However, in Yamaguchi's work the magnitude of this quantum confinement effect is very sensitive to the choice of Luttinger parameters[29] and can range from 2 to 20 meV for 2nm thick quantum

wells. Ueda *et al.*, on the other hand, found no appreciable QW thickness effect[66]. They proposed strain to be the dominant factor, and derived a large shear-strain deformation potential of D_6=-8.8 eV from their measurements[66].

Strain in $(11\overline{2}2)$ semipolar InGaN grown on GaN substrates is characterized by the shear strain and anisotropic strain in the c plane. To evaluate these effects we use the deformation potentials D_1 to D_6, the determination of which was discussed in Sec. 2.3. With these deformation potentials and the band parameters of Ref. 29 we use the $\mathbf{k{\cdot}p}$ approach to determine the energies of the topmost three valence bands at the Γ point.

The energies of the topmost three valence bands at the Γ point (E_1 to E_3) can be obtained by the k.p theory by diagonalizing a strained 6×6 Hamiltonian of wurtzite symmetry, as shown in Sec. 2.1. Including strain components along the three directions in the normal coordinate system ε_{xx}, ε_{yy}, and ε_{zz} and shear strain

(only ε_{xz} for simplicity) gives

$$
\begin{aligned}
E_1 &= \Delta + (D_1 + D_3)\varepsilon_{zz} + (D_2 + D_4)(\varepsilon_{xx} + \varepsilon_{yy}) \\
&\quad -D_5(\varepsilon_{xx} - \varepsilon_{yy}), \\
E_2 &= \tfrac{1}{2}\Delta + D_1\varepsilon_{zz} + D_2(\varepsilon_{xx} + \varepsilon_{yy}) \\
&\quad +\tfrac{1}{2}\left[D_3\varepsilon_{zz} + D_4(\varepsilon_{xx} + \varepsilon_{yy}) + D_5(\varepsilon_{xx} - \varepsilon_{yy})\right] + \tfrac{1}{2}\delta, \\
E_3 &= \tfrac{1}{2}\Delta + D_1\varepsilon_{zz} + D_2(\varepsilon_{xx} + \varepsilon_{yy}) \\
&\quad +\tfrac{1}{2}\left[D_3\varepsilon_{zz} + D_4(\varepsilon_{xx} + \varepsilon_{yy}) + D_5(\varepsilon_{xx} - \varepsilon_{yy})\right] - \tfrac{1}{2}\delta, \\
\delta &= \sqrt{\left[\Delta + D_3\varepsilon_{zz} + D_4(\varepsilon_{xx} + \varepsilon_{yy}) + D_5(\varepsilon_{xx} - \varepsilon_{yy})\right]^2 + 8D_6^2\varepsilon_{xz}^2},
\end{aligned}
\tag{2.11}
$$

where Δ_{cr} is the crystal-field splitting and the spin-orbit splitting has been omitted. Note that the present expressions are different from those in Sec. 2.2, due to the inclusion of both the uniaxial strain and the shear strain. The eigenstate pertaining to E_1 has p_y character, and the other two have mixed p_x and p_z character[51]. The energy separation between the topmost two bands at the Γ point in strained $In_xGa_{1-x}N$ layers is:

$$
\Delta E_{12} = \frac{1}{2}[\Delta + D_3\varepsilon_{zz} + D_4(\varepsilon_{xx} + \varepsilon_{yy})] - \frac{3}{2}D_5(\varepsilon_{xx} - \varepsilon_{yy}) - \frac{1}{2}\delta. \tag{2.12}
$$

As can be seen from Eq. 2.12, anisotropic strain (D_5) and shear strain (D_6) have opposite effects because D_5 is negative[80]. A switch in the band ordering may occur if the shear strain and/or the deformation potential D_6 are large enough.

Before we can investigate the effect of strain on the band structure the strain conditions in the alloy have to be determined. The lattice parameters follow from

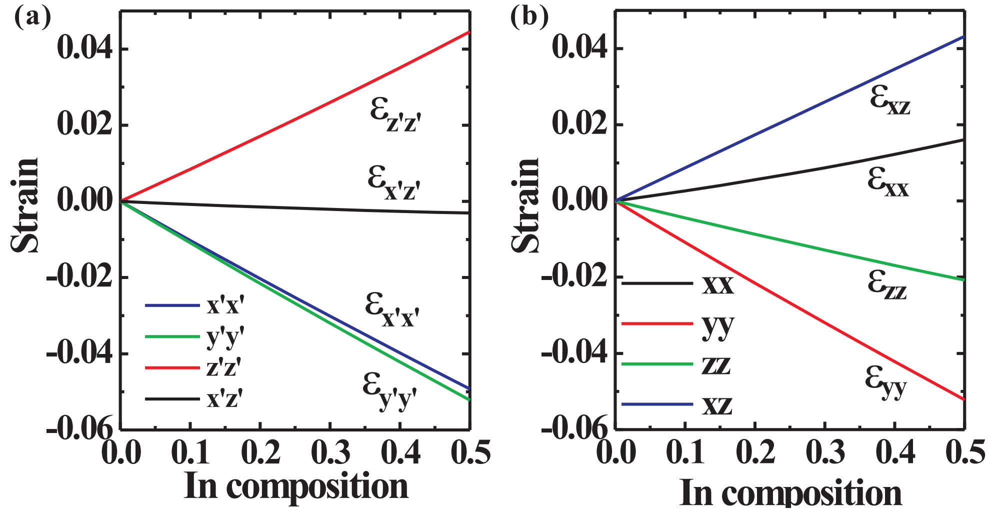

Figure 2.9: Strain components of the $(11\bar{2}2)$ InGaN grown on a GaN substrate in (a) primed coordinate system related to the layer surface normal and (b) natural coordinate system associated with the c axis. For more details of the definition of primed and natural coordinate systems, we refer to Ref. 20.

Vegard's law: $a_{\mathrm{InGaN}} = a_{\mathrm{InN}} \times x + a_{\mathrm{GaN}} \times (1-x)$. The lattice mismatch to the GaN substrate induces composition-dependent compressive in-plane strain. If the InGaN layer thickness is below the critical value for misfit-dislocation formation, the lattice mismatch is accommodated by straining the layer elastically. The strain components in and out of the c plane, which are needed for the $\mathbf{k}\cdot\mathbf{p}$ approach, can be determined from the lattice mismatch in the semipolar plane[20]. Using the elastic constants of Wright[91] we obtain the strain components for $(11\bar{2}2)$ semipolar quantum wells in terms of the normal c-plane coordinate system as shown in Fig. 2.9. We observe that these pseudomorphic strain conditions lead to anisotropic strain in the c-plane ($\varepsilon_{xx} - \varepsilon_{yy} \neq 0$), and a large shear-strain component ε_{xz}.

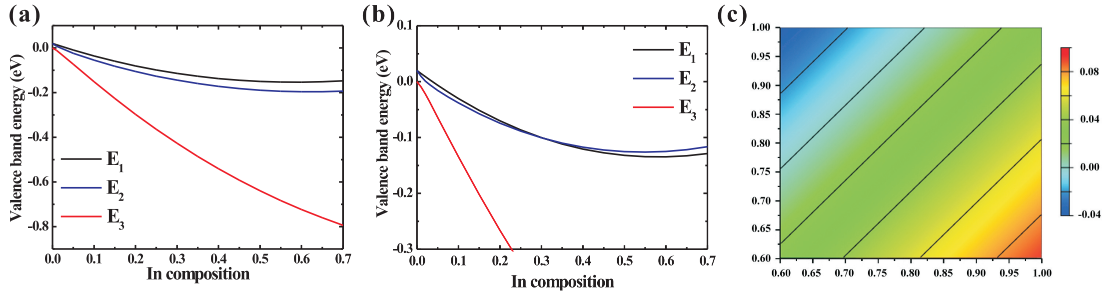

Figure 2.10: (a) Transition energies of $(11\bar{2}2)$ semipolar $In_xGa_{1-x}N$ alloy system assuming that the epilayer is fully strained by lattice mismatch. (b) Transition energies of semipolar $In_xGa_{1-x}N$ alloy system assuming that the strain in the epilayer is partially relaxed by 20% along the $[1\bar{1}00]$ direction. (c) Contour plot of the energy difference between the topmost two valence bands at In composition x=0.3.

To evaluate Eq. (2.12) for a given indium composition we linearly interpolate the deformation potentials of GaN and InN. In Fig. 2.10a we show the transition energies between the three valence bands and the conduction band, assuming that the $(11\bar{2}2)$ InGaN layer is pseudomorphically grown on a GaN substrate. Under these conditions, the two highest valence bands do not cross over and the band ordering does not switch with increasing In concentration. The value of ΔE_{12} and the In concentration at which polarization switching occurs also depend on the degree of quantum confinement and on the spin-orbit splitting. Since the spin-orbit splitting in GaN is only 8 meV[106], we expect it does not change our qualitative results. Effects of quantum confinement are also not included here. In separate work, in collaboration with C. Roberts, we calculated these quantum-confinement effects explicity and found them to lead to very small differences compared to bulk calculations, thus not impacting any of our conclusions[107].

Due to the large lattice mismatch between InN and GaN (11%), strains in alloys with high In content will be large and may be partially relaxed by forming structural defects (such as dislocations and stacking faults). According to Fig. 2.9, the magnitude of the strain component along the y direction is larger than along the x and z directions. It is thus conceivable that the strain component in the y direction may be partially relaxed in an InGaN layer grown on GaN. In Fig. 2.10c we plot ΔE_{12} for an $In_{0.3}Ga_{0.7}N$ alloy as a function of the strain components along the $[1\bar{1}00]$ (y) and $[\bar{1}\bar{1}23]$ (projection of c-axis on $(11\bar{2}2)$ plane) directions, expressed relative to their coherent value obtained from the lattice mismatch $[\epsilon_0 = (a_{\mathrm{substrate}} - a_{\mathrm{alloy}})/a_{\mathrm{alloy}}]$. We find that ΔE_{12} becomes negative if the strain relaxation along $[1\bar{1}00]$ is larger than that along $[\bar{1}\bar{1}23]$ [Fig. 2.10b]. We conclude that partial strain relaxation may play a role in polarization switching of semipolar InGaN grown on GaN substrates.

Partial strain relaxation has indeed been observed in semipolar InGaN samples[108]: The strain component along $[\bar{1}\bar{1}23]$ was found to experience a higher degree of relaxation through the formation of dislocations facilitated by the existence of glide planes (the c plane) and the presence of shear strain. This relaxation pattern differs from the one that we predict to promote polarization switching [Fig. 2.10]. However, the process of relaxations through dislocations may cause an inhomogeneous strain distribution in the InGaN layer, especially at high In concentrations. The in-c-plane and shear strain variation induces fluctuations of

the valence-subband separation as a function of position. In some areas, the shear strain might be large enough in comparison to the in-c-plane strain to push up the band with $|x'\rangle$ character and hence change the ordering of the topmost two subbands. In these areas, the $|x'\rangle$ band is higher in energy and occupied by holes at low excitation power, leading to a change in the dominant polarization. At very high excitation powers, the area over which the reordering occurs is insufficient to invert the hole population in the two subbands, and the emission polarization will not change, thus explaining the observations of Ref. 104. More theoretical and experimental work is called for to investigate the inhomogeneities of In concentrations and strain distributions in $(11\bar{2}2)$ InGaN/GaN QWs, and to establish their relation to the polarization switching phenomenon.

2.5 Conclusion

In this Chapter we have studied the strain effects on the band structure of wurtzite AlN, GaN, and InN using a first-principles approach based on hybrid functional and quasiparticle G_0W_0 methods. We observe nonlinearities in the strain dependence that should be taken into account in highly strained nitride materials and alloys. For the linear regime around the experimental lattice parameters, we present a complete and consistent set of deformation potentials for the three nitride materials. Together with the Luttinger band parameters, the deformation potentials constitute essential input for device modeling and allows

to predict the band positions under realistic strain conditions. By using this set of deformation potentials, we have predicted the transition energies of InGaN alloys grown on polar, semipolar, and nonpolar GaN substrates. We obtain an accurate value for the InGaN bowing parameter by calculating the strain effect on the band gap and fitting to experimental data. We predict a change in valence-band ordering for a strained InGaN alloy grown on m-plane GaN, which agrees with experimental observations. We also calculate the change in band structures for a semipolar $(11\overline{2}2)$ InGaN alloy grown on a GaN substrate but do not observe the change in band ordering reported in some experiments. We propose that the partial relaxation of strain and inhomogeneous strain distribution may play a role in the observed polarization switching phenomenon.

Chapter 3

The role of defects in absorption and luminescence in GaN and AlN

Point defects and impurity atoms strongly affect the electronic properties of nitride materials and the performance of nitride-based optoelectronic devices. First, the intentional addition of donor and acceptor atoms to semiconductors yields n- and p-type doped materials, respectively, which are prerequisites for the fabrication of light emitting diodes. Second, defects and impurities are responsible for carrier compensation. The free-carrier density achieved by doping may be limited by compensating defects that spontaneously form at high doping concentrations. In addition, defects mediate non-radiative recombination and cause loss

in optoelectronic devices and possibly device degradation in laser devices. These examples highlight the need to study defects in nitride materials and understand their effect on device performance. In this chapter, we will focus on providing the optical signatures of several relevant native defects and defect complexes in GaN and AlN.

3.1 The role of the nitrogen vacancy in luminescence in Mg-doped GaN

3.1.1 Nitrogen vacancies and complexes in GaN

As GaN-based semiconductor devices are pushed to higher efficiencies, it becomes imperative to minimize the impact of defects that are detrimental to the device performance. In particular, it is crucial to understand the behavior and grasp control of defects that limit *p*-type doping by acting as recombination centers in Mg-doped GaN. It has been suggested that native defects such as nitrogen vacancies play an important role as compensating centers in *p*-type GaN[21,109]. Recent experiments based on positron annihilation spectroscopy (PAS) indicate the presence of nitrogen vacancies and their pairing with Mg impurities in Mg-doped GaN layers[109,110]. Since nitrogen vacancies are expected to induce deep levels in the band gap, they are also likely to affect the luminescence properties of GaN.

Conspicuous broad peaks in the yellow, blue, and red have been observed

in the photoluminescence (PL) spectra of GaN layers synthesized under various growth conditions[111,112,113,114,115,116,117,118]. Yellow luminescence in n-type GaN has been attributed to Ga vacancies[119] and to C substituting on a N site in carbon-containing samples[120], but has also been observed in p-GaN[117,118]. The blue luminescence has often been attributed to recombination between a deep donor and a Mg acceptor[121]. The red PL band, with a peak position around 1.8 eV, has been observed in both p- and n-type GaN[121], but its origins are unknown.

Based on measurements of optically detected magnetic resonance (ODMR) in Mg-doped GaN, Bayerl *et al.* suggested that the red PL originates from recombination between a shallow donor and a deep acceptor[112,113], with the deep level being related to V_{N}[113]. On the other hand, based on a correlation between the PAS spectrum, PL and ODMR signals in such material, Zeng *et al.* concluded that the red PL originates from a deep donor to a deep acceptor transition, possibly related to V_{N} and $\mathrm{Mg}_{\mathrm{Ga}}$[110]. DFT calculations for the electronic properties of nitrogen vacancies and related complexes in GaN have also been reported[21,122]. However, the severe underestimation of band gaps in DFT precludes a direct comparison of the calculated defect levels with the observed luminescence peaks.

3.1.2 Computational details

We again use the hybrid functional[32,84] approach, as discussed in Sec. 1.4, which has also been shown to produce more accurate predictions for energetics

and electronic structure of defects in semiconductors[120]. The mixing parameter for the Hartree-Fock exchange potential is set to 31% (the original HSE value is 25%) in order to reproduce the experimental band gap of 3.5 eV. The calculated equilibrium lattice parameters of GaN, $a = 3.19$ Å and $c = 5.20$ Å, agree well with experimental data ($a = 3.189$ Å and $c = 5.185$ Å at 300 K)[123]. These calculated lattice parameters are slightly larger than those obtained by HSE calculations with the original mixing parameter (25%) as shown in Table 1.1. We calculate the formation energies of V_{N}, $\mathrm{Mg_{Ga}}$, and $\mathrm{Mg_{Ga}}$-V_{N} complexes in GaN, discuss all possible charge states, and determine optical absorption and emission energies from the calculated configuration-coordinate diagrams. The defects are simulated using a 96-atom supercell, a cutoff of 300 eV for the plane-wave basis set, and a $2\times2\times2$ k-point mesh for the integrations over the Brillouin zone.

3.1.3 Formation of nitrogen vacancies and complexes in GaN

The electronic structure of V_{N} in GaN can be understood as follows. The removal of a N atom results in four Ga dangling bonds that, in the neutral charge state, are occupied by a total of three electrons. In the near-tetrahedral environment of the wurtzite structure, these dangling bonds combine into a symmetric state (s-like symmetry) near midgap, and three almost degenerate states (p-like symmetry) near the CBM. In the neutral defect the lower state in the gap is oc-

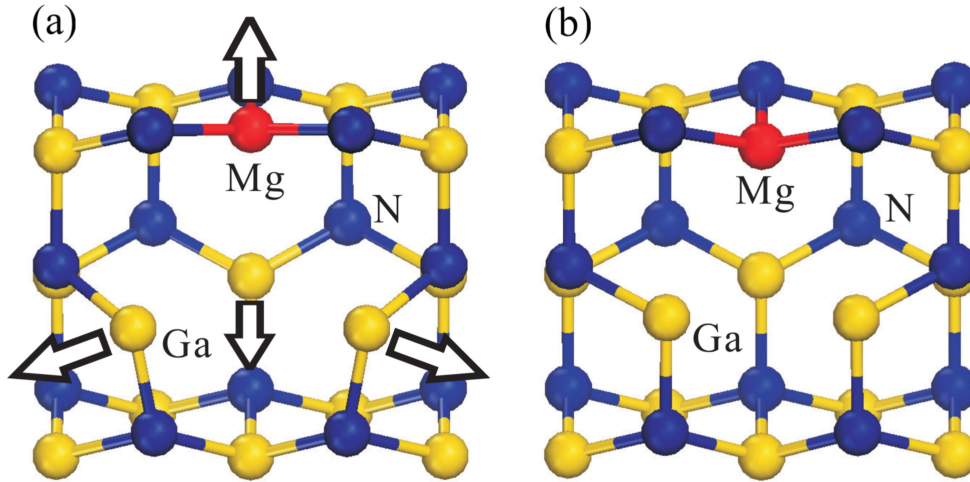

Figure 3.1: Geometry of (a) the $(\mathrm{Mg_{Ga}}\text{-}V_{\mathrm{N}})^{2+}$ and (b) the $(\mathrm{Mg_{Ga}}\text{-}V_{\mathrm{N}})^{0}$ complexes in GaN.

cupied by two electrons, and the third electron occupies the lowest of the three states near the CBM. From this picture it emerges that +, 2+, and 3+ charge states may be obtained by successively removing electrons from the V_{N} Kohn-Sham defect states. Similarly, negative charge states can in principle be obtained by adding electrons, but electron-electron repulsion will push the states upwards, i.e., closer to the CBM. Atomic relaxations will of course affect the positions of the Kohn-Sham states; whether a particular charge state is actually thermodynamically stable thus needs to be determined on the basis of its formation energy.

The $\mathrm{Mg_{Ga}}$ acceptor in neutral charge state, on the other hand, introduces a state near the VBM that is singly occupied. The association of V_{N} with $\mathrm{Mg_{Ga}}$ will result in an electron being transferred from a V_{N} state to the $\mathrm{Mg_{Ga}}$-acceptor state. The $\mathrm{Mg_{Ga}}$ will also perturb the position of the vacancy-induced gap states.

The geometries of the Mg_{Ga}-V_N complexes are shown in Fig. 3.1.

A general discussion of formation energies was given in Sec. 1.3; the formation energies of V_N, Mg_{Ga}, and the Mg_{Ga}-V_N complex are given by

$$\begin{aligned} E^f(V_{\rm N}^q) &= E_t(V_{\rm N}^q) - E_t({\rm GaN}) + \mu_{\rm N} + q\epsilon_F + \Delta^q, \\ E^f({\rm Mg}_{\rm Ga}^q) &= E_t({\rm Mg}_{\rm Ga}^q) - E_t({\rm GaN}) + \mu_{\rm Ga} - \mu_{\rm Mg} + q\epsilon_F + \Delta^q, \\ E^f[({\rm Mg}_{\rm Ga}\text{-}V_{\rm N})^q] &= E_t[({\rm Mg}_{\rm Ga}\text{-}V_{\rm N})^q] - E_t({\rm GaN}) - \mu_{\rm Mg} + \mu_{\rm Ga} \\ &\quad + \mu_{\rm N} + q\epsilon_F + \Delta^q, \end{aligned} \tag{3.1}$$

where $E_t(V_{\rm N}^q)$, $E_t({\rm Mg}_{\rm Ga}^q)$ and $E_t[({\rm Mg}_{\rm Ga}\text{-}V_{\rm N})^q]$ are the total energies of the supercells containing V_N, Mg_{Ga}, and the Mg_{Ga}-V_N complex in charge state q, and E_t(GaN) is the total energy of a perfect crystal in the same supercell.

The N atom removed from the crystal is placed in a reservoir of energy $\mu_{\rm N}$, and the Ga atom that is removed is placed in a reservoir of energy $\mu_{\rm Ga}$. The chemical potentials $\mu_{\rm N}$ and $\mu_{\rm Ga}$ can vary over a range determined by the calculated GaN formation enthalpy [$\Delta H_f({\rm GaN}) = -1.34$ eV], reflecting growth conditions that can vary from N-rich to Ga-rich. The Mg atom that is added is taken from a reservoir with energy $\mu_{\rm Mg}$. If we assume the chemical potential of Mg is limited by the formation of Mg_3N_2, with a formation enthalpy of $\Delta H_f(Mg_3N_2) = -4.8$ eV, then the upper limit of Mg chemical potential is determined by $3\mu_{\rm Mg} + 2\mu_{\rm N} = \Delta H_f(Mg_3N_2)$. Note that the formation energy of V_N is lower under Ga-rich conditions. In the case of charged defects, electrons are exchanged with the reservoir for electrons in the solid, the energy of which is the Fermi level ϵ_F,

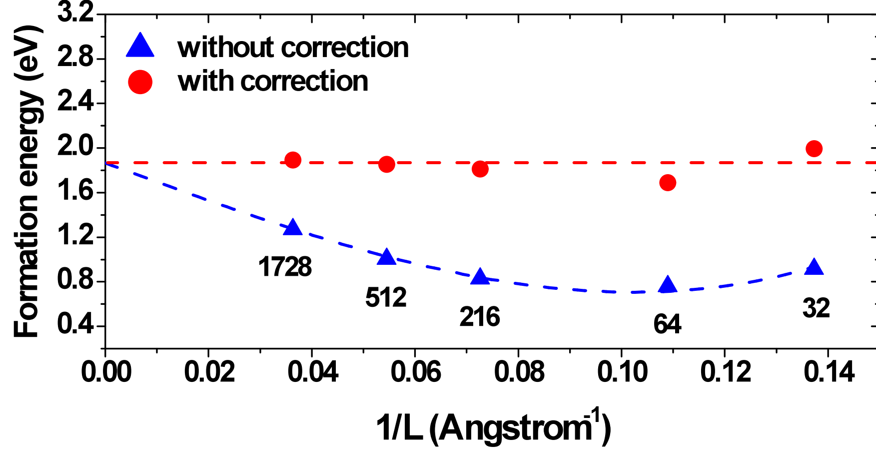

Figure 3.2: . Formation energy of the nitrogen vacancy (V_{N}^{3+}) in zinc-blende GaN obtained from GGA-PBE calculations. The data in blue are obtained without correction while those in red are obtained with finite-size correction. The blue data is best fitted by the function $E = a + b/L + c/L^3$ which is shown as a blue dashed line.

referenced to the VBM. In our calculations, finite-size corrections to formation energies as described in Sec. 1.3 are included.

As shown in Fig. 3.2, the uncorrected formation energy of a nitrogen vacancy in the 3+ charge state in zinc-blende GaN obtained from GGA-PBE calculations is dependent on the size of the unit cell. Without correction, the dependence of formation energy on $1/L$ (L is the cube root of the volume of the unit cell) is fitted

very well by $E = a + b/L + c/L^3$. The values converge quite slowly with unit-cell size. With inclusion of the finite-size correction, the formation energy converges very quickly to a value around 1.9 eV. This example indicates the importance of including finite-size corrections in order to obtain reliable formation energies and transition levels in charged defect systems. For the formation energies of V_{N} in GaN obtained in a 96-atom cell with the hybrid functional method, we obtain Δ^q values 0.13 eV, 0.61, and 1.46 eV for q=+1, 2+, and 3+ charge states, respectively.

The formation energies for the nitrogen vacancy and the $\mathrm{Mg_{Ga}}$-V_{N} complex are shown in Fig. 3.3. Both $\mathrm{Mg_{Ga}}$-V_{N} and V_{N} have low formation energies and are stable as donors when the Fermi level is near the VBM. This indicates that these defects can play an important role as compensating centers in p-GaN.

Figures 3.3a and 3.3b show that V_{N} is most stable in the 3+ charge state for Fermi-level positions near the VBM. The thermodynamic level corresponding to the transition between the 3+ and + states occurs at 0.47 eV above the VBM. The 2+ charge state is always higher in energy than the + and 3+ charge states, forming a negative-U center. In n-type GaN, in which ϵ_F is close to the CBM, the formation energy of V_{N} is very high, indicating it is unlikely to form. A transition between + and neutral charge states occurs at 0.24 eV below the CBM. We find that the negative charge state is not stable for Fermi-level positions within the band gap. Note that if the band gap is corrected by a scissors operator (meaning a rigid shift of the conduction bands with respect to the valence bands) [124], negative

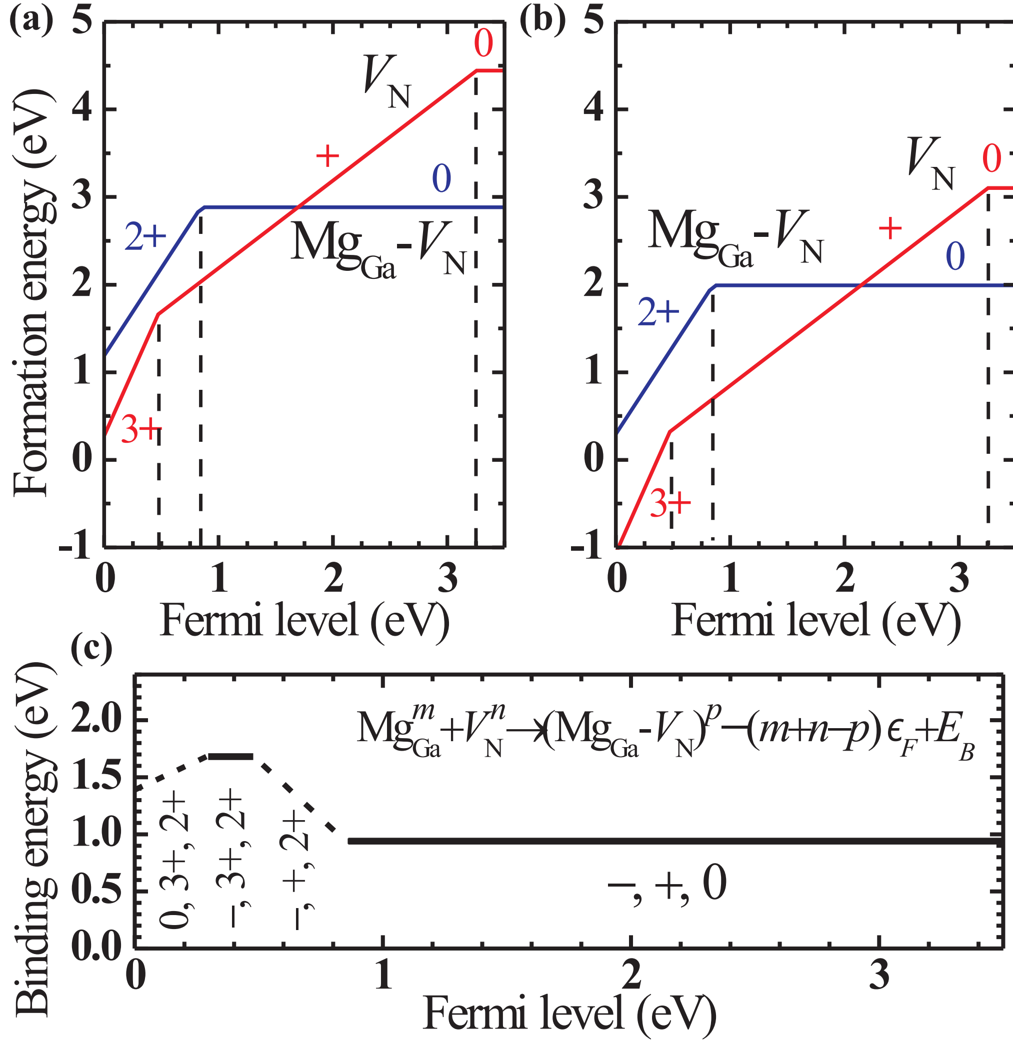

Figure 3.3: Formation energies as a function of Fermi level for the nitrogen vacancy V_N and the Mg_{Ga}-V_N complex in GaN, under (a) N-rich and (b) Ga-rich conditions. (c) Binding energies (E_B) as a function of Fermi level. In each region of Fermi level, we only take into account the defect and complex charge states with lowest formation energies and their charge states (m, n, p) are listed. The solid lines indicate processes where the charge neutrality condition is fulfilled, while the dashed lines indicate processes that require exchange of carriers with the Fermi level and may involve additional barriers.

charge states are stabilized.

The negative-U character, in which the 2+ charge state is always higher in energy than the 3+ and + states, is due to large and charge-state dependent relaxations around V_{N}. The four nearest-neighbor Ga atoms relax away from the vacancy by 1.1%, 10.8%, and 21.9% of the equilibrium Ga-N bond length for the +, 2+, and 3+ charge state, respectively. In the neutral and negative charge states, the Ga atoms surrounding the vacancy pair up and move inward, with Ga-Ga distances of 2.96 Å within each pair for V_{N}^{0} and 2.70 Å for V_{N}^{-}, significantly smaller than the Ga-Ga distances around the vacancy in the + charge state (3.23 Å).

Since Mg is an acceptor and V_{N} is a donor in GaN, we expect them to attract and form a complex. We find the stable charge states of the $\mathrm{Mg_{Ga}}$-V_{N} complex to be 2+, +, and neutral. The 2+/+ transition level occurs at 0.84 eV above the VBM, and the +/0 level at 0.89 eV. Therefore the 2+ state is stable in p-type, while the neutral state is stable in n-type GaN. As shown in Fig. 3.3c as solid lines, the binding energy (E_B) for the $(\mathrm{Mg_{Ga}}\text{-}V_{\mathrm{N}})^{0}$ complex with respect to dissociation into $\mathrm{Mg_{Ga}^{-}}$ and V_{N}^{+} is 0.94 eV, while that for $(\mathrm{Mg_{Ga}}\text{-}V_{\mathrm{N}})^{2+}$ with respect to $\mathrm{Mg_{Ga}^{-}}$ and V_{N}^{3+} is 1.69 eV. There are two other dissociation processes that require exchange of carriers with the band edges, and hence, depend on the Fermi level position: the dissociation of $(\mathrm{Mg_{Ga}}\text{-}V_{\mathrm{N}})^{2+}$ into $\mathrm{Mg_{Ga}^{0}}$ and V_{N}^{3+}, and the dissociation of $(\mathrm{Mg_{Ga}}\text{-}V_{\mathrm{N}})^{2+}$ into $\mathrm{Mg_{Ga}^{-}}$ and V_{N}^{+}. The first requires the release of

an electron, and the binding energy thus increases with Fermi level. The second requires the capture of electrons, and the binding energy decreases with the Fermi-level position. Note that these two processes may involve additional barriers due to the necessity for carrier exchange with the bulk.

The local lattice relaxations for the $(\mathrm{Mg_{Ga}}\text{-}V_\mathrm{N})^0$ and $(\mathrm{Mg_{Ga}}\text{-}V_\mathrm{N})^{2+}$ complexes are illustrated in Fig. 3.1. The three nearest-neighbor Ga atoms are displaced away from the vacancy by 21% and 9.5% of the equilibrium Ga-N bond length in the 2+ and + charge states, while in the neutral charge state they relax towards the vacancy by 1.2%; the Mg atom relaxes away from the vacancy by 20.1%, 10.0%, and 4.7% in the 2+, + and neutral charge states, respectively.

3.1.4 Luminescence of nitrogen vacancies and complexes in GaN

Given that V_N and $\mathrm{Mg_{Ga}}\text{-}V_\mathrm{N}$ are deep centers in GaN, they likely lead to characteristic absorption and emission peaks. The charge-state-dependent local lattice relaxations of the different charge states will lead to significant Stokes shifts and strong vibrational broadening of those peaks. The optical transition energies are determined from the calculated configuration-coordinate diagrams shown in Fig. 3.4. The energy difference between minima in the configuration-coordinate diagram corresponds to the zero-phonon line, and is equal to the difference between the $q/q{+}1$ transition level and the CBM. For the $\mathrm{Mg_{Ga}}\text{-}V_\mathrm{N}$ complex we identify

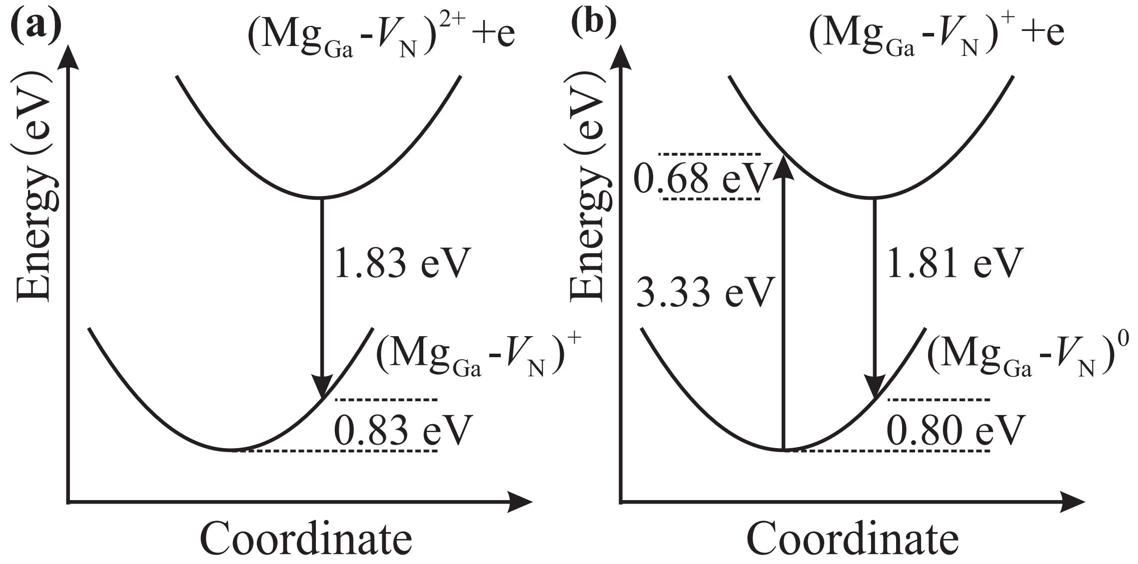

Figure 3.4: Configuration-coordinate diagrams for the Mg_{Ga}-V_N complex. (a) Illustration of the transition between an electron in the CBM (previously excited from the valence band) and the deep acceptor state related to $(Mg_{Ga}\text{-}V_N)^{2+}$ that leads to red luminescence (1.83 eV). (b) The $(Mg_{Ga}\text{-}V_N)^0$ to $(Mg_{Ga}\text{-}V_N)^+$ optical absorption starts at 2.61 eV and peaks at 3.33 eV, while the $(Mg_{Ga}\text{-}V_N)^+$ to $(Mg_{Ga}\text{-}V_N)^0$ emission peaks at 1.81 eV, in the red region of the spectrum.

two processes by which emission can be observed in PL experiments, depending on the Fermi level position.

In *p*-type GaN [Fig. 3.4(a)], where Mg doping is intentional, the Mg_{Ga}-V_N complex is stable in the 2+ charge state. During the photoluminescence process, an electron previously excited from the valence band to the conduction band can make a transition to the empty defect state of $(Mg_{Ga}\text{-}V_N)^{2+}$, i. e., $(Mg_{Ga}\text{-}V_N)^{2+} \rightarrow (Mg_{Ga}\text{-}V_N)^{+}$. The absorption energy in this case is the band-gap energy. The peak emission energy corresponds to the energy difference between $(Mg_{Ga}\text{-}V_N)^{2+}$ and $(Mg_{Ga}\text{-}V_N)^{+}$ in the lattice configuration corresponding to the initial

configuration, i.e., that of $(\mathrm{Mg_{Ga}}\text{-}V_\mathrm{N})^{2+}$. From our calculations, this results in an emission peak at 1.83 eV, with a relaxation energy of 0.83 eV as shown in Fig. 3.4(a). Our results thus indicate that $\mathrm{Mg_{Ga}}$-V_N is a source of red luminescence in *p*-type GaN, explaining the experimental observations of the red PL[114,113].

In the case of *n*-type GaN [Fig. 3.4(b)], in which Mg may be present unintentionally or due to intentional co-doping, the $\mathrm{Mg_{Ga}}$-V_N complex occurs in the neutral charge state (Fig. 3.4). An electron can be excited from the defect state to the conduction band, with a peak absorption energy of 3.33 eV, given by the energy difference between $(\mathrm{Mg_{Ga}}\text{-}V_\mathrm{N})^0$ and $(\mathrm{Mg_{Ga}}\text{-}V_\mathrm{N})^+$, both in the lattice configuration corresponding to the initial neutral charge state. Emission will occur at 1.81 eV, corresponding to the energy difference between $(\mathrm{Mg_{Ga}}\text{-}V_\mathrm{N})^+$ and $(\mathrm{Mg_{Ga}}\text{-}V_\mathrm{N})^0$ in the lattice configuration of the positive charge state. Our results thus indicate that the $\mathrm{Mg_{Ga}}$-V_N complex can also lead to broad red luminescence in *n*-type GaN[115,116].

Finally, we note that isolated V_N can also give rise to photoluminescence. We focus on *p*-type GaN, in which isolated V_N are most likely to occur, and stable in the 3+ charge state (Fig. 3.4). An electron excited to the CBM can recombine with the empty defect state, resulting in a $V_\mathrm{N}^{3+}\rightarrow V_\mathrm{N}^{2+}$ transition. The corresponding emission peaks at 2.18 eV, in the yellow region, with a relaxation energy of 0.81 eV. We thus conclude that the isolated V_N center may be a source of yellow luminescence in *p*-type GaN, consistent with experimental observations[117,118].

3.1.5 Summary

In summary, based on hybrid density functional calculations we have shown that Mg_{Ga}-V_N complexes lead to broad red luminescence in both *p*- and *n*-type GaN. We also find that isolated nitrogen vacancies can give rise to broad emission peaked at 2.18 eV. Our results provide an explanation for the mechanisms of the red and yellow luminescence signals that have been observed in Mg-containing GaN.

3.2 Optical absorption and emission due to native defects and complexes in AlN

3.2.1 Motivation

There has been great progress in the growth of high-quality bulk AlN crystals as substrates for deep-UV light-emitting devices[125,126]. Still, the UV transparency of the substrates remains an outstanding issue. Conspicuous optical absorption bands in the blue and UV range are typically observed, and nearly all AlN crystals exhibit a yellow or dark amber color due to the presence of defects. It has been widely recognized that oxygen is the main impurity that contaminates the AlN crystals, and it has been suggested that the incorporation of oxygen is accompanied by the formation of Al vacancies[127]. Recent positron annihilation studies

suggested that complexes between Al vacancies and oxygen on a nitrogen site (V_{Al}-$\mathrm{O_N}$) are the dominant form of V_{Al} in as-grown AlN samples, whereas isolated V_{Al} were detected in irradiated samples[128]. In addition, defects on the nitrogen sublattice (either $\mathrm{O_N}$ or V_{N}) have been observed by electron paramagnetic resonance (EPR)[129,130]. All these defects are expected to introduce defect states in the band gap of AlN (which is 6.2 eV wide); they may cause sub-band-gap light absorption that can interfere with the operation of optoelectronic devices. Despite these initial assignments, an explanation of the various experimental results based on detailed microscopic mechanisms has yet to emerge.

Broad peaks in blue and UV range have also been observed in the absorption spectra of AlN layers synthesized under various growth conditions including metal organic chemical vapor deposition, $\mathrm{NH_3}$−source molecular beam epitaxy, and physical vapor transport. A broad absorption band centered around 2.9 eV is frequently observed in as-grown AlN samples containing oxygen[131,132,133,134], and a correlation between the yellow coloration and this absorption band has been established[132]. A variety of origins has been proposed for this 2.9 eV absorption band, including nitrogen vacancies[131,132], Al interstitials[135], and Al vacancies[136]. No reliable physical model has been offered for how these defects give rise to this absorption band. Several other absorption bands have been observed for which the origins are also unknown: a peak at ~ 3.4 eV has been observed in irradiated AlN samples[137,128], another centered around 4.0 eV (whose peak position slightly

varies from sample to sample), and some other absorption bands in the range from 4 eV to 5.5 eV[132,133]. The 3.4 eV absorption band was tentatively attributed to nitrogen vacancies[137]; however, both Al and N vacancies can be generated by irradiation, and Al vacancies cannot be ruled out.

In addition to absorption spectra, AlN also exhibits a rich set of luminescence peaks. A luminescence band centered around 3.1−3.3 eV has been frequently observed in oxygen-containing samples[138,139,140]. Another luminescence band centered around 2.8 eV was recently observed in AlN samples with oxygen concentration around 2×10^{18} cm^{-3}; it was tentatively attributed to isolated V_{Al}[136]. First-principles calculations based on DFT for native defects and related complexes in AlN have also been reported[21,141,142,143]. However, the severe underestimation of band gaps in DFT within the standard local density or generalized gradient approximations precluded a direct comparison of the calculated defect levels with the observed absorption or emission peaks.

In this Section we address the formation energy, transition levels, and optical properties of native defects and related complexes using first-principles calculations with a hybrid functional approach. We focus on Al vacancies (V_{Al}), N vacancies (V_{N}), substitutional oxygen impurities ($\mathrm{O_N}$), and complexes between Al vacancies and oxygen (V_{Al}-$\mathrm{O_N}$). The absorption and emission energies are extracted from the calculated configuration-coordinate diagrams. Based on our results we explain the mechanisms behind the absorption and emission bands that

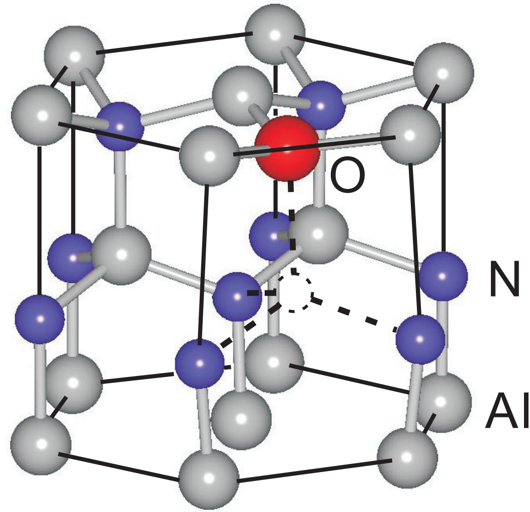

Figure 3.5: Geometry of the $(V_{\mathrm{Al}}\text{-}\mathrm{O_N})^{2-}$ complex. Dashed lines indicate the position of the missing N atom.

are observed in the AlN spectrum.

3.2.2 Computationals details

The calculations are based on generalized Kohn-Sham theory[144], projector augmented wave (PAW) potentials[145,89], and the screened hybrid functional of Heyd, Scuseria, and Ernzerhof (HSE)[32,84], as implemented in the VASP code[90]. The mixing parameter for the Hartree-Fock exchange potential is set to 32%, which reproduces the experimental band gap for AlN. The increase in the mixing parameter results in a larger band gap of 6.14 eV compared with our earlier HSE calculations as shown in Table 1.1. The defects are simulated using a 96-atom supercell, a cutoff of 400 eV for the plane-wave basis set, and a 2×2×2 k-point mesh for the integrations over the Brillouin zone.

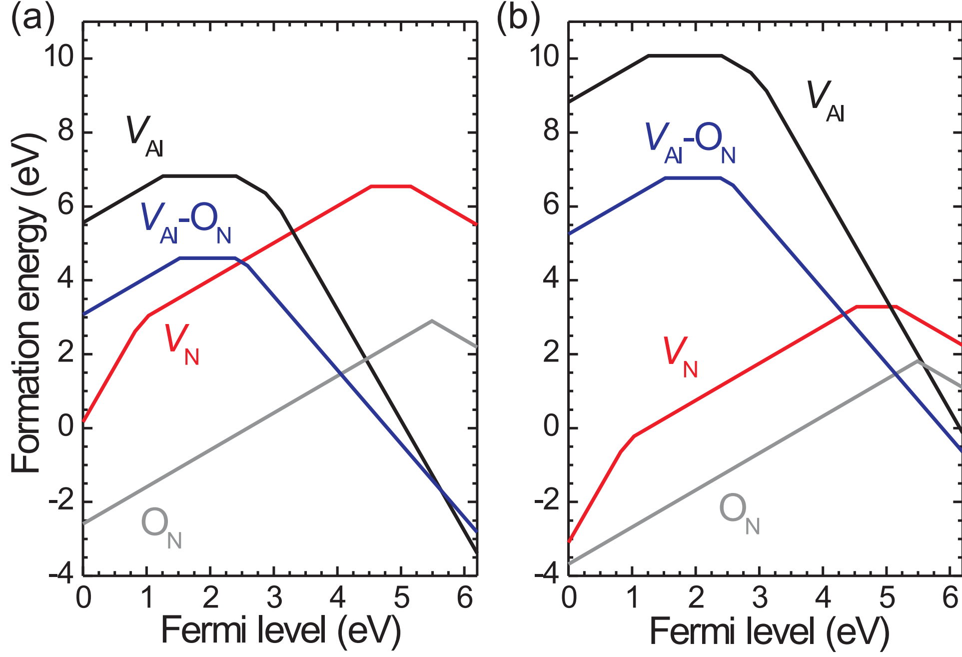

Figure 3.6: Formation energies as a function of Fermi level for the nitrogen vacancy V_N, aluminum vacancy V_{Al}, oxygen impurity O_N, and the V_{Al}-O_N complex, under (a) N-rich and (b) Al-rich conditions.

3.2.3 Formation of native defects and complexes in AlN

We again follow the general definition of formation energy given in Sec. 1.3. The formation energy of the V_{Al}-O_N complex is given by

$$E^f[(V_{Al}\text{-}O_N)^q] = E_t[(V_{Al}\text{-}O_N)^q] - E_t(\text{AlN}) - \mu_O + \mu_{Al} + \mu_N + q\epsilon_F + \Delta^q, \quad (3.2)$$

where $E_t[(V_{Al}\text{-}O_N)^q]$ is the total energy of the supercell containing a V_{Al}-O_N complex in charge state q, and $E_t(\text{AlN})$ is the total energy of a perfect crystal in the same supercell.

The Al atom removed from the crystal is placed in a reservoir of energy μ_{Al},

and the N atom that is removed is placed in a reservoir of energy μ_{N}. The chemical potentials μ_{Al} and μ_{N} are referenced to the energy per atom of Al bulk and N_2 molecules, and can vary over a range determined by the calculated formation enthalpy of AlN [$\Delta H_f(\mathrm{AlN}) = -3.18$ eV], reflecting growth conditions all the way from Al-rich to N-rich. The oxygen atom is taken from a reservoir with energy μ_{O}, referenced to the energy per atom of the O_2 molecule. We assume the chemical potential of oxygen is limited by the formation of Al_2O_3, with a calculated formation enthalpy of $\Delta H_f(\mathrm{Al_2O_3}) = -16.2$ eV. The upper limit of μ_{O} is then determined by $2\mu_{\mathrm{Al}} + 3\mu_{\mathrm{O}} = \Delta H_f(\mathrm{Al_2O_3})$. Due to the choice of Al_2O_3 as the solubility-limiting phase for μ_{O}, which introduces a dependence on the host chemical potentials, the formation energy of the complex is different under Al-rich and N-rich conditions. In the case of charged defects, electrons are exchanged with the reservoir for electrons in the solid, the energy of which is the Fermi level ϵ_F, referenced to the VBM. The last term in Eq. (3.2), Δ^q, is the correction for charged defects due to the finite size of the supercell, as described in Sec. 1.3.

When forming an Al vacancy, the removal of the Al atom results in four N dangling bonds. In the near-tetrahedral environment of the wurtzite structure, these p-like states are split in a singlet and a triplet state. In the neutral charge state, these states are occupied by a total of three electrons. By successively adding electrons to the Kohn-Sham states of the defect, 1−, 2−, and 3− charge states may be obtained. Addition of electrons to the vacancy results in an outward

breathing relaxation: in the $3-$ charge state the three equivalent nitrogen atoms move outward by 11% of the bond length, while the N atom along the c-axis moves outward by 16%.

The association of $V_{\rm Al}$ and $\rm O_N$, resulting in a $V_{\rm Al}$-$\rm O_N$ complex, involves an electron being transferred from the $\rm O_N$ state to the $V_{\rm Al}$ state. Since oxygen p states are lower in energy than nitrogen p states, the defect states will move closer to the VBM. The local lattice relaxations for the $(V_{\rm Al}\text{-}{\rm O_N})^{2-}$ complex are illustrated in Fig. 3.5. The three nearest-neighbor N atoms are displaced away from the vacancy by 9.3% and 9.1% of the equilibrium Al-N bond length in the $2-$ and $1-$ charge states; the O atom along the c-axis relaxes away from the vacancy by 14.1% and 13.9% in the $2-$ and $1-$ charge states, respectively.

As shown in Fig. 3.6, the $V_{\rm Al}$ has a low formation energy when the Fermi level is in the upper part of the band gap, where it is stable in a 3– charge state. The 2–/3– thermodynamic transition level is located at 3.11 eV above the VBM. Similarly, the $V_{\rm Al}$-$\rm O_N$ complex is most stable for ϵ_F values high in the gap, with a charge state of 2–; the –/2– transition level occurs at 2.59 eV above the VBM. Note that $V_{\rm Al}$-$\rm O_N$ complexes have lower formation energy than isolated vacancies for most Fermi-level positions within the band gap, under both Al-rich and N-rich conditions. The binding energy (E_b) of the $(V_{\rm Al}\text{-}{\rm O_N})^{2-}$ complex with respect to dissociation into $\rm O_N^+$ and $V_{\rm Al}^{3-}$ is 1.12 eV, indicating that there is indeed a strong driving force for Al vacancies and oxygen impurities to form complexes.

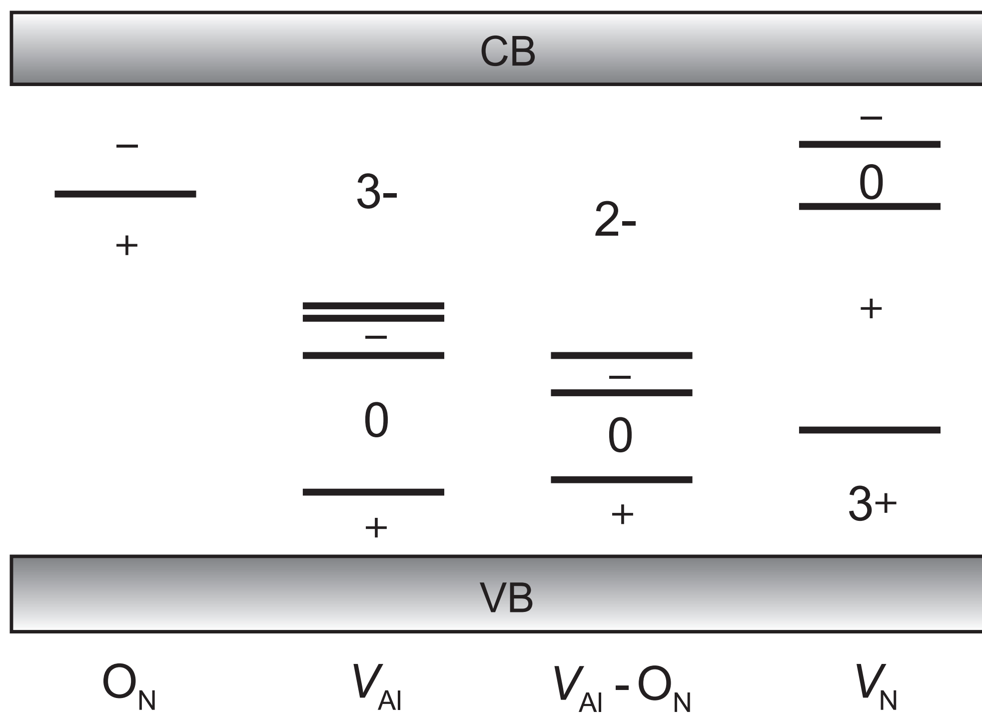

Figure 3.7: Thermodynamic transition levels obtained from formation energies of defects. The conduction and valence bands are denoted by CB and VB.

3.2.4 Optical signatures of native defects and complexes in AlN

The kinks in the curves of Fig. 3.6 correspond to thermodynamic transition levels; these levels are summarized in Fig. 3.7. All of these defects potentially lead to characteristic absorption and emission peaks. The optical transition energies are determined from the configuration-coordinate diagrams shown in Fig. 3.8. The energy difference between minima of the two curves in such diagrams corresponds to the zero-phonon line, and is equal to the energy difference between the $q/q{+}1$ transition level (Fig. 3.6) and the CBM (for transitions involving electrons in the CB) or the VBM (for transitions involving holes in the VB). The local lattice relaxations are quite different for different charge states and lead to significant Stokes shifts and strong vibrational broadening of absorption and emission peaks.

In the absence of intentional doping, the Fermi-level is most likely to occur in the upper part of the band gap, because of the tendency of the material to incorporate donor-type impurities, particulaly oxygen. When the Fermi level is above 3.11 eV (in the case of $V_{\rm Al}$) or above 2.59 eV (for $V_{\rm Al}$-$\rm O_N$), the defect states of both $V_{\rm Al}$ and $V_{\rm Al}$-$\rm O_N$ are fully occupied. Optical absorption can therefore only involve transitions from occupied defect states to empty CB states (or shallow donors). The peak absorption energy corresponds to the energy difference between $V_{\rm Al}^{3-}$ as the initial state and $V_{\rm Al}^{2-}$ fixed in the lattice configuration of $V_{\rm Al}^{3-}$ as the final state. This results in an absorption peak at 3.43 eV, with a relaxation energy of

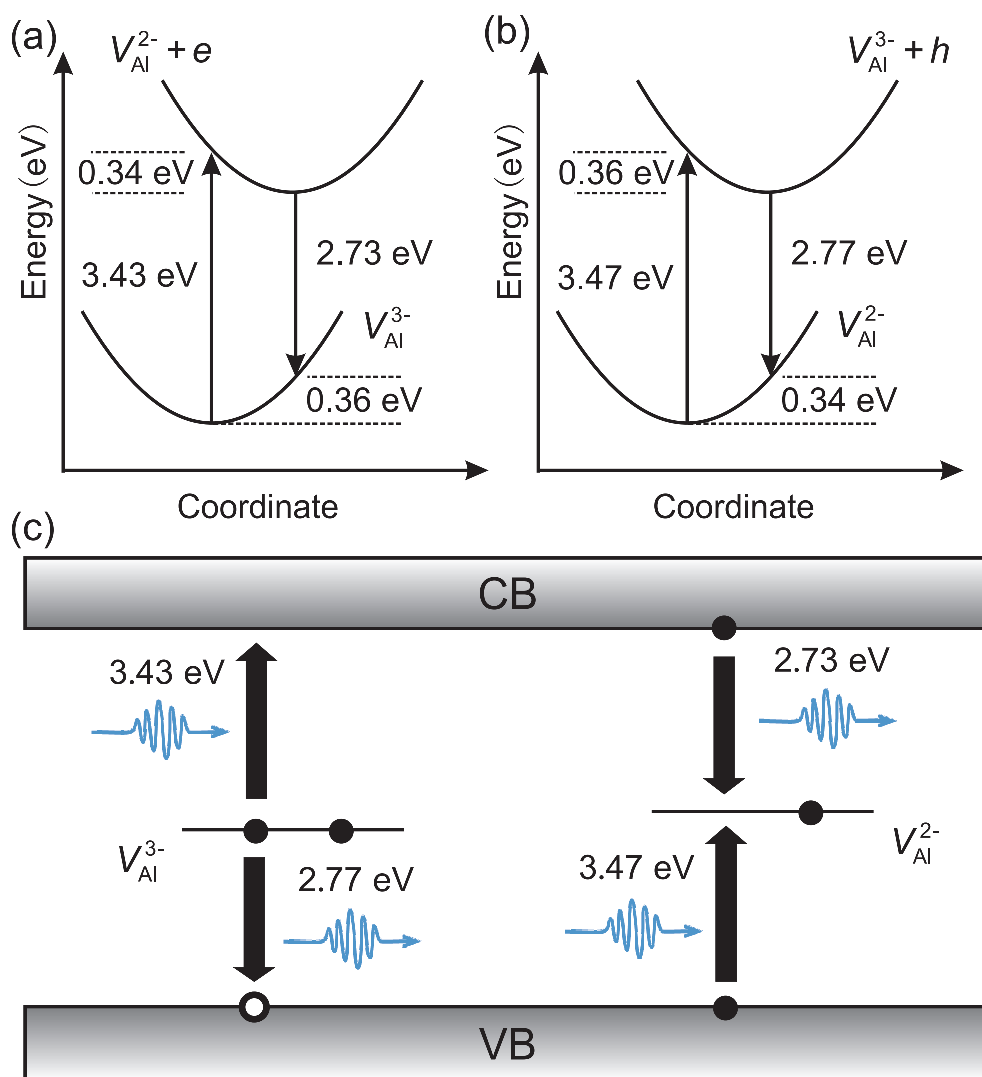

Figure 3.8: Configuration-coordinate diagrams for $V_{\rm Al}$. (a) Transition between an electron in the deep acceptor state and the CBM. (b) Transition between the deep acceptor state and a hole in the VBM. (c) Schematic of absorption and emission related to $V_{\rm Al}$.

0.34 eV as shown in Fig. 3.8a. This peak agrees very well with the absorption peak observed at around 3.4 eV in irradiated samples[137,128]. Since nitrogen vacancies are also likely to form during irradiation, we also calculate the absorption due to the nitrogen vacancy. We find that the absorption due to the nitrogen vacancy does not match the observed absorption at 3.4 eV. We can therefore attribute the 3.4 eV absorption peak to V_{Al} formed during irradiation.

After excitation has taken place, the electron in the conduction band can recombine with a hole in the defect state, leading to luminescence. For V_{Al}^{2-} this results in an emission peak at 2.73 eV, with a relaxation energy of 0.36 eV [Fig. 3.8a]. This result explains the observed photoluminescence band centered around 2.78 eV[136].

Figure 3.9 illustrates the transitions associated with the V_{Al}-$\mathrm{O_N}$ complex. Optical absorption corresponds to a transition $(V_{\mathrm{Al}}\text{-}\mathrm{O_N})^{2-}\rightarrow(V_{\mathrm{Al}}\text{-}\mathrm{O_N})^{-}$ which gives rise to an absorption peak at 3.97 eV, with a relaxation energy of 0.36 eV [Fig. 3.9a]. This result thus indicates that V_{Al}-$\mathrm{O_N}$ is a source of the absorption band around 4.0 eV observed in as-grown AlN bulk crystals containing a large amount of oxygen[132,133]. The electrons excited into the CB can recombine with the defect state, resulting in an emission peak at 3.24 eV, with a relaxation energy of 0.37 eV [Fig. 3.9a]. We can therefore assign the luminescence band centered around 3.1−3.3 eV observed in oxygen-containing samples[138,139,140] to a transition involving an electron in the CB with $(V_{\mathrm{Al}}\text{-}\mathrm{O_N})^{1-}$.

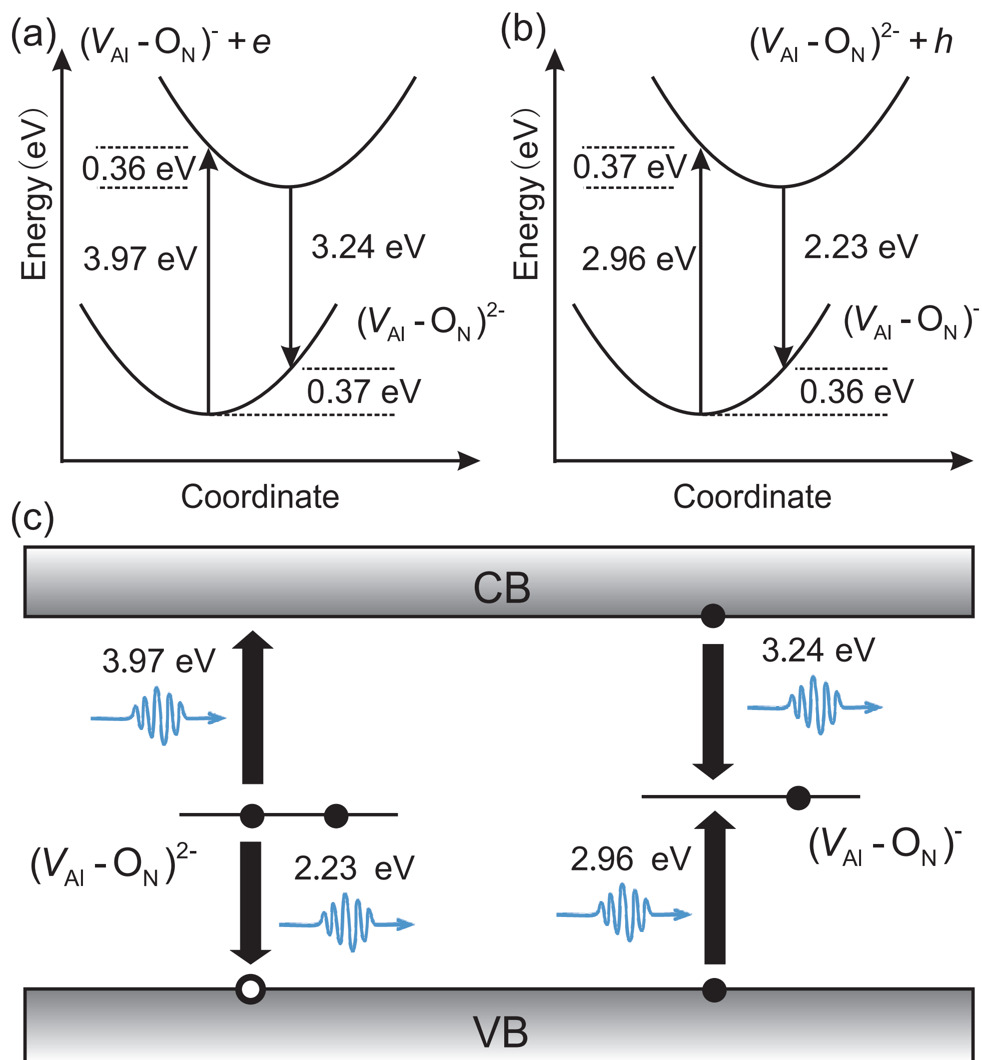

Figure 3.9: Configuration-coordinate diagrams for V_{Al}-$\mathrm{O_N}$. (a) Transition between an electron in the deep acceptor state and the CBM. (b) Transition between the deep acceptor state and a hole in the VBM. (c) Schematic of absorption and emission related to V_{Al}-$\mathrm{O_N}$.

3.2.5 Summary

In summary, based on hybrid density functional calculations we have shown that isolated aluminum vacancies lead to an absorption peak at 3.43 eV and an emission peak at 2.73 eV, providing mechanisms for the absorption signal around 3.4 eV observed in irradiated AlN samples, and luminescence signal around 2.78 eV observed containing relatively low levels of oxygen. V_{Al}-$\mathrm{O_N}$ complexes give rise to absorption peaked at 3.97 eV and emission peaked at 3.24 eV, explaining the absorption signal at around 4.0 eV and luminescence band around 3.1−3.3 eV in oxygen-containing AlN.

3.3 Excitonic effect on optical absorption from nitrogen vacancies in AlN

3.3.1 Motivation and computational details

The removal of unwanted light absorption in AlN due to defects is critical to fabricate high performance AlN-based optoelectronic devices. It is hence important to establish the correlation between specific defects in AlN samples and optical signatures in absorption spectra. In the previous Section we addressed the link between defect electronic structure and optical spectra through the use of configuration-coordinate diagrams. At that level of description, we ignored that

in semiconductor materials electrons and holes pair up and form excitons during optical excitation. From the theoretical point of view, this many-body effect must be taken into account in studying the optical absorption spectrum wtihin a more accurate theoretical framework. In this Section, we will show how excitonic interaction affects the absorption spectrum of defects.

We carry out quasiparticle band structure calculations within the many-body perturbation theory which takes into account electronic exchange and correlation effects by including the electron self-energy operator in the GW approximation[146]. Subsequently, we calculate the optical spectrum by solving the Bethe-Salpeter equation (BSE) of correlated electron-hole excitations[37,147]. As explained in Sec. 1.4, the BSE approach has become a standard procedure for optical excitations and has already been applied to a number of defect systems including LiCl[148], SiC[149], and CaF_2[150].

We use the BerkeleyGW package[35,147,151] to calculate the quasiparticle properties and the optical responses. The package takes as input the Kohn-Sham DFT eigenvalues and eigenvectors computed with the Quantum Espresso code[152]. The local spin-density approximation and norm-conserving Troullier-Martins pseudopotentials are used in the ground state calculations. All structural optimizations are carried out at the experimental lattice constants of a=3.112 Å and c=4.982 Å. Note that the experimental lattice constants are different from the equilibrium lattice constants obtained with LDA and HSE (see Table 1.1), which induces

a small strain in defect systems. However, the lattice parameters differ by less than 1%, and the atomic structures obtained at experimental lattice constants are very similar to the structures obtained by HSE calculations in the previous Section. For the bulk AlN system, 250 empty bands are included in empty-state summations when calculating dielectric functions. For the defect system, we employ a supercell of 96 atoms and the empty-state summations include 2880 empty bands, corresponding to 120 empty bands for a primitive four-atom unit cell. The reciprocal-space summations employ 8 k points for the dielectric matrix and the self-energy operator, and 32 k points for the representation of optical excitations. When calculating absorption spectra, 18 valence bands and 12 conduction bands are included, yielding excitation energies converged to about 0.1 eV.

3.3.2 Results for the excitonic effects in optical absorption

We first carry out GW+BSE calculations for bulk AlN material at the experimental lattice constants (a=3.112 Å, c=4.982 Å). Figure 3.10 shows our results for the dielectric function $\epsilon_2(\omega)$ of wurtzite AlN for light polarized parallel to the c-axis. Without excitonic effects, there are three main peaks in the absorption spectrum below an excitation energy around 20 eV, which are denoted as E_1, E_2, and E_3, respectively. These features are consistent with previous theoretical results[153] calculated in the single-particle scheme. BSE calculations result in significant changes in the absorption spectrum. The E_1 peak is shifted toward lower

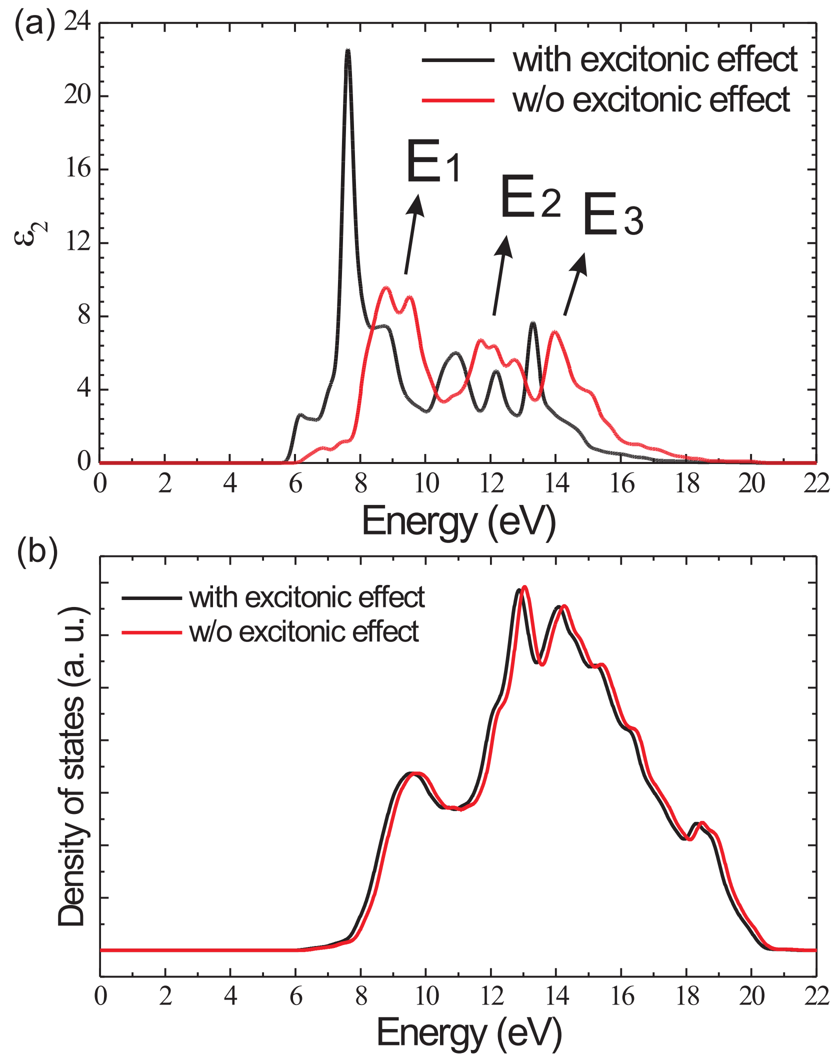

Figure 3.10: (a) Dielectric function of the wurtzite AlN obtained from G_0W_0 and BSE calculations. (b) Joint density of states of wurtzite AlN calculated from G_0W_0 quasiparticle band structures and density of excited states obtained from BSE calculations.

energies and becomes stronger, indicating the formation of a bound state. The peaks at energies E_2 and E_3 are also shifted toward lower energies and become small shoulders rather than well-defined peaks. Overall, all of these features agree with a previous theoretical study[154] based on BSE calculations.

Our study of the excitonic effects in optical absorption is focused on the nitrogen vacancy (V_N) in AlN. In an AlN crystal, a nitrogen vacancy is formed by removing a nitrogen atom from the lattice. The dangling bonds of the four neighboring Al atoms combine to form bonding and antibonding states. These defect states can interact with both the conduction and valence band and serve as recombination centers. As shown in the previous Section (Fig. 3.6), V_N is most stable in the 3+ charge state for Fermi-level positions near the VBM, while the thermodynamic level corresponding to the transition between the 3+ and + states occurs at 0.89 eV above the VBM. In the 3+ charge state, the bonding state is located above the VBM and is unoccupied. During an optical absorption process, electrons in the valence band may be excited into this defect state, leaving holes in the valence band. The electron-hole pairs in such defect systems may form localized excitons.

In order to study the excitonic effect on optical excitation, we carry out G_0W_0 calculations to obtain quasiparticle band structures using LDA as a starting point. Fortunately, the bonding state of V_N^{3+} from LDA is well above the VBM (as shown in Fig. 3.11a) and its wavefunction is localized and does not mix with valence

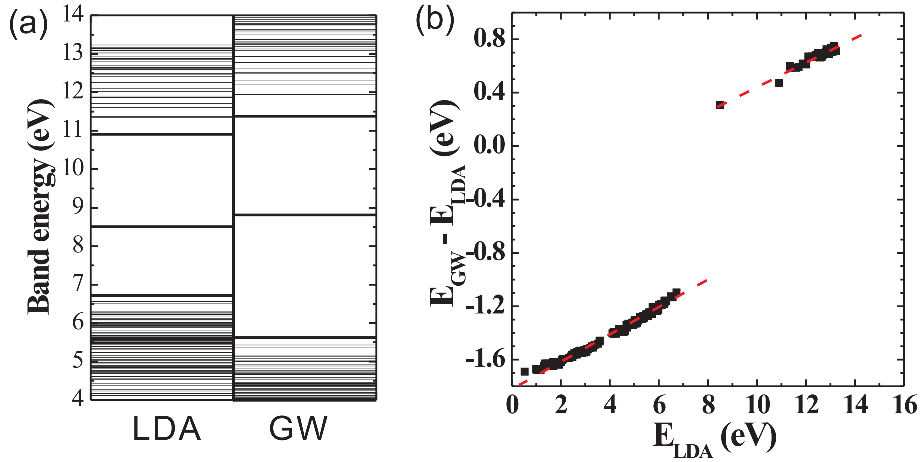

Figure 3.11: (a) Eigenenergies of V_{N}^{3+} at the Γ point from LDA and G_0W_0 calculations. (b) Energy shift of eigenstates between G_0W_0 and LDA calculations as a function of LDA eigenenergies.

bands. This validates the use of G_0W_0 calculations in which LDA wavefunctions are used as approximations of quasiparticle wavefunctions.

As shown in Fig. 3.11a, the Kohn-Sham state a1 is located at 1.76 eV above the VBM at the Γ point in LDA, while its position relative to the VBM increases by 1.44 eV due to G_0W_0 corrections. Figure 3.11b shows the energy shift of eigenstates between G_0W_0 and LDA calculations as a function of LDA eigenenergies. The G_0W_0 corrections open up the gap and induce different shifts of valence and conduction bands. These shifts of both valence and conduction bands are close to linear. Interestingly, the shift of the bonding state of the defect falls on the same line as the conduction-band states. This may be related with the fact that the defect state consists of the dangling bonds of neighboring Al atoms and their

characters are similar to conduction bands in AlN. It indicates that the G_0W_0 correction will shift the absorption spectrum to a higher energy due to the change in the quasiparticle excitation energies.

Next we will explore how electron-hole interaction affects absorption energies. We assume that the Fermi level is very close to the VBM and V_{N} is stable in the 3+ charge state. In this case, the defect state a1 is empty above the VBM and transitions occur from the VBM into this defect state. The joint density of states calculated from G_0W_0 quasiparticle band structures and the density of excited states from BSE calculations are shown in Fig. 3.12a. The density of excited states obtained from BSE calculations with electron-hole interaction is shifted to lower energies by around 0.3 eV compared with the joint density of states calculated from the G_0W_0 quasiparticle band structure. A strong peak centered around 3.7 eV is observed in the dielectric function shown in Fig. 3.12b due to the transitions from valence bands to the bonding defect state. By considering the electron-hole interaction, the peak position is changed to 3.1 eV. Obviously this change is different from the shift in density of states, which means it is not simply due to the change in excitation energies. Instead, such change comes from the excitonic effect, which effectively modifies the transition matrix elements and induces a redistribution in two-particle excitations with stronger excitations at lower energies.

Detailed information about the spatial properties of the exciton is obtained

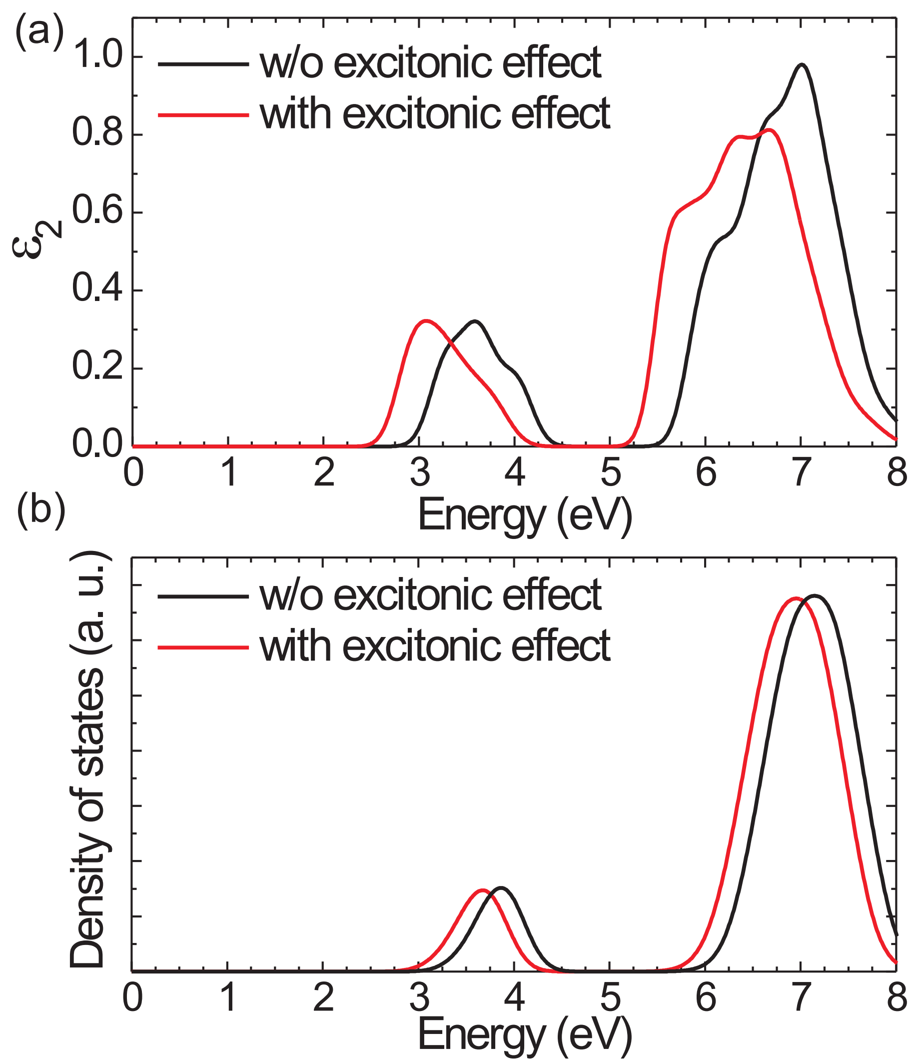

Figure 3.12: (a) Dielectric function of the wurtzite AlN containing a nitrogen vacancy in 3+ charge state obtained from G_0W_0 and BSE calculations. (b) Joint density of states calculated from G_0W_0 quasiparticle band structures and density of excited states obtained from BSE calculations.

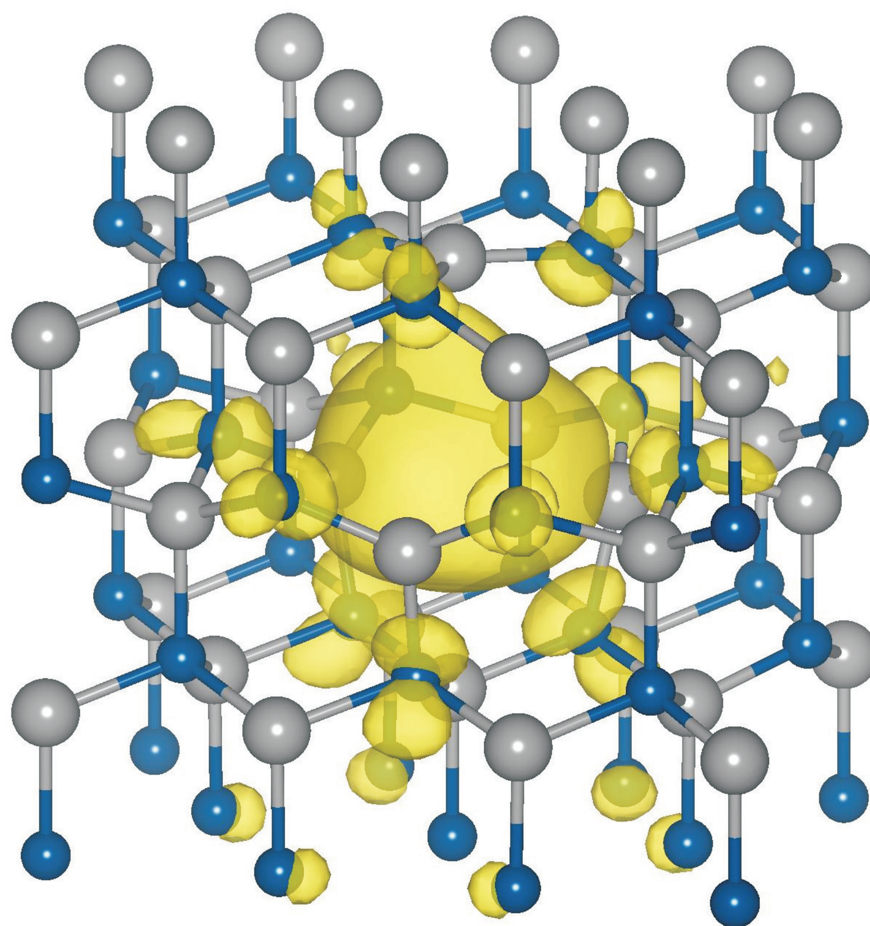

Figure 3.13: Spatial distribution of the electron relative to the hole fixed at the vacancy center, for the exciton at 2.7 eV excitation energy.

from the two-particle wavefunction. In order to show such a two-particle wavefunction, we can fix one particle at a certain position and plot the wavefunction of the other particle. Figure 3.13 shows the resulting distribution of the electron wavefunction around the hole fixed at the vacancy site. Overall the wavefunction has s character localized near the vacancy and some p character on the second-nearest-neighbor N atoms. The quantitative details, however, are very complex. The electron is localized at the defect within about 4 Å, but it also has significant amplitude on the neighboring atoms. The localization of the electron is caused by the Coulomb attraction to the hole resulting from the electron-hole interaction, which is taken into account in the BSE scheme.

3.3.3 Summary

In summary, we have investigated the optical excitation of bulk AlN and the nitrogen vacancy in AlN using first-principles many-body perturbation theory. Our calculations show that both the G_0W_0 correction and the BSE treatment affect the absorption spectrum. The exciton is strongly localized around the vacancy. We cannot compare the calculated optical spectrum directly with experiment, since in real materials atomic and electronic degrees of freedom are coupled and the line width of optical absorption is significantly affected by vibronic coupling. Further efforts are needed to address this issue in a many-body interaction framework.

Chapter 4

Device simulation of nitride-based LEDs

In this chapter, we study the performance of polar, nonpolar, and semipolar nitride-based LED devices using semi-empirical device simulations. Nitride-based light-emitting diodes (LEDs) and laser diodes (LDs) grown on nonpolar and semipolar bulk GaN substrates have been widely studied experimentally and theoretically[155,156,157,158]. Compared to conventional devices grown on the *c* planes, devices on nonpolar and semipolar planes are expected to have higher internal efficiency due to the reduction or even elimination of internal polarization[20]. The lighting efficiencies of semipolar and nonpolar nitride-based light emitters have shown superior performance over those *c*-plane devices. However, there is still room for improvement. For example, the carrier distribution is not uniform in

multi-QW structures of LEDs and only a few quantum wells near the p side are emitting light during device operation. There is clear evidence that this phenomenon is associated with the carrier transport issue. On the other side, the effects of the polarization field on the performance of semipolar LEDs is still not clear. We will show that device simulations can help in explaining the difference in those semipolar and nonpolar devices compared with traditional c-plane devices.

4.1 Droop problem and polarization field

4.1.1 Motivation

As mentioned in the Introduction chapter, the internal quantum efficiency (IQE) of nitride-based LEDs can be described by the ABC model and the appearance of the droop issue under high current injection is due to the Auger recombination (Cn^3 term in ABC model). It has been suggested that the values of the A, B, and C coefficients are affected by the polarization fields[159]. This seems to provide a promising way to improve the high-current performance of nitride LEDs by increasing the electron-hole wavefunction overlap in quantum wells through novel device design. Here we report an analysis (performed in collaboration with E. Kioupakis) of electron-hole wavefunction overlap in various QW structures. We build on the fact[160] that the A, B, and C coefficients are all proportional to the square of the overlap F between the electron (ψ_c) and hole (ψ_v)

wavefunctions: $F = \int \psi_v^*(\boldsymbol{r})\psi_c(\boldsymbol{r})d\boldsymbol{r}$.

4.1.2 Wavefunction overlap in polar and nonpolar quantum wells

We performed the simulations using the SimuLED code. The strain and piezoelectric polarization charges in nonpolar and semipolar heterostructures are calculated with the approach suggested in Ref. 20. The piezoelectric constants for InN, GaN, AlN are taken from Ref. 161,162,163 while the spontaneous polarization constants are taken from Ref. 14. We study the operation of nitride LEDs and elucidate the behavior of the IQE by examining the wavefunction overlap as a function of the In content and the bias voltage. As shown in Fig. 4.1, in c-plane quantum wells, the polarization fields keep the electron and hole wavefunctions at opposite ends of the QW both under zero [Fig. 4.1(a)] and finite bias [Fig. 4.1(b)]. Moreover, increasing In concentrations in the QW enhances the strain and piezoelectric fields and further reduces the overlap (Fig. 4.2), deteriorating the device efficiency. The nonpolar QW exhibits much better behavior. Under zero bias the electron and hole wavefunctions are kept apart by the junction field [Fig. 4.1(c)]. This increases the value of all carrier-recombination coefficients (A, B, and C), which are proportional to the square of the overlap, $|F|^2$.

Since the IQE is a ratio of recombination rates, it is independent of the wavefunction overlap and therefore has the same value both for the polar and the

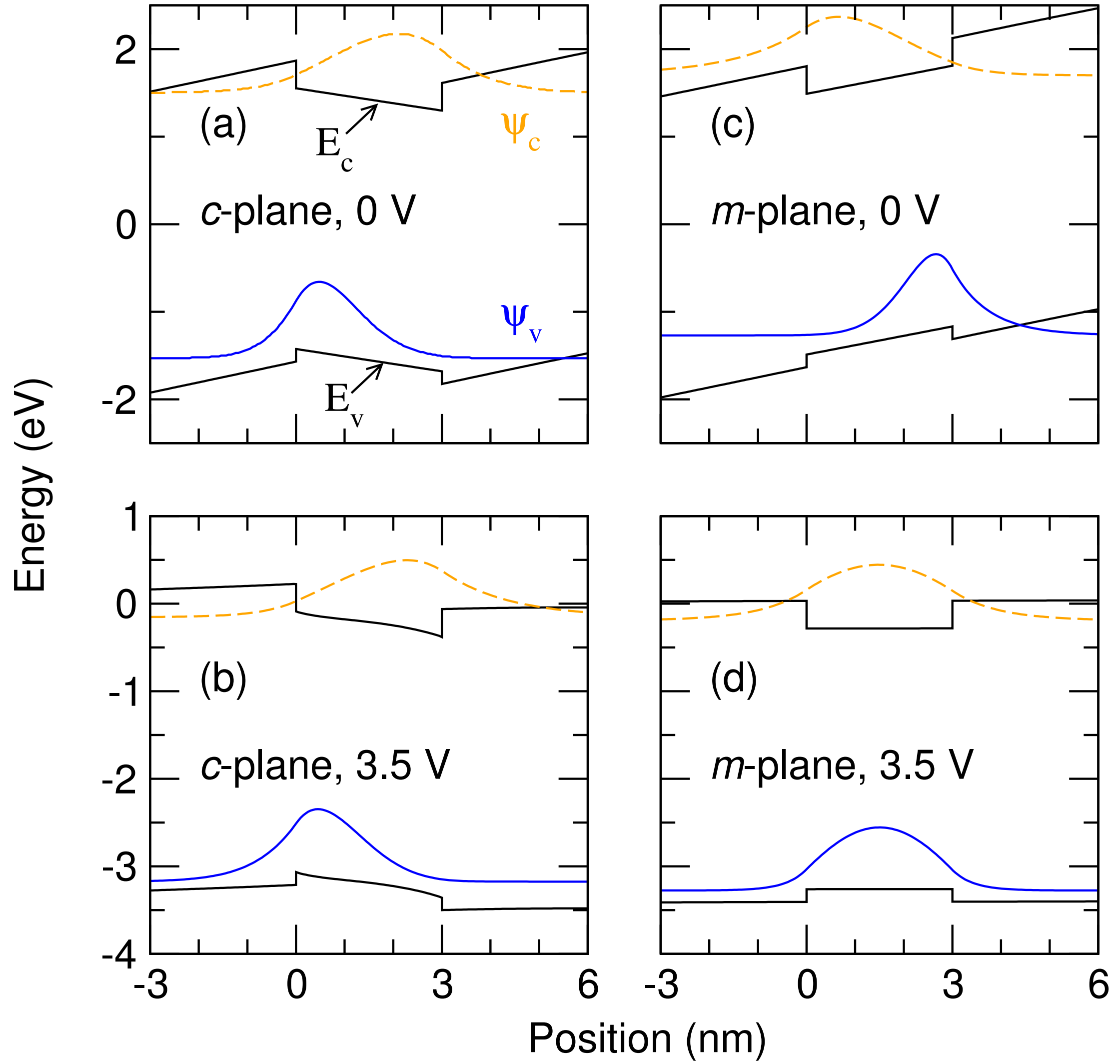

Figure 4.1: Calculated electron (ψ_c) and hole (ψ_v) wavefunctions and conduction (E_c) and valence (E_v) band profiles for an $\mathrm{In}_x\mathrm{Ga}_{1-x}\mathrm{N}$ QW ($x = 0.12$), for the c-plane [(a) and (b)] and the m-plane [(c) and (d)] growth, under zero bias [(a) and (c)] or a 3.5 V applied voltage [(b) and (d)]. The absence of polarization fields in the m-plane device increases the electron-hole overlap and improves the efficiency.

nonpolar LED for fixed n. However, the radiated power at a given n is higher for the nonpolar device because the increased overlap enhances the B coefficient. In other words, for a given injected current density the operating carrier density is lower in the nonpolar LED (because carriers recombine faster), and this increases the IQE. This conclusion was previously reached experimentally for polar LEDs with varying In content and hence varying polarization fields[159]. Our simulation results verify this picture and explain how the enhanced wavefunction overlap of nonpolar devices significantly improves the high-power efficiency for all emission wavelengths [Fig. 4.1(d)].

The simulated IQE versus current density curves (Fig. 4.3) show the improved efficiency of nonpolar devices. In order to simulate the IQE curves, for the bulk recombination parameters we use typical values from experiment[164] ($A_0 = 5 \times 10^7$ s^{-1}, $B_0 = 2 \times 10^{-11}$ cm^{3}s^{-1}, and $C_0 = 10^{-30}$ cm^{6}s^{-1}). Theoretically obtained values for the B_0 and C_0 coefficients are in agreement with these measurements[165] and qualitatively produce the same conclusions. The c-plane device exhibits the efficiency-droop and green-gap problems under both optical excitation [zero bias, Fig. 4.3(a)] and electrical injection [3.5 V bias, Fig. 4.3(b)]. On the other hand, the m-plane device shows efficiency droop that *improves* with increasing In content under optical excitation [Fig. 4.3(c)], while for electrical injection [Fig. 4.3(d)] droop is significantly suppressed and the efficiency is almost independent of the emission wavelength.

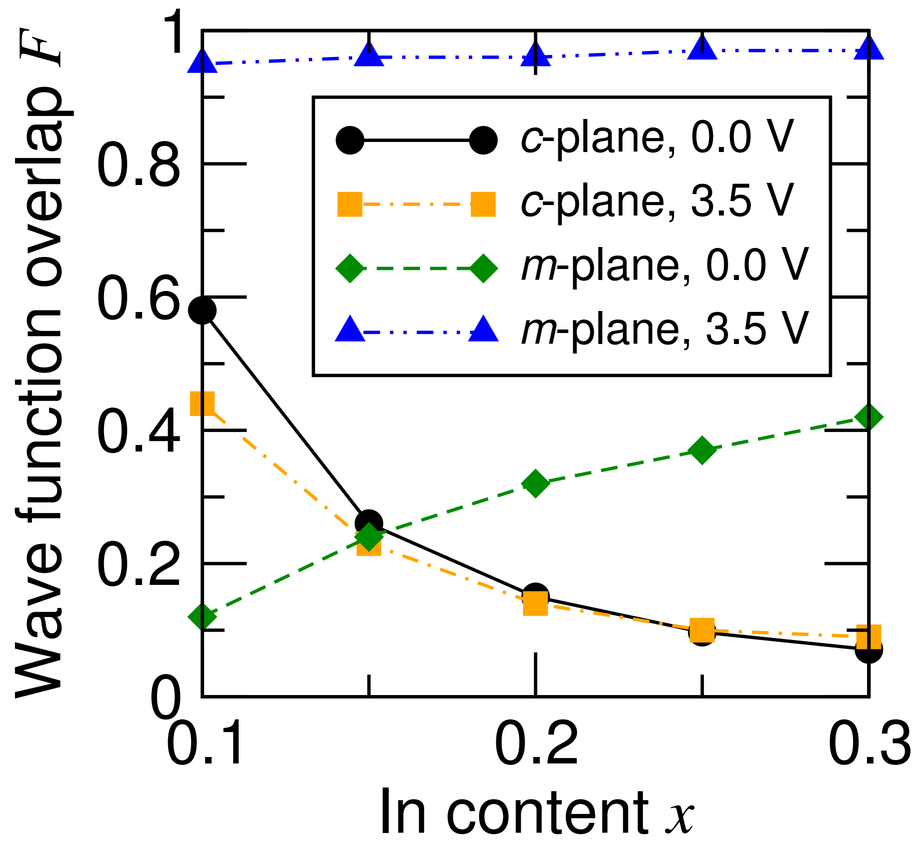

Figure 4.2: Electron-hole wavefunction overlap as a function of In content and applied voltage for the c- and m-plane growth. The overlap for the nonpolar device is much larger than its polar counterpart under electrical-injection conditions and does not decrease for increasing In content.

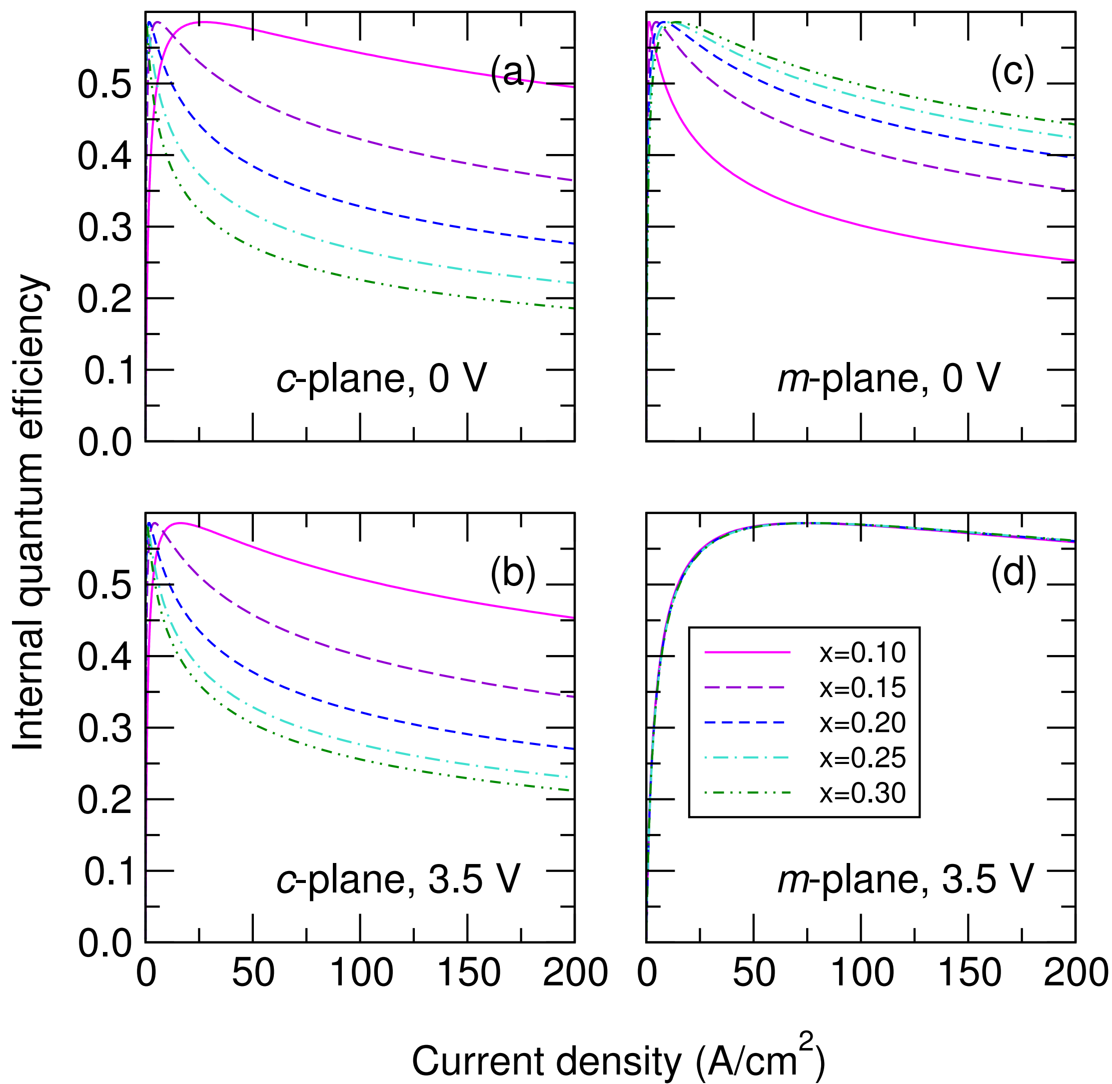

Figure 4.3: Calculated internal quantum efficiency versus current density for c-plane [(a) and (b)] and m-plane [(c) and (d)] growth, under zero bias [i.e. optical injection, (a) and (c)] or a 3.5 V applied voltage [(b) and (d)]. The polar c-plane device shows the characteristic droop and green-gap problems (b). The nonpolar m-plane LED displays much better performance (d).

As the In content increases, the QW confines electrons and holes more effectively and the higher dielectric constant reduces the electric field in the well; these effects combine to improve the droop behavior at longer wavelengths [Figs. 4.3(c) and 4.2]. The free carriers generate a counteracting screening field. This field (estimated to be less than 0.05 V/nm for carrier densities of 10^{19} cm^{-3}) partially cancels out the junction field (on the order of 0.1 V/nm), increase the carrier overlap, and improve the IQE at high carrier densities compared to our unscreened estimates. Nevertheless, the IQE behavior in Fig. 4.3(c) remains qualitatively correct. A finite (3.5 V) applied bias creates flat-band conditions [Fig. 4.1(d)] and the resulting overlaps approach 100% (Fig. 4.2), independent of In content.

4.1.3 Summary

We have presented an analysis of internal quantum efficiency in nitride QW LEDs that highlights the interplay between polarization fields and recombination rates. The reduction in polarization fields in nonpolar quantum wells increases the electron-hole overlap, which increases not only the radiative recombination rate but also the nonradiative rates, all by the same factor. These changes in recombination rates give less droop for nonpolar LED devices under device operation condition compared with *c*-plane devices. Hence the improvements due to nonpolar or semipolar growth or polarization engineering are attributable to the ability to operate at lower carrier densities. Device designs that suppress the

polarization fields in the QWs will alleviate the droop and green-gap problems. Semipolar and nonpolar growth have already yielded devices with superior performance. A different approach to minimize the polarization fields in polar devices is by engineering the quantum barriers, for example, quaternary AlGaInN or InGaN barriers which reduce polarization charges at the QW-barrier interfaces and enhance the electron-hole overlap in polarization-matched structures.

4.2 Carrier transport and the effect of the barrier modification

4.2.1 Hole transport in multiple-quantum-well structures

In typical nitride-based LEDs, MQW structures are adopted to lower the carrier density per QW. However, it has been reported that holes mostly populate the top QW nearest to the *p* side, and the resulting uneven hole distribution is expected to reduce the overall recombination rate for the *c*-plane LEDs[166]. Such an uneven hole distribution is expected to exist also in semipolar LEDs. So far, MQW LEDs with emission wavelengths larger than 500 nm and output powers comparable to those of SQW LEDs have not been demonstrated on semipolar planes. Improvements in carrier transport in MQW structures are needed to increase the output powers of semipolar LEDs. Recently, a reduction in voltage was observed when Mg doping was introduced into the middle barrier of the $(20\bar{2}1)$

double-quantum-well (DQW) LEDs[167]. This result suggests the existence of carrier transport problems in long-wavelength $(20\bar{2}1)$ MQW LEDs and provides a potential solution to improve the hole injection efficiency by Mg doping in the barriers. In this Section, we report theoretical simulations on the effects of Mg doping in the barriers of $(20\bar{2}1)$ DQW LEDs with emission wavelengths in the green region. This work was performed in collaboration with experimental researchers in the Solid State Lighting and Energy Center, in particular Chia-Yen Huang, Yuji Zhao, Kenji Fujito, and Daniel Feezell[167].

4.2.2 Experimental spectra of double-quantum-well LEDs

To examine the influence of Mg-doped barriers on the hole transport between QWs, our experimental collaborators grew dichromatic DQW LEDs with undoped or Mg-doped middle barriers by metalorganic chemical vapor deposition (MOCVD) on free-standing $(20\bar{2}1)$ GaN substrates[167]. The thicknesses of the QWs and the barriers were estimated to be 3 nm and 10 nm, respectively. Secondary ion mass spectroscopy (SIMS) confirmed the Mg concentration in the barrier to be 6×10^{18} cm^{-3}. The p-side QW was grown at $765°C$ while the n-side QW was grown at $865°C$. The emission wavelengths for the two QWs were $515-520$ nm and $410-420$ nm, respectively. After the growth of the active region, a 10 nm p-type $Al_{0.2}Ga_{0.8}N$ electron blocking layer (EBL) was deposited, followed by a 100 nm p-GaN capping layer. Only a single peak in the green region was observed in

the electroluminescence spectra for the dichromatic double quantum well $(20\bar{2}1)$ LEDs with undoped barriers, which implied that most of the recombination took place in the QW near the p side and that the holes mostly populated the top QW under injection currents up to 100 mA. On the other hand, the emission in the green region dominated under low current injection in the electroluminescence spectra for the double quantum well LEDs with Mg-doped barriers (with dopant concentration of 6×10^{18} cm^{-3})[167]. As the injection current was increased, the emission in the violet region emerges and the intensity became comparable to that of the green emission at higher injection levels. Clearly, the emission spectra suggest the existence of hole transport problems in long-wavelength $(20\bar{2}1)$ DQW LEDs. These experimental observations suggest a potential solution to improve the hole injection efficiency in MQW LEDs by Mg doping in barriers.

4.2.3 Effects of Mg doping on the hole distribution in DQW LEDs

To examine the effects of the Mg doping in the barriers on the band diagram, device simulations of the LED structures are carried out using the SiLENSe code developed by the STR Group[168]. The parameters used in our simulations are the same as in Sec. 4.1. The potential distribution and quasi-Fermi levels are calculated by solving the Schrödinger-Poisson equations self-consistently. A drift-diffusion current model is used for the simulation of the device operation under

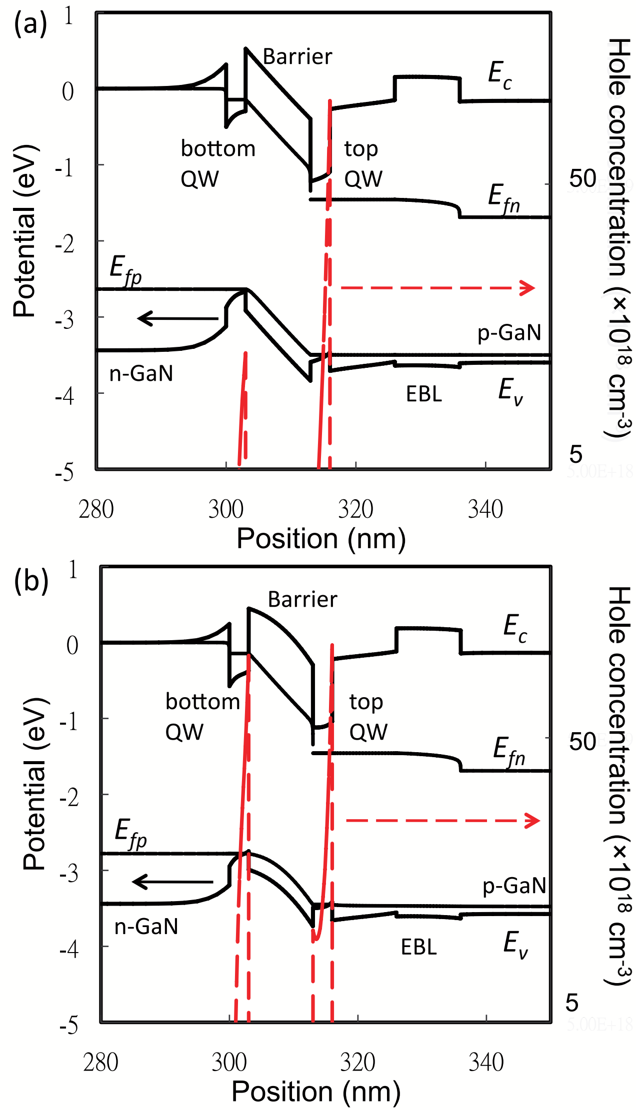

Figure 4.4: Simulated band diagrams and hole concentrations of (2021) DQW green LEDs with (a) undoped and (b) Mg-doped barriers.

high bias voltage (3.5 V). The strain and polarization effects in the semipolar InGaN/GaN structures are accounted for.

Figures 4.4a and 4.4b show the simulated band diagrams for the $(20\bar{2}1)$ DQW green LEDs with and without Mg doping in the middle barrier, respectively. Due to the inverse polarization in the QWs on the $(20\bar{2}1)$ plane compared to those on the plane[20], an additional energy barrier (ΔE) is present for carriers traversing the QWs. With lower effective mass and broader distribution of kinetic energy, electrons overcome the energy barrier more easily than holes. The injected holes are scattered by the additional energy barrier caused by internal polarization in the QW. As shown in Fig. 4.4b, after Mg doping of the barrier, the band bending in the barrier creates a reduced effective barrier thickness for holes, which enhances hole transport. Overall, the injection current and hole concentration in both QWs are both increased after Mg doping.

Together with the experimental observations, the simulations explain the difficulty in making high-brightness MQW LEDs with long-wavelength emission. As the number of QWs increases, the electrons are distributed among the wells but most of the holes populate the QW closest to the p side. This reduces the radiative efficiency of the remaining QWs. The addition of Mg doping in the middle barrier enhances hole transport between the QWs and improves the radiative efficiency of the QW closer to the n side. Considering the trade-off between enhanced carrier transport and radiative efficiency in each QW, the overall radiative efficiency of

the active region is increased with an optimized Mg doping profile in the barriers.

4.2.4 Summary

In conclusion, we have presented evidence that hole transport between QWs is a limiting factor for the performance of long-wavelength LEDs on the $(20\bar{2}1)$ plane. Simulations confirm that with Mg doping in the middle barrier, the effective barrier thickness for holes between adjacent QWs is reduced due to the band bending. The simulation also suggests that the hole concentration in the QWs and the injection current are increased under the same bias with Mg doping, which is consistent with the experimental results. These results indicate that improving hole injection efficiency is key to enhancing the performance of MQW green LEDs.

4.3 Optical spectrum of $(20\bar{2}1)$ and $(20\overline{21})$ semipolar LEDs

4.3.1 Experimental observations: dependence of emission wavelengths on the inclination angle

Semipolar and nonpolar planes have been extensively investigated for the growth of high-indium-content quantum wells (QWs) in green light-emitting diodes (LEDs) and laser diodes (LDs)[169,170,171]. One advantage of nonpolar and semipo-

lar growth is the elimination or reduction of polarization-related electric fields in the QWs, which are responsible for the reduced radiative recombination rate and large blue shift observed in conventional *c*-plane emitters[15,172,173]. The issues associated with polarization-related electric fields are exacerbated for higher indium content QWs.

Semipolar planes have been shown theoretically and experimentally to exhibit superior performance over the *c*-plane devices. For example, the semipolar $(11\bar{2}2)$ plane was reported to have binding sites that may accommodate indium atoms more easily than either the *c* plane or the *m* plane[174]. Additionally, long-wavelength yellow LEDs have been demonstrated on this plane[175]. However, the formation of misfit dislocations (MDs) within the active region has been observed and is known to degrade the device performance[176]. The semipolar $(20\bar{2}1)$ plane, which is miscut by 15° toward the *c* plane from the *m* plane, has been utilized to produce high-performance green LEDs[177,178]. More recently, several advantageous features, including high optical polarization ratio, small wavelength shift, and low efficiency droop, were reported for blue-green $(20\overline{21})$ LEDs[179,180] and LDs[181]. In this Section, we will discuss the impacts of the indium composition and polarization-related electric fields on the emission wavelengths of nonpolar and semipolar devices. This work was again performed in collaboration with experimentalists in the Solid State Lighting and Energy Center, in particular Yuji Zhao, Chia-Yen Huang, Shih-Chieh Huang, Po Shan Hsu, Shinichi Tanaka, Chih-

Chien Pan, Yoshinobu Kawaguchi, Kenji Fujito, and Daniel Feezell[179].

Recent electroluminescence (EL) measurements on InGaN SQWs grown on different planes show that, with the same TMI flow and growth temperature, devices grown on $(20\overline{2}\overline{1})$ planes with higher inclination angles from the m plane exhibit longer emission wavelengths than those on less-inclined planes[179]. Furthermore, although characterized by identical strain conditions[20], the semipolar $(20\overline{2}1)$ plane (Ga-polar character) consistently exhibits higher indium incorporation than the semipolar $(20\overline{2}\overline{1})$ plane (N-polar character). Similar results were also observed on the $(30\overline{3}1)$ and $(30\overline{3}\overline{1})$ planes[182]. Interestingly, although similar indium compositions are extracted from x-ray diffraction (XRD) analysis for the coherent structures on the $(20\overline{2}1)$ plane and the $(20\overline{2}\overline{1})$ plane, those on the $(20\overline{2}1)$ plane exhibit longer emission wavelengths[179]. Similar results are also observed when comparing the m plane and the $(11\overline{2}2)$ plane, with $(11\overline{2}2)$ exhibiting longer emission wavelengths[179].

4.3.2 Simulations: polarization fields and emission wavelengths

To clarify these phenomena, we carried out device simulations for blue-green LED structures using the SiLENSe code[168]. The parameters used in our simulations are the same as in Sec. 4.1. The potential distributions are calculated by solving the Poisson equation self-consistently, including the strain and polariza-

tion effects. The polarization field in the $In_{0.25}Ga_{0.75}N$ alloy grown on different planes and its dependence on the inclination angle respect to the c-axis are shown in Fig. 1.2. Obviously, the polarization changes dramatically with the inclination angle and has opposite sign for Ga-polar (e.g., $(20\overline{2}1)$) and N-polar planes (e.g., $(20\overline{2}\overline{1})$).

For ease of interpretation, identical SQW LED structures (with 25% indium composition) are simulated under a current density of 20 A/cm^2. The calculated band diagrams and peak emission wavelengths for $(20\overline{2}1)$, $(20\overline{2}\overline{1})$, $(11\overline{2}2)$ and m-plane devices are shown in Fig. 4.5(a)−(d). For a given indium composition, the emission wavelengths of the $(20\overline{2}1)$ and $(20\overline{2}\overline{1})$ LEDs are approximately 10−15 nm longer than those of the $(11\overline{2}2)$ and m-plane LEDs. These differences can be explained by the magnitudes and directions of polarization-related electric fields in the QWs. For the $(20\overline{2}1)$ and $(11\overline{2}2)$ planes, the polarization-related electric field in the QWs is in the same direction as the p-n junction built-in electric field, while for the $(20\overline{2}\overline{1})$ plane the polarization-related electric field opposes the p-n junction built-in electric field. For the m plane, the polarization-related electric field is zero and only the p-n junction built-in electric field exists in the QWs in the unbiased case. As a result, distinct potential profiles are obtained in the QWs of $(20\overline{2}1)$, $(20\overline{2}\overline{1})$, $(11\overline{2}2)$ and m-plane devices.

At a low current density (20 A/cm^2), InGaN QWs on the $(20\overline{2}1)$ and $(11\overline{2}2)$ planes exhibit triangular potential profiles, since the polarization-induced electric

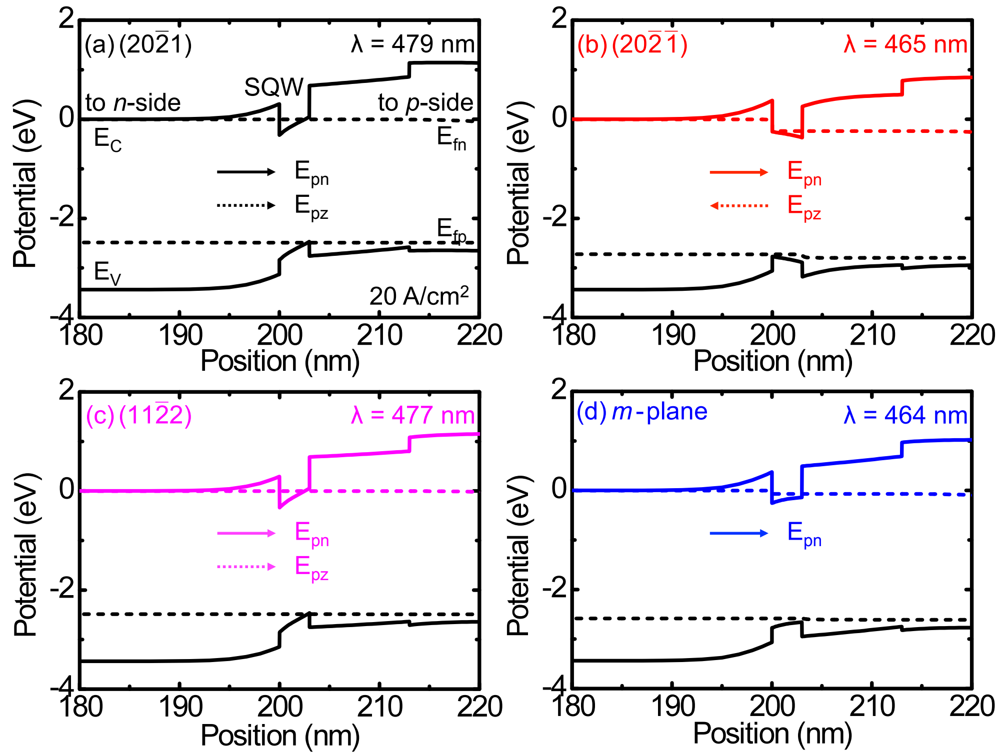

Figure 4.5: Simulated band diagrams and emission wavelengths for the SQW InGaN (with 0.25 indium composition) blue-green LEDs on the (a) $(20\bar{2}1)$, (b) $(20\bar{2}\bar{1})$, (c) $(11\bar{2}2)$, and (d) m-planes under a current density of 20 mA/cm^2.

field and the p-n junction built-in electric field are along the same direction. Conversely, QWs on the $(20\overline{2}\overline{1})$ plane exhibit relatively flat potential profiles, since the polarization-related electric field and the p-n junction built-in electric field are opposite in direction and nearly equal in magnitude. The m-plane QWs also exhibit relatively flat potential profiles beyond diode turn-on. For a given indium composition, this triangular potential profile produces a red shift in the emission and contributes to the longer emission wavelengths observed on $(20\overline{2}1)$ and $(11\overline{2}2)$ compared to the m plane and $(20\overline{2}\overline{1})$, respectively. However, the red shift at low current densities in $(20\overline{2}1)$ and $(11\overline{2}2)$ QWs is counteracted at larger current densities by carrier-induced screening of the electric fields and the cumulative result is a blue shift of the emission wavelength with increasing current. Instead, LEDs on $(20\overline{2}\overline{1})$ show very little blue shift since in the low current case the potential profile in QW is already relatively flat.

4.3.3 Summary

In summary, we have carried out device simulations to study the role of polarization fields in the emission wavelength of semipolar and nonpolar LED devices. We demonstrate that both the indium composition and the magnitude and direction of the polarization-related electric fields in the QWs affect the emission wavelength. These results are qualitatively explained by the different magnitudes and directions of polarization-related electric fields in the QWs on the different

planes, which lead to various degrees of band bending in the QWs. For planes on which the polarization-related electric field and the p-n junction built-in electric field are additive, a triangular potential profile results in the QWs and a red shift in the emission wavelength is obtained. This results in a strong blue shift with increasing current injection. For some planes on which the polarization-related electric field and the p-n junction built-in electric field are along opposite directions, a relatively flat potential profile can be obtained. This leads to a shorter emission wavelength for a given indium composition but much smaller blue shift.

Chapter 5

Summary and outlook

With the motivation to explain and assist the experimental development of high-performance solid state optoelectronic devices, we have employed a set of computational approaches for the study of nitride materials and devices. A wide range of applications has been presented, ranging from the basic structural and electronic properties of the nitride materials to the effects of strain, defects, polarization fields, and device design on the optoelectronic device performance. We have shown that these computational approaches provide powerful explanatory and predictive computational tools that can assist and guide the experimental development of efficient solid state optoelectronic devices. With these computational approaches, we are well-equipped to focus on any remaining unresolved as well as new questions in this field.

One question relates to the physical properties of InGaN or AlGaN nitride

alloys with high In or Al compositions. It is usually assumed that the properties of alloys can be obtained from linear interpolation of those of binary compounds. For some physical properties of the InGaN or AlGaN alloys, including deformation potentials and elastic constants, this assumption has not been validated. Further efforts are needed to clarify this. In addition, there is a need for a physical model to address the inhomogeneous strain and fluctuations in In or Al compositions in InGaN or AlGaN alloys, and their effects on the optical properties of nitride-based light emitters.

Another area that deserves further investigation is the study of the absorption spectrum due to the defects in nitride materials and the development of a first-principles approach to enable the direct comparison with experimental data. Since the electronic and atomic structures are coupled and the line width of optical absorption is significantly affected by vibronic coupling[183], a realistic absorption spectrum for defects cannot be obtained only with GW+BSE calculations. Further efforts are needed to address this issue within a many-body interaction framework.

With continued pressure to increase the efficiency of nitride light emitters, it becomes crucial now to better understand the role of defects and impurities in the device performance. It is well known that these defects usually induce deep levels in the gap, and these deep levels can behave as nonradiative recombination centers and lower the device efficiency at low current. However, such effects have

not yet been quantified from first principles and need to be assessed in the future.

Finally, we turn to the device modeling of nitride optoelectronic devices. In the drift-diffusion model, the quantum effect of carrier tunneling between quantum wells is not taken into account. The lack of such quantum effects in this model is the probable cause of the discrepancy between theoretical predictions and experimental observations, particularly the difference in turn-on voltage and current. This issue is currently being studied and several tentative solutions, such as artificially decreasing the polarization constants[184] or the inclusion of a modified "quantum potential"[185], have been proposed to achieve a better agreement with experiment. A more fundamental solution would be to employ quantum transport theory using non-equilibrium Green's functions. Further investigations are needed to more accurately describe the carrier transport in nitride-based optoelectronic devices.

Bibliography

[1] S. Pimputkar, J. S. Speck, S. P. DenBaars, and S. Nakamura. Prospects for LED lighting. *Nature Photonics*, 3:180, 2009.

[2] H. J. Round. A note on Carborundum. *Electrical World*, 49:309, 1907.

[3] O. V. Losev. Luminous carborundum detector and detection effect and oscillations with crystals. *Phil. Mag.*, 6:1024, 1928.

[4] S. Nakamura, M. Senoh, and T. Mukai. P-GaN/n-InGaN/n-GaN double-heterostructure blue-light-emitting diodes. *Jpn. J. Appl. Phys.*, 32:L8, 1993.

[5] A. Laubsch, M. Sabathil, J. Baur, M. Peter, and B. Hahn. High-power and high-efficiency InGaN-based light emitters. *IEEE T. Electron Dev.*, 57:79, 2010.

[6] M. H. Kim, M. F. Schubert, Q. Dai, J. K. Kim, E. F. Schubert, J. Piprek, and Y. Park. Origin of efficiency droop in GaN-based light-emitting diodes. *Appl. Phys. Lett.*, 91:183507, 2007.

[7] B. Monemar and B. E. Sernelius. Defect related issues in the current roll-off in InGaN based light emitting diodes. *Appl. Phys. Lett.*, 91:181103, 2007.

[8] Y. C. Shen, G. O. Mueller, S. Watanabe, N. F. Gardner, A. Munkholm, and M. R. Krames. Auger recombination in InGaN measured by photoluminescence. *Appl. Phys. Lett.*, 91:141101, 2007.

[9] A. David and N. F. Gardner. Droop in III-nitrides: Comparison of bulk and injection contributions. *Appl. Phys. Lett.*, 97:193508, 2010.

[10] W. Shockley and W. T. Read. Statistics of the recombinations of holes and electrons. *Phys. Rev.*, 87:835, 1952.

[11] J. Piprek. Efficiency droop in nitride-based light-emitting diodes. *phys. stat. sol. (a)*, 207:2217, 2010.

[12] J. Hader, J. V. Moloney, B. Pasenow, S. W. Koch, M. Sabathil, N. Linder, and S. Lutgen. On the importance of radiative and auger losses in GaN-based quantum wells. *Appl. Phys. Lett.*, 92:261103, 2008.

[13] K. T. Delaney E. Kioupakis, P. Rinke and C. G. Van de Walle. Indirect Auger recombination as a cause of efficiency droop in nitride light-emitting diodes. *Appl. Phys. Lett.*, 98:161107, 2011.

[14] F. Bernardini, V. Fiorentini, and D. Vanderbilt. Spontaneous polarization and piezoelectric constants of III-V nitrides. *Phys. Rev. B*, 56:R10024, 1997.

[15] F. Bernardini and V. Fiorentini. Spontaneous versus piezoelectric polarization in III-V nitrides: Conceptual aspects and practical consequences. *phys. stat. sol. (b)*, 216:391, 1999.

[16] T. Takeuchi, C. Wetzel, S. Yamaguchi, H. Sakai, H. Amano, I. Akasaki, Y. Kaneko, S. Nakagawa, Y. Yamaoka, and Yamada N. Determination of piezoelectric fields in strained GaInN quantum wells using the quantum-confined Stark effect. *Appl. Phys. Lett.*, 73:1691, 1998.

[17] P. Lefebvre, A. Morel, M. Gallart, T. Taliercio, J. Allègre, B. Gil, H. Mathieu, B. Damilano, N. Grandjean, and J. Massies. High internal electric field in a graded-width InGaN/GaN quantum well: Accurate determination by time-resolved photoluminescence spectroscopy. *Appl. Phys. Lett.*, 78:1252, 2001.

[18] J. W. Matthews. *Dislocations in Solids*. North-Holland, Amsterdam, 1979.

[19] J. F. Nye. *Physical Properties of Crystals*. Oxford University Press, New York, 1985.

[20] A. E. Romanov, T. J. Baker, S. Nakamura, and J. S. Speck. Strain-induced polarization in wurtzite III-nitride semipolar layers. *J. Appl. Phys.*, 100:023522, 2006.

[21] C. G. Van de Walle and J. Neugebauer. First-principles calculations for

defects and impurities: Application to III-nitrides. *J. Appl. Phys.*, 95:3851, 2004.

[22] C. Freysoldt, J. Neugebauer, and C. G. Van de Walle. Fully ab initio finite-size corrections for charged-defect supercell calculations. *Phys. Rev. Lett.*, 102:016402, 2009.

[23] R. M. Martin. *Electronic Structure, Basic Theory and Practical Methods.* Cambridge University Press, 2004.

[24] J. P. Perdew, K. Burke, and M. Ernzerhof. Generalized gradient approximation made simple. *Phys. Rev. Lett.*, 77:3865, 1996.

[25] D. M. Ceperley and B. Alder. Ground state of the electron gas by a stochastic method. *Phys. Rev. Lett.*, 45:566, 1980.

[26] E. Wigner. On the interaction of electrons in metals. *Phys. Rev.*, 46:1002, 1934.

[27] M. Gell-Mann and K. A. Brueckner. Exact Kohn-Sham exchange potential in semiconductors. *Phys. Rev.*, 106:364, 1957.

[28] C. Stampfl and C. G. Van de Walle. Density-functional calculations for III-V nitrides using the local-density approximation and the generalized gradient approximation. *Phys. Rev. B*, 59:5521, 1999.

[29] P. Rinke, M. Winkelnkemper, A. Qteish, D. Bimberg, J. Neugebauer, and M. Scheffler. Consistent set of band parameters for the group-III nitrides AlN, GaN, and InN. *Phys. Rev. B*, 77:075202, 2008.

[30] I. Vurgaftman and J. R. Meyer. Band parameters for nitrogen-containing semiconductors. *J. Appl. Phys.*, 94:3675, 2003.

[31] A. D. Becke. A new mixing of HartreeFock and local density-functional theories. *J. Chem. Phys.*, 98:1372, 1993.

[32] J. Heyd, G. E. Scuseria, and M. Ernzerhof. Hybrid functionals based on a screened Coulomb potential. *J. Chem. Phys.*, 118:8207, 2003.

[33] Q. Yan, P. Rinke, M. Winkelnkemper, A. Qteish, D. Bimberg, M. Scheffler, and C. G. Van de Walle. Band parameters and strain effects in ZnO and group-III nitrides. *Semicond. Sci. Technol.*, 26:014037, 2011.

[34] L. Hedin and S. Lundqvist. Effects of electron-electron and electron-phonon interactions on the one-electron states of solids. *Solid State Physics*, 23:1, 1970.

[35] M. S. Hybertsen and S. G. Louie. Electron correlation in semiconductors and insulators: Band gaps and quasiparticle energies. *Phys. Rev. B*, 34:5390, 1986.

[36] W. G. Aulbur, L. Jönsson, and J. W. Wilkins. Quasiparticle calculations in solids. *Solid State Phys.*, 54:1, 2000.

[37] G. Onida, L. Reining, and A. Rubio. Electronic excitations: density-functional versus many-body Green's-function approaches. *Rev. Mod. Phys.*, 74:601, 2002.

[38] R.W. Godby, M. Schlüter, and L.J. Sham. Accurate exchange-correlation potential for silicon and its discontinuity on addition of an electron. *Phys. Rev. Lett.*, 56:2415, 1988.

[39] M. Rohlfing, P. Krüger, and J. Pollmann. Quasiparticle band structure of CdS. *Phys. Rev. Lett.*, 75:3489, 1995.

[40] M. Giantomassi, M. Stankovski, R. Shaltaf, M. Grüning, F. Bruneval, P. Rinke, and G.M. Rignanese. Electronic properties of interfaces and defects from many-body perturbation theory: Recent developments and applications. *phys. stat. sol. (b)*, 248:275, 2011.

[41] W.G. Aulbur, L. Jönsson, and J.W. Wilkins. *Solid State Physics, Advances in Research and Application.* Academic, New York, 2000.

[42] M. Städele, J. A. Majewski, P. Vogl, and A. Görling. Exact Kohn-Sham exchange potential in semiconductors. *Phys. Rev. Lett.*, 79:2089, 1997.

[43] G. Strinati. Dynamical shift and broadening of core excitons in semiconductors. *Phys. Rev. Lett.*, 49:1519, 1982.

[44] G. Strinati. Effects of dynamical screening on resonances at inner-shell thresholds in semiconductors. *Phys. Rev. B*, 29:5718, 1984.

[45] B. Adolph, V.I. Gavrilenko, K. Tenelsen, F. Bechstedt, and R. Del Sole. Nonlocality and many-body effects in the optical properties of semiconductors. *Phys. Rev. B*, 53:9797, 1996.

[46] P. A. M. Dirac. The quantum theory of emission and absorption of radiation. *Proc. Roy. Soc.*, A114:243, 1927.

[47] F. Seitz. The theoretical constitution of metallic lithium. *Phys. Rev.*, 47:400, 1935.

[48] J. M. Luttinger and W. Kohn. Motion of electrons and holes in perturbed periodic fields. *Phys. Rev.*, 97:869, 1955.

[49] E. O. Kane. Energy band structure in p-type germanium and silicon. *J.Phys.Chem.Solids*, 1:82, 1956.

[50] M. Cardona and F. H. Pollak. Energy-band structure of germanium and silicon: The $k \cdot p$ method. *Phys. Rev.*, 142:530, 1966.

[51] G. L. Bir and G. E. Pikus. *Symmetry and Strain-Induced Effects in Semiconductors.* Wiley, New York, 1974.

[52] S. Nakamura, T. Mukai, and M. Senoh. High-power GaN p-n junction blue-light-emitting diodes. *Jpn. J. Appl. Phys.*, 30:L1998, 1991.

[53] S. Nakamura, M. Senoh, S. Nagahama, N. Iwasa, T. Yamada, T. Matsushita, Y. Sugimoto, and H. Kiyoku. Room-temperature continuous-wave operation of InGaN multi-quantum-well structure laser diodes. *Appl. Phys. Lett.*, 69:4056, 1996.

[54] T. Nishida, H. Saito, and N. Kobayashi. Efficient and high-power AlGaN-based ultraviolet light-emitting diode grown on bulk gan. *Appl. Phys. Lett.*, 79:711, 2001.

[55] Y. Taniyasu, M. Kasu, and T. Makimoto. An aluminium nitride light-emitting diode with a wavelength of 210 nanometres. *Nature*, 441:325, 2006.

[56] D. A. B. Miller, D. S. Chemla, T. C. Damen, A. C. Gossard, W. Wiegmann, T. H. Wood, and C. A. Burrus. Band-edge electroabsorption in quantum well structures: The quantum-confined Stark effect. *Phys. Rev. Lett.*, 53:2173, 1984.

[57] S. Park and S. Chuang. Crystal-orientation effects on the piezoelectric field and electronic properties of strained wurtzite semiconductors. *Phys. Rev. B*, 59:4725, 1999.

[58] H. Masui, H. Yamada, K. Iso, S. Nakamura, and S. P. Denbaars. Optical polarization characteristics of m-oriented InGaN/GaN light-emitting diodes

with various indium compositions in single-quantum-well structure. *J. Phys. D: Appl. Phys.*, 41:225104, 2008.

[59] M. D. McCluskey, C. G. Van de Walle, L. T. Romano, B. S. Krusor, and N. M. Johnson. Effect of composition on the band gap of strained $In_xGa_{1-x}N$ alloys. *J. Appl. Phys.*, 93:4340, 2003.

[60] K. P. O'Donnell, R. W. Martin, C. Trager-Cowan, M. E. White, K. Esona, C. Deatcher, P. G. Middleton, K. Jacobs, W. Van der Stricht, C. Merlet, B. Gil, A. Vantomme, and J.F.W. Mosselmans. The dependence of the optical energies on InGaN composition. *Mater. Sci. Eng.*, B82:194, 2001.

[61] C. A. Parker, J. C. Roberts, S. M. Bedair, M. J. Reed, S. X. Liu, N. A. El-Masry, and L. H. Robins. Optical band gap dependence on composition and thickness of $In_xGa_{1-x}N$ ($0 < x < 0.25$) grown on GaN. *Appl. Phys. Lett.*, 75:2566, 1999.

[62] K. Kojima, H. Kamon, M. Funato, and Y. Kawakami. Theoretical investigations on anisotropic optical properties in semipolar and nonpolar InGaN quantum wells. *phys. stat. sol. (a)*, 5:3038, 2008.

[63] A. A. Yamaguchi. Anisotropic optical matrix elements in strained GaN-quantum wells with various substrate orientations. *phys. stat. sol. (c)*, 5:2329, 2008.

[64] Q. Yan, P. Rinke, M. Scheffler, and C. G. Van de Walle. Role of strain in polarization switching in semipolar InGaN/GaN quantum wells. *Appl. Phys. Lett.*, 97:181102, 2010.

[65] W. Scheibenzuber, U. Schwarz, R. Veprek, B. Witzigmann, and A. Hangleiter. Optical anisotropy in semipolar (Al,In)GaN laser waveguides. *phys. stat. sol. (c)*, 7:1925, 2010.

[66] M. Ueda, M. Funato, K. Kojima, Y. Kawakami, Y. Narukawa, and T. Mukai. Polarization switching phenomena in semipolar $In_xGa_{1-x}N$/GaN quantum well active layers. *Phys. Rev. B*, 78:233303, 2008.

[67] M. Smith, G. D. Chen, J. Y. Lin, H. X. Jiang, M. Asif Khan, C. J. Sun, Q. Chen, and J. W. Yang. Free excitonic transitions in GaN grown by metal-organic chemical-vapor deposition. *J. Appl. Phys.*, 79:7001, 1996.

[68] G. D. Chen, M. Smith, J. Y. Lin, H. X. Jiang, S. H. Wei, M. Asif Kahn, and C. J. Sun. Fundamental optical transitions in GaN. *Appl. Phys. Lett.*, 68:2784, 1996.

[69] B. Gil and A. Alemu. Optical anisotropy of excitons in strained GaN epilayers grown along the $\langle 10\bar{1}0 \rangle$ direction. *Phys. Rev. B*, 56:12446, 1997.

[70] W. Shan, R. J. Hauenstein, A. J. Fischer, J. J. Song, W. G. Perry, M. D. Bremser, R. F. Davis, and B. Goldenberg. Strain effects on excitonic transitions in GaN: Deformation potentials. *Phys. Rev. B*, 54:13460, 1996.

[71] S. Chichibu, T. Azuhata, T. Sota, H. Amano, and I. Akasaki. Optical properties of tensile-strained wurtzite GaN epitaxial layers. *Appl. Phys. Lett.*, 70:2085, 1997.

[72] B. Gil, M. Moret, O. Briot, S. Ruffenach, Ch. Giesen, M. Heuken, S. Rushworth, T. Leese, and M. Succii. InN excitonic deformation potentials determined experimentally. *J. Cryst. Growth*, 311:2798, 2009.

[73] R. Ishii, A. Kaneta, M. Funato, Y. Kawakami, and A. A. Yamaguchi. All deformation potentials in GaN determined by reflectance spectroscopy under uniaxial stress: Definite breakdown of the quasicubic approximation. *Phys. Rev. B*, 81:155202, 2010.

[74] M. Suzuki and T. Uenoyama. Strain effect on electronic and optical properties of GaN/AlGaN quantum-well lasers. *J. Appl. Phys.*, 80:6868, 1996.

[75] S. L. Chuang and C. S. Chang. $\mathbf{k}\cdot\mathbf{p}$ method for strained wurtzite semiconductors. *Phys. Rev. B*, 54:2491, 1996.

[76] S. Ghosh, P. Waltereit, O. Brandt, H. T. Grahn, and K. H. Ploog. Electronic band structure of wurtzite GaN under biaxial strain in the m-plane investigated with photoreflectance spectroscopy. *Phys. Rev. B*, 65:075202, 2002.

[77] K. Shimada, T. Sota, and K. Suzuki. First-principles study on electronic and elastic properties of BN, AlN, and GaN. *J. Appl. Phys.*, 84:4951, 1998.

[78] W. W Chow, A. F. Wright, A. Girndt, F. Jahnke, and S. W. Koch. Theory of gain in group-III nitride lasers. *Mater. Res. Soc. Symp. Proc.*, 468:487, 1997.

[79] J. A. Majewski, M. Stadele, and P. Vogl. Electronic structure of biaxially strained wurtzite crystals GaN and AlN. *Mater. Res. Soc. Symp. Proc.*, 449:887, 1997.

[80] Q. Yan, P. Rinke, M. Scheffler, and C. G. Van de Walle. Strain effects in group-III nitrides: Deformation potentials for AlN, GaN, and InN. *Appl. Phys. Lett.*, 95:121111, 2009.

[81] A. A. Yamaguchi, Y. Mochizuki, C. Sasaoka, A. Kimura, M. Nido, and A. Usui. Reflectance spectroscopy on GaN films under uniaxial stress. *Appl. Phys. Lett.*, 71:374, 1997.

[82] P. Misra, U. Behn, O. Brandt, H. T. Grahn, B. Imer, S. Nakamura, S. P. DenBaars, and J. S. Speck. Polarization anisotropy in GaN films for different nonpolar orientations studied by polarized photoreflectance spectroscopy. *Appl. Phys. Lett.*, 88:161920, 2006.

[83] H. Y. Peng, M. D. McCluskey, Y. M. Gupta, M. Kneissl, and N. M. Johnson. Shock-induced band-gap shift in GaN: Anisotropy of the deformation potentials. *Phys. Rev. B*, 71:115207, 2005.

[84] J. Heyd, G. E. Scuseria, and M. Ernzerhof. Erratum: "Hybrid functionals based on a screened Coulomb potential" [J. Chem. Phys. 118, 8207 (2003)]. *J. Chem. Phys.*, 124:219906, 2006.

[85] P. Rinke, A. Qteish, J. Neugebauer, C. Freysoldt, and M. Scheffler. Combining gw calculations with exact-exchange density-functional theory: an analysis of valence-band photoemission for compound semiconductors. *New J. Phys.*, 7:126, 2005.

[86] H. Masui, T. J. Baker, M. Iza, H. Zhong, S. Nakamura, and S. P. DenBaars. Light-polarization characteristics of electroluminescence from InGaN/GaN light-emitting doides prepared on $(11\overline{2}2)$-plane GaN. *J. Appl. Phys.*, 100:113109, 2006.

[87] H. Masui, H. Asamizu, A. Tyagi, N. F. DeMille, S. Nakamura, and S. P. DenBaars. Correlation between optical polarization and luminescence morphology of $(11\overline{2}2)$-oriented InGaN/GaN quantum-well structures. *Appl. Phys. Express*, 2:071002, 2009.

[88] G. B. Ren, Y. M. Liu, and P. Blood. Valence-band structure of wurtzite GaN including the spin-orbit interaction. *Appl. Phys. Lett.*, 74:1117, 1999.

[89] P. E. Blöchl. Projector augmented-wave method. *Phys. Rev. B*, 50:17953, 1994.

[90] G. Kresse and J. Furthmüller. Efficient iterative schemes for ab initio total-energy calculations using a plane-wave basis set. *Phys. Rev. B*, 54:11169, 1996.

[91] A. F. Wright. Elastic properties of zinc-blende and wurtzite aln, gan, and inn. *J. Appl. Phys.*, 82:2833, 1997.

[92] M. D. McCluskey, C. G. Van de Walle, C. P. Master, L. T. Romano, and N. M. Johnson. Large band gap bowing of $In_xGa_{1-x}N$ alloys. *Appl. Phys. Lett.*, 72:2725, 1998.

[93] C. G. Van de Walle, M.D. McCluskey, C. P. Master, L. T. Romano, and N. M. Johnson. Large and composition-dependent band gap bowing in $In_xGa_{1-x}N$ alloys. *Mater. Sci. Eng.*, B59:274, 1999.

[94] S. Pereira, M. R. Correia, T. Monteiro, E. Pereira, E. Alves, A. D. Sequeira, and N. Franco. Compositional dependence of the strain-free optical band gap in $In_xGa_{1-x}N$ layers. *Appl. Phys. Lett.*, 78:2137, 2001.

[95] P. G. Moses and C. G. Van de Walle. Band bowing and band alignment in InGaN alloys. *Appl. Phys. Lett.*, 96:021908, 2010.

[96] B. A. Haskell, F. Wu, S. Matsuda, M. D. Craven, P. T. Fini, S. P. DenBaars, J. S. Speck, and S. Nakamura. Structural and morphological characteristics of planar $(11\bar{2}0)$ *a*-plane gallium nitride grown by hydride vapor phase epitaxy. *Appl. Phys. Lett.*, 83:1554, 2003.

[97] K. Nishizuka, M. Funato, Y. Kawakami, S. Fujita, Y. Narukawa, and T. Mukai. Light-polarization characteristics of electroluminescence from InGaN/GaN light-emitting diodes prepared on $(11\overline{2}2)$-plane GaN. *Appl. Phys. Lett.*, 85:3122, 2004.

[98] A. Tyagi, Y.-D. Lin, D. A. Cohen, M. Saito, K. Fujito, J. S. Speck, S. P. DenBaars, and S. Nakamura. Stimulated emission at blue-green (480 nm) and green (514 nm) wavelengths from nonpolar (m-plane) and semipolar $(11\overline{2}2)$ InGaN multiple quantum well laser diode structures. *Appl. Phys. Express*, 1:091103, 2008.

[99] U. Behn, P. Misra, H. T. Grahn, B. Imer, S. Nakamura, S. P. DenBaars, and J. S. Speck. Polarization anisotropy in nonpolar oriented GaN films studied by polarized photoreflectance spectroscopy. *phys. stat. sol. (a)*, 204:299, 2007.

[100] N. F. Gardner, J. C. Kim, J. J. Wierer, Y. C. Shen, and M. R. Krames. Polarization anisotropy in the electroluminescence of m-plane InGaN/GaN multiple-quantum-well light-emitting diodes. *Appl. Phys. Lett.*, 86:111101, 2005.

[101] H. Tsujimura, S. Nakagawa, K. Okamoto, and H. Ohta. Characteristics of polarized electroluminescence from m-plane InGaN-based light emitting diodes. *Jpn. J. Appl. Phys.*, 46:L1010, 2007.

[102] T. Koyama, T. Onuma, H. Masui, A. Chakraborty, B. A. Haskell, S. Keller, U. K. Mishra, J. S. Speck, S. Nakamura, S. P. DenBaars, T. Sota, and S. F. Chichibu. Prospective emission efficiency and in-plane light polarization of nonpolar m-plane $In_xGa_{1-x}N/GaN$ blue light emitting diodes fabricated on freestanding GaN substrates. *Appl. Phys. Lett.*, 89:091906, 2006.

[103] M. Ueda, K. Kojima, M. Funato, Y. Kawakami, Y. Narukawa, and T. Mukai. Epitaxial growth and optical properties of semipolar $(11\overline{2}2)$ GaN and InGaN/GaN quantum wells on GaN bulk substrates. *Appl. Phys. Lett.*, 89:211907, 2006.

[104] Dmitry S. Sizov, Rajaram Bhat, Jerome Napierala, Chad Gallinat, Kechang Song, and Chung en Zah. 500-nm optical gain anisotropy of semipolar $(11\overline{2}2)$ InGaN quantum wells. *Appl. Phys. Express*, 2:071001, 2009.

[105] K. Kojima, M. Funato, Y. Kawakami, S. Masui, S. Nagahama, and T. Mukai. Stimulated emission at 474 nm from an InGaN laser diode structure grown on a $(11\overline{2}2)$ GaN substrate. *Appl. Phys. Lett.*, 91:251107, 2007.

[106] V. Bougrov, M. Levinshtein, S. Rumyantsev, and A. Zubrilov. *Properties of Advanced Semiconductor Materials* edited by M. E. Levinshtein, S. L. Rumyantsev, and M. S. Shur. Wiley, New York, 2001.

[107] C. Roberts, Q. Yan, M. S. Miao, and C. G. Van de Walle. Confinement

effects on valence-subband character and polarization anisotropy in $(11\overline{2}2)$ semipolar InGaN/GaN quantum wells. *J. Appl. Phys.*, 111:073113, 2012.

[108] A. Tyagi, F. Wu, E. C. Young, A. Chakraborty, H. Ohta, R. Bhat, K. Fujito, S. P. DenBaars, S. Nakamura, and J. S. Speck. Partial strain relaxation via misfit dislocation generation at heterointerfaces in (Al,In)GaN epitaxial layers grown on semipolar $(11\overline{2}2)$ GaN free standing substrates. *Appl. Phys. Lett.*, 95:251905, 2009.

[109] S. Hautakangas, J. Oila, M. Alatalo, K. Saarinen, L. Liszkay, D. Seghier, and H. P. Gislason. Vacancy defects as compensating centers in Mg-doped GaN. *Phys. Rev. Lett.*, 90:137402, 2003.

[110] S. Zeng, G. N. Aliev, D. Wolverson, J. J. Davies, S. J. Bingham, D. A. Abdulmalik, P. G. Coleman, T. Wang, and P. J. Parbrook. Origin of the red luminescence in Mg-doped GaN. *Appl. Phys. Lett.*, 89:022107, 2006.

[111] S. Nakamura, N. Iwasaki, M. Senoh, and T. Mukai. Hole compensation mechanism of p-type GaN films. *Jpn. J. Appl. Phys.*, 31:1258, 1992.

[112] M. W. Bayerl, M. S. Brandt, E. R. Glaser, A. E. Wickenden, D. D. Koleske, R. L. Henry, and M. Stutzmann. The origin of red luminescence from Mg-doped GaN. *phys. stat. sol. (b)*, 216:547, 1999.

[113] M. W. Bayerl, et al. M. S. Brandt, O. Ambacher, M. Stutzmann, E. R. Glaser, R. L. Henry, A. E. Wickenden, D. D. Koleske, T. Suski, I. Grzegory,

and S. Porowski. Optically detected magnetic resonance of the red and near-infrared luminescence in Mg-doped GaN. *Phys. Rev. B*, 63:125203, 2001.

[114] U. Kaufmann, M. Kunzer, H. Obloh, M. Maier, Ch. Manz, A. Ramakrishnan, and B. Santic. Origin of defect-related photoluminescence bands in doped and nominally undoped GaN. *Phys. Rev. B*, 59:5561, 1999.

[115] W. Götz, L. T. Romano, B. S. Krusor, N. M. Johnson, and R. J. Molnar. Electronic and structural properties of GaN grown by hydride vapor phase epitaxy. *Appl. Phys. Lett.*, 69:242, 1996.

[116] C. Lee, J. E. Kim, H. Y. Park, S. T. Kim, and H. Lim. Defect-related luminescence of Mg-doped n-GaN grown by hybrid vapour-phase epitaxy. *J. Phys.: Condens. Matter*, 10:11103, 1998.

[117] G. Salviati, N. Armani, C. Zanotti-Fregonara, E. Gombia, M. Albrecht, H. P. Strunk, M. Mayer, M. Kamp, and A. Gasparotto. Deep level related yellow luminescence in p-type GaN grown by MBE on (0001) sapphire. *MRS Internet J. Nitride Semicond. Res.*, 5S1:W11.50, 2000.

[118] O. Gelhausen, H. N. Klein, M. R. Phillips, and E. M. Goldys. Low-energy electron-beam irradiation and yellow luminescence in activated Mg-doped GaN. *Appl. Phys. Lett.*, 83:3293, 2003.

[119] J. Neugebauer and C. G. Van de Walle. Gallium vacancies and the yellow luminescence in GaN. *Appl. Phys. Lett.*, 69:503, 1996.

[120] J. L. Lyons, A. Janotti, and C. G. Van de Walle. Carbon impurities and the yellow luminescence in GaN. *Appl. Phys. Lett.*, 97:152108, 2010.

[121] M. A. Reshchikov and H. Morkoç. Luminescence properties of defects in GaN. *J. Appl. Phys.*, 97:061301, 2005.

[122] F. A. Reboredo and S. T. Pantelides. Novel defect complexes and their role in the p-type doping of GaN. *Phys. Rev. Lett.*, 82:1887, 1999.

[123] O. Madelung, editor. *Semiconductors-Basic Data, 2nd revised ed.* Springer, Berlin, 1996.

[124] M. G. Ganchenkova and R. M. Nieminen. Nitrogen vacancies as major point defects in gallium nitride. *Phys. Rev. Lett.*, 96:196402, 2006.

[125] R. Schlesser, R. Dalmau, and Z. Sitar. Seeded growth of AlN bulk single crystals by sublimation. *J. Cryst. Growth*, 241:416, 2002.

[126] A. Khan, K. Balakrishnan, and T. Katona. Ultraviolet light-emitting diodes based on group three nitrides. *Nature Photonics*, 2:77, 2008.

[127] G. A. Slack, R. A. Tanzilli, R. O. Pohl, and J. W. Vandersande. The intrinsic thermal conductivity of AlN. *J. Phys. Chem. Solids*, 48:641, 1987.

[128] J.-M. Mäki, I. Makkonen, F. Tuomisto, A. Karjalainen, S. Suihkonen, J. Räisänen, T. Yu. Chemekova, and Yu. N. Makarov. Identification of the V_{Al}-O_N defect complex in AlN single crystals. *Phys. Rev. B*, 84:081204, 2011.

[129] S. M. Evans, N. C. Giles, L. E. Halliburton, G. A. Slack, S. B. Schujman, and L. J. Schowalter. Electron paramagnetic resonance of a donor in aluminum nitride crystals. *Appl. Phys. Lett.*, 88:062112, 2006.

[130] N. T. Son, A. Gali, Á. Szabó, M. Bickermann, T. Ohshima, J. Isoya, and E. Janzén. Defects at nitrogen site in electron-irradiated AlN. *Appl. Phys. Lett.*, 98:242116, 2011.

[131] G. A. Slack and T. F. McNelly. AlN single crystals. *J. Cryst. Growth*, 42:560, 1977.

[132] G. A. Slack, L. J. Schowalter, D. Morelli, and J. A. Freitas Jr. Some effects of oxygen impurities on AlN and GaN. *J. Cryst. Growth*, 246:287, 2002.

[133] M. Bickermann, B. M. Epelbaum, and A. Winnacker. Characterization of bulk AlN with low oxygen content. *J. Cryst. Growth*, 269:432, 2004.

[134] M. Bickermann, A. Münch, B. M. Epelbaum, O. Filip, P. Heimann, S. Nagata, and A. Winnacker. Polarization-dependent below band-gap optical absorption of aluminum nitride bulk crystals. *J. Appl. Phys.*, 103:073522, 2008.

[135] G. A. Cox, D. O. Cummins, K. Kawabe, and R. H. Tredgold. On the preparation, optical properties and electrical behaviour of aluminium nitride. *J. Phys. Chem. Solids*, 28:543, 1967.

[136] A. Sedhain, L. Du, J. H. Edgar, J. Y. Lin, and H. X. Jiang. The origin of 2.78 ev emission and yellow coloration in bulk AlN substrates. *Appl. Phys. Lett.*, 95:262104, 2009.

[137] K. Atobe, M. Honda, N. Fukuoka, M. Okada, and M. Nakagawa. F-type centers in neutron-irradiated AlN. *Jpn. J. Appl. Phys.*, 29:150, 1990.

[138] R. A. Youngman and J. H. Harris. Luminescence studies of oxygen-related defects in aluminum nitride. *J. Am. Ceram. Soc.*, 11:3238, 1990.

[139] M. Morita, K. Tsubouchi, and N. Mikoshiba. Optical absorption and cathodoluminescence of epitaxial aluminum nitride films. *Jpn. J. Appl. Phys.*, 21:1102, 1982.

[140] T. Koyama, M. Sugawara, T. Hoshi, A. Uedono, J. F. Kaeding, R. Sharma, S. Nakamura, and S. F. Chichibu. Relation between Al vacancies and deep emission bands in AlN epitaxial films grown by NH_3-source molecular beam epitaxy. *Appl. Phys. Lett.*, 90:241914, 2007.

[141] K. Laaksonen, M. G. Ganchenkova, and R. M. Nieminen. Vacancies in wurtzite GaN and AlN. *J. Phys.: Condens. Matter*, 21:015803, 2009.

[142] T. Mattila and R. M. Nieminen. Point-defect complexes and broadband luminescence in GaN and AlN. *Phys. Rev. B*, 55:9571, 1997.

[143] I. Gorczyca, A. Svane, and N. E. Christensen. Theory of point defects in GaN, AlN, and BN: Relaxation and pressure effects. *Phys. Rev. B*, 60:8147, 1999.

[144] W. Kohn and L. J. Sham. Self-consistent equations including exchange and correlation effects. *Phys. Rev.*, 140:A1133, 1965.

[145] G. Kresse and D. Joubert. Efficient iterative schemes for ab initio total-energy calculations using a plane-wave basis set. *Phys. Rev. B*, 59:1758, 1999.

[146] L. Hedin. New method for calculating the one-particle Green's function with application to the electron-gas problem. *Phys. Rev.*, 139:A796, 1965.

[147] M. Rohlfing and S. G. Louie. Electron-hole excitations and optical spectra from first principles. *Phys. Rev. B*, 62:4927, 2000.

[148] M. L. Tiago and J. R. Chelikowsky. Optical excitations in organic molecules, clusters, and defects studied by first-principles Green's function methods. *Phys. Rev. B*, 73:205334, 2006.

[149] M. Bockstedte, A. Marini, O. Pankratov, and A. Rubio. Many-body effects

in the excitation spectrum of a defect in SiC. *Phys. Rev. Lett.*, 105:026401, 2010.

[150] Y. Ma and M. Rohlfing. Optical excitation of deep defect levels in insulators within many-body perturbation theory: The F center in calcium fluoride. *Phys. Rev. B*, 77:115118, 2008.

[151] J. Deslippe, G. Samsonidze, D. A. Strubbe, M. Jain, M. L. Cohen, and S. G. Louie. BerkeleyGW: A massively parallel computer package for the calculation of the quasiparticle and optical properties of materials and nanostructures. *Comput. Phys. Commun.*, 183:1269, 2012.

[152] P. Giannozzi, S. Baroni, N. Bonini, M. Calandra, R. Car, C. Cavazzoni, D. Ceresoli, G. L. Chiarotti, M. Cococcioni, I. Dabo, A. Dal Corso, S. de Gironcoli, S. Fabris, G. Fratesi, R. Gebauer, U. Gerstmann, C. Gougoussis, A. Kokalj, M. Lazzeri, L. Martin-Samos, N. Marzari, F. Mauri, R. Mazzarello, S. Paolini, A. Pasquarello, L. Paulatto, C. Sbraccia, S. Scandolo, G. Sclauzero, A. P. Seitsonen, A. Smogunov, P. Umari, and R. M. Wentzcovitch. QUANTUM ESPRESSO: a modular and open-source software project for quantum simulations of materials. *J. Phys.: Condens. Matter*, 21(39):395502 (19pp), 2009.

[153] C. Persson, R. Ahuja, A. Ferreira da Silva, and B. Johansson. First-

principle calculations of optical properties of wurtzite AlN and GaN. *J. Cryst. Growth*, 231:407, 2001.

[154] L. X. Benedict, T. Wethkamp, K. Wilmers, C. Cobet, N. Esser, E. L. Shirley, W. Richter, and M. Cardona. Dielectric function of wurtzite GaN and AlN thin films. *Solid State Commun.*, 112:129, 1999.

[155] T. Takeuchi, H. Amano, and I. Akasaki. Theoretical study of orientation dependence of piezoelectric effects in wurtzite strained GaInN/GaN heterostructures and quantum wells. *Jpn. J. Appl. Phys.*, 39:413, 2000.

[156] S. H. Park and D. Ahn. Depolarization effects in $(11\overline{2}2)$-oriented InGaN/GaN quantum well structures. *Appl. Phys. Lett.*, 90:013505, 2007.

[157] Y. Zhao, J. Sonoda, C. C. Pan, S. Brinkley, I. Koslow, K. Fujito, H. Ohta, S. P. DenBaars, and S. Nakamura. Depolarization effects in $(11\overline{2}2)$-oriented InGaN/GaN quantum well structures. *Appl. Phys. Express*, 3:102101, 2010.

[158] H. Zhong, A. Tyagi, N. N. Fellows, F. Wu, R. B. Chung, M. Saito, K. Fujito, J. S. Speck, S. P. DenBaars, and S. Nakamura. High power and high efficiency blue light emitting diode on freestanding semipolar $(10\overline{1}\overline{1})$ bulk GaN substrate. *Appl. Phys. Lett.*, 90:233504, 2007.

[159] A. David and M. J. Grundmann. Influence of polarization fields on carrier lifetime and recombination rates in InGaN-based light-emitting diodes. *Appl. Phys. Lett.*, 97:033501, 2010.

[160] E. Kioupakis and Q. Yan and C. G. Van de Walle. Interplay of polarization fields and Auger recombination in the efficiency droop of nitride light-emitting diodes. Submitted.

[161] J. G. Gualtieri, J. A. Kosinski, and A. Ballato. Piezoelectric materials for acoustic wave applications. *IEEE Trans. Ultrason. Ferroelectr. Freq. Control*, 41:53, 1994.

[162] A. E. Romanov, P. Waltereit, and J. S. Speck. Buried stressors in nitride semiconductors: Influence on electronic properties. *J. Appl. Phys.*, 97:043708, 2005.

[163] S. Nakamura, S. Pearton, and G. Fasol. *"The Blue Laser Diode: The Complete Story"*. Springer, Berlin, 2000.

[164] Y. Shen, G. O. Mueller, S. Watanabe, N. F. Gardner, A. Munkholm, and M. R. Krames. Auger recombination in InGaN measured by photoluminescence. *Appl. Phys. Lett.*, 91:141101, 2007.

[165] Emmanouil Kioupakis, Patrick Rinke, Kris T. Delaney, and Chris G. Van de Walle. Indirect Auger recombination as a cause of efficiency droop in nitride light-emitting diodes. *Appl. Phys. Lett.*, 98:161107, 2011.

[166] A. David, M. J. Grundmann, J. F. Kaeding, N. F. Gardner, T. G. Mihopoulos, and M. R. Krames. Carrier distribution in (0001)InGaN/GaN multiple quantum well light-emitting diodes. *Appl. Phys. Lett.*, 92:053502, 2008.

[167] C. Y. Huang, Q. Yan, Y. Zhao, K. Fujito, D. Feezell, C. G. Van de Walle, J. S. Speck, S. P. DenBaars, and S. Nakamura. Influence of Mg-doped barriers on semipolar $(20\bar{1}1)$ multiple-quantum-well green light-emitting diodes. *Appl. Phys. Lett.*, 99:141114, 2011.

[168] V. F. Mymrin, K. A. Bulashevich, N. I. Podolskaya, I. A. Zhmakin, S. Yu. Karpov, and Yu. N. Makarov. Modelling study of MQW LED operation. *phys. stat. sol. (c)*, 2:2928, 2005.

[169] J. W. Raring, M. C. Schmidt, C. Poblenz, Y. C. Chang, M. J. Mondry, B. Li, J. Iveland, B. Walters, M. R. Krames, R. Craig, P. Rudy, J. S. Speck, S. P. DenBaars, and S. Nakamura. High-efficiency blue and true-green-emitting laser diodes based on non-*c*-plane oriented GaN substrates. *Appl. Phys. Express*, 3:112101, 2010.

[170] Y. Enya, Y. Yoshizumi, T. Kyono, K. Akita, M. Ueno, M. Adachi, T. Sumitomo, T. Ikegami S. Tokuyama, K. Katayama, and T. Nakamura. 531 nm green lasing of InGaN based laser diodes on semi-polar 2021 free-standing GaN substrates. *Appl. Phys. Express*, 2:082101, 2009.

[171] Y. D. Lin, S. Yamamoto, C. Y. Huang, C. L. Hsiung, F. Wu, K. Fujito, H. Ohta, J. S. Speck, S. P. Denbaars, and S. Nakamura. High quality InGaN/AlGaN multiple quantum wells for semipolar InGaN green laser diodes. *Appl. Phys. Express*, 3:082001, 2010.

[172] P. Waltereit, O. Brandt, A. Trampert, H. T. Grahn, J. Menniger, M. Ramsteiner, M. Reiche, and K. H. Ploog. Nitride semiconductors free of electrostatic fields for efficient white light-emitting diodes. *Nature*, 406:865, 2000.

[173] M. C. Schmidt, K. C. Kim, H. Sato, N. Fellows, H. Masui, S. Nakamura, S. P. DenBaars, and J. S. Speck. High power and high external efficiency m-plane ingan light emitting diodes. *Jpn. J. Appl. Phys.*, 46:L126, 2007.

[174] J. E. Northrup. GaN and InGaN $(11\overline{2}2)$ surfaces: Group-III adlayers and indium incorporation. *Appl. Phys. Lett.*, 95:133107, 2009.

[175] H. Sato, R. B. Chung, H. Hirasawa, N. Fellows, H. Masui, F. Wu, M. Saito, K. Fujito, J. S. Speck, S.P. DenBaars, and S. Nakamura. Optical properties of yellow light-emitting diodes grown on semipolar $(11\overline{2}2)$ bulk GaN substrates. *Appl. Phys. Lett.*, 92:221110, 2008.

[176] P. S. Hsu, E. C. Young, A. E. Romanov, K. Fujito, S. P. DenBaars, S. Nakamura, and J. S. Speck. Misfit dislocation formation via pre-existing threading dislocation glide in $(11\overline{2}2)$ semipolar heteroepitaxy. *Appl. Phys. Lett.*, 99:081912, 2011.

[177] T. Kyono, Y. Yoshizumi, Y. Enya, M. Adachi, S. Tokuyama, M. Ueno, K. Katayama, and T. Nakamura. Optical polarization characteristics of

ingan quantum wells for green laser diodes on semi-polar $\{20\overline{21}\}$ gan substrates. *Appl. Phys. Express*, 3:011003, 2010.

[178] S. Yamamoto, Y. Zhao, C. C. Pan, R. B. Chung, K. Fujito, J. Sonoda, S. P. Denbaars, and S. Nakamura. High-efficiency single-quantum-well green and yellow-green light-emitting diodes on semipolar $(20\overline{21})$ GaN substrates. *Appl. Phys. Express*, 3:122102, 2010.

[179] Y. Zhao, T. Tanaka, Q. Yan, C. Y. Huang, R. B. Chung, C. C. Pan, K. Fujito, D. Feezell, C. G. Van de Walle, J. S. Speck, S. P. DenBaars, and S. Nakamura. High optical polarization ratio from semipolar $(20\overline{21})$ blue-green InGaN/GaN light-emitting diodes. *Appl. Phys. Lett.*, 99:051109, 2011.

[180] Y. Zhao, S. Tanaka, C. C. Pan, K. Fujito, D. Feezell, J. S. Speck, S. P. DenBaars, , and S. Nakamura. High-power blue-violet semipolar $(20\overline{21})$ ingan/gan light-emitting diodes with low efficiency droop at 200 A/cm^2. *Appl. Phys. Express*, 4:082104, 2011.

[181] C. Y. Huang, M. T. Hardy, K. Fujito, D. Feezell, J. S. Speck, S. P. DenBaars, and S. Nakamura. Demonstration of 505 nm laser diodes using wavelength-stable semipolar $(20\overline{21})$ InGaN/GaN quantum wells. *Appl. Phys. Lett.*, 95:241115, 2011.

[182] P. S. Hsu, J. Sonoda, K. M. Kelchner, A. Tyagi, R. M. Farrell, D. A. Haeger, E. C. Young, A. E. Romanov, K. Fujito, S. P. DenBaars H. Ohta, J. S.

Speck, and S. Nakamura. Blue InGaN/GaN laser diodes grown on $(30\bar{3}1)$ free-standing GaN substrates. *phys. stat. sol. (c)*, 8:2390, 2011.

[183] G. Davies. *Identification of Defects in Semiconductors (Semiconductors and Semimetals, vol. 51B), Chapter 1, Optical Measurements of Point Defects.* edited by M. Stavola. Academic, New York, 1999.

[184] Y. K. Kuo, M. C. Tsai, and S. H. Yen. Numerical simulation of blue InGaN light-emitting diodes with polarization-matched AlGaInN electron-blocking layer and barrier layer. *Opt. Commun.*, 282:4252, 2009.

[185] S. Yu. Karpov. Modeling of III-nitride light-emitting-diodes: progress, problems, and perspectives. *Proc. SPIE*, 7939:79391C–1–12, 2011.